

From the der Medizinischen Klinik und Poliklinik III
der Ludwig-Maximilians-Universität München
Direktor: Prof. Dr. Dr. Michael von Bergwelt



Dissertation
zum Erwerb des Doctor of Philosophy (Ph.D.) an der
Medizinischen Fakultät der
Ludwig-Maximilians-Universität zu München

Functional Characterization of *ARID1A* Mutations in Follicular Lymphoma

vorgelegt von:

Martina Antonioli

Jahr:

2023

Mit Genehmigung der Medizinischen Fakultät der
Ludwig-Maximilians-Universität zu München

First evaluator (1. TAC member): *Prof. Dr. Oliver Weigert*

Second evaluator (2. TAC member): *Prof. Heinrich Leonhardt*

Third evaluator: *Prof. Dr. Michael Albert*

Fourth evaluator: *Prof. Dr. Rainer Glaß*

Dean: Prof. Dr. med. Thomas Gudermann

Datum der Verteidigung:

04.10.2023

Part of this work was presented at the 63rd ASH (American Society of Hematology) Annual Meeting, December 11-14, 2021, Atlanta, GA, USA and was awarded an "Abstract Achievement Award".

Table of content

Table of content	4
Abstract	7
Zusammenfassung	8
List of Figures	10
List of Tables	11
List of abbreviations	12
1. Introduction	14
1.1 Follicular lymphoma	14
1.1.1 Clinical perspective of FL	14
1.1.2 Molecular perspective of FL.....	15
1.2 AT-rich interaction domain 1A (ARID1A) and the SWI/SNF complex.....	17
1.2.1 Epigenetics: a short introduction.....	17
1.2.2 The chromatin remodeling role of the SWI/SNF complexes	18
1.2.3 The SWI/SNF complexes: BAF and PBAF.....	19
1.2.4 <i>ARID1A</i> mutations are recurrent across cancers and inactivating	19
2. Aims of the study	21
3. Material and Methods	22
3.1 Material	22
3.1.1 Chemicals, reagents, and media	22
3.1.2 Consumables	24
3.1.3 Equipment.....	25
3.1.4 Kits	26
3.1.5 Standards	26
3.1.6 Buffers and Solutions	26
3.1.7 Fluorescent Dyes	27
3.1.8 Antibodies.....	27
3.1.9 Oligonucleotides.....	28
3.1.10 Short hairpin RNA plasmid	29
3.1.11 Plasmid.....	29
3.1.12 Primary patients data	30
3.2 Methods	31
3.2.1 Patients data	31
3.2.2 FL-like cell lines model system	31
3.2.3 <i>Ex vivo</i> BCL culture model system.....	33
3.2.4 RNA Sequencing (RNA-Seq).....	35
3.2.5 Assay for Transposase-Accessible Chromatin (ATAC-Seq)	36
3.2.6 Mass Spectrometry	37
3.2.7 Functional Assays	38
3.2.8 Nucleic acid methods	40
3.2.9 Flow-cytometry.....	41
3.2.10 Protein methods.....	44

3.2.11	Statistical analysis.....	46
4.	Results.....	47
4.1	ARID1A mutations in the GLSG2000 cohort	47
4.2	Generation of FL-like model systems	48
4.2.1	FL-like cell lines.....	48
4.2.2	B cell lymphoma-like (BCL) cells	48
4.3	Transcriptome analysis of CRISPR/Cas9-engineered cell lines with and without ARID1A mutation	49
4.3.1	Data analysis	49
4.3.2	Differential expression of genes (DEGs)	50
4.3.3	Gene ontology (GO) analysis	50
4.4	ARID1A loss affects cell growth and division in FL	51
4.4.1	Growth phenotype deriving from <i>ARID1A</i> mutations	51
4.4.2	GSEA suggests that <i>ARID1A</i> loss is associated with cell cycle progression and impaired mitosis	51
4.4.3	Slower cell cycle progression in <i>ARID1A</i> mutant clones correlates with anaphase chromatin bridge formation.....	52
4.4.4	Summary	53
4.5	ARID1A mutation impacts FASLG-induced apoptosis	54
4.5.1	<i>ARID1A</i> mutation status and FAS levels in primary FL samples.....	54
4.5.2	FAS levels upon <i>ARID1A</i> mutations in FL-like cell lines	55
4.5.3	FASLG-induced apoptosis phenotype in <i>ARID1A</i> mutant FL-like cell lines	56
4.5.4	CD8+ T lymphocytes-mediated killing upon <i>ARID1A</i> loss	57
4.5.5	<i>ARID1A</i> loss correlates with reduced FAS expression	57
4.5.6	Assay for Transposase-Accessible Chromatin using sequencing (ATAC-Seq) shows that chromatin openness at FAS TSS is not affected by <i>ARID1A</i> loss	58
4.5.7	FAS promoter accessibility upon <i>ARID1A</i> loss.....	59
4.5.8	Expression of FAS-regulating transcription factors upon <i>ARID1A</i> loss	59
4.5.9	Identification of the FAS-regulating <i>ARID1A</i> -dependent transcriptional network ...	60
4.5.10	<i>RUNX3</i> chromatin accessibility and expression are reduced upon <i>ARID1A</i> loss ..	60
4.5.11	ETS1 but not <i>RUNX3</i> alone, regulates FAS transcription	62
4.5.12	FAS phenotype upon <i>RUNX3</i> overexpression in <i>ARID1A</i> mutant clones.....	63
4.5.13	FAS rescue upon <i>RUNX3</i> overexpression is functionally relevant.....	64
4.5.14	Summary	64
4.6	ARID1A mutations impact T cells functions in FL	66
4.6.1	TME-derived gene expression signatures.....	66
4.6.2	Whole-transcriptome of FL-like cell lines shows deregulation of cytoskeleton and plasma membrane functions upon <i>ARID1A</i> loss	66
4.6.3	<i>ARID1A</i> loss impacts cellular stiffness.....	67
4.6.4	<i>ARID1A</i> mutations impair conjugates formation with CD4+ T cells in FL-like models.....	68
4.6.5	Summary	69
5.	Discussion.....	70
5.1	Functional characterization of <i>ARID1A</i> mutations in FL.....	70
5.1.1	<i>ARID1A</i> loss alters gene expression.....	70
5.1.2	<i>ARID1A</i> mutation causes cell growth defects and chromatin bridges formation	71
5.1.3	<i>ARID1A</i> mutation results in reduced FAS levels and FASLG-induced apoptosis ..	72
5.1.4	<i>ARID1A</i> mutations affect the complex cross-talk with T cells.....	74

5.2	Clinical vulnerabilities of <i>ARID1A</i> -mutant FL cases.....	75
6.	Future Perspectives.....	77
6.1	Broadening the knowledge of ARID1A loss systemic impact on CD4+ and CD8+ T lymphocytes.....	77
6.2	Gaining a comprehensive understanding of ARID1A loss impact on the TME	79
	References	81
	Acknowledgments	89
	Affidavit.....	91
	Confirmation of congruency.....	92
	Curriculum vitae.....	Error! Bookmark not defined.
	List of publications	93

Abstract

Background: Follicular lymphoma (FL) is one of the most common malignant lymphomas worldwide and the most common form of indolent lymphoma. FL is highly heterogeneous from both the clinical and molecular point of view. It remains a clinical challenge since advanced-stage disease is still considered incurable, and patients ultimately present with relapsed or refractory disease. Molecularly, FL is characterized by highly recurrent genetic mutations in genes coding for epigenetic modifiers. *ARID1A* mutations are among the most frequent mutations in FL (~10-20 % at the time of diagnosis). *ARID1A* mutations are a component of the prognostic clinic-genetic risk model m7-FLIPI (Pastore, Jurinovic et al. 2015). These mutations are primarily disruptive and result in protein haplodeficiency. Functionally, ARID1A is part of a SWI/SNF complex, which controls chromatin accessibility and is involved in numerous processes, including gene expression.

Aim: Functionally characterize *ARID1A* mutations in representative human FL model systems.

Methods: I used established and primary FL-like cell lines that harbor the hallmark t(14;18) translocation with or without heterozygous or homozygous *ARID1A* mutations (introduced by CRISPR/Cas9) or knock-down (by shRNA). I applied complementary omics approaches (RNA-Seq and ATAC-Seq) and functional assays to untangle the consequences of ARID1A loss in these FL model systems.

Results: ARID1A loss profoundly altered gene expression. Across three cell lines, we observed consistent down-regulation of genes involved in cell cycle regulation and apoptosis pathways upon ARID1A loss. In functional experiments, I could show that *ARID1A* mutant clones are characterized by significantly slower cell proliferation and increased formation of anaphase bridges.

Next, I demonstrated that ARID1A loss results in decreased FAS levels and lower sensitivity to FASLG-induced apoptosis. We discovered the underlying molecular mechanism through advanced bioinformatics analyses and functional experiments. Briefly, ARID1A loss does not directly affect FAS expression. Still, it results in reduced DNA accessibility and expression of the co-transcription factor *RUNX3*, thereby hindering RUNX3-ETS1 cooperativity and ETS1-induced FAS expression, which promotes a functionally and clinically relevant immune-evasive phenotype.

Finally, RNA-Seq analysis indicated that ARID1A loss alters the plasma membrane and cytoskeleton functions, as well as the overall abundance of ligands and receptors. *Ex vivo* co-cultures of FL-like cells with T cells suggested impaired immune synapse formation with CD4 T lymphocytes upon ARID1A loss.

Discussion and conclusion: Overall, our analyses provide novel insights into the functional consequences of *ARID1A* mutations in FL, most notably promoting immune evasion. A better understanding of mutation-specific biology, including its impact on interactions within the tumor microenvironment, holds promise for improved patient stratification and the development of personalized treatment approaches.

Zusammenfassung

Hintergrund: Das folliculäre Lymphom (FL) ist eines der häufigsten malignen Lymphome weltweit und die häufigste Form des indolenten Lymphoms. FL sind sowohl aus klinischer als auch aus molekularer Sicht sehr heterogen. Patienten mit FL stellen nach wie vor eine klinische Herausforderung dar, da sie meist erst im fortgeschrittenen Stadium diagnostiziert werden, weiterhin als unheilbar gelten und letztendlich eine rezidierte oder refraktäre Erkrankung entwickeln. Auf molekularer Ebene sind FL durch häufige Mutationen in epigenetischen Modifikatoren gekennzeichnet. *ARID1A* gehört zu den häufigsten Mutationen beim FL (~10-20 % zum Zeitpunkt der Diagnose). *ARID1A* Mutationen sind ein Bestandteil des prognostischen klinisch-genetischen Risikomodells m7-FLIPI (Pastore, Jurinovic et al. 2015). Diese Mutationen sind in erster Linie inaktivierend und führen zu einer Proteinhaplodefizienz. Funktionell ist ARID1A Teil eines SWI/SNF-Komplexes, der die Zugänglichkeit von Chromatin kontrolliert und an zahlreichen Prozessen, einschließlich der Genexpression, beteiligt ist.

Ziel: Funktionelle Charakterisierung von *ARID1A*-Mutationen in repräsentativen humanen FL-Modellsystemen.

Methoden: Ich verwendete etablierte und primäre FL-ähnliche Zelllinien, die die charakteristische t(14;18)-Translokation aufweisen, mit oder ohne heterozygote oder homozygote *ARID1A* Mutationen (eingeführt durch CRISPR/Cas9) oder Knock-down (durch shRNA). Ich habe komplementäre Omics-Ansätze (RNA-Seq und ATAC-Seq) und funktionelle Assays angewandt, um die Folgen des ARID1A Verlusts in diesen FL-Modellsystemen zu entschlüsseln.

Ergebnisse: Der Verlust von ARID1A führte zu tiefgreifenden Veränderungen der Genexpression. In drei Zelllinien beobachteten wir übereinstimmend eine geringere Expression von Genen, die an der Regulierung des Zellzyklus und an der Apoptose beteiligt sind, wenn ARID1A fehlt. In funktionellen Experimenten konnte ich zeigen, dass ARID1A mutierte Klone ein deutlich langsames Zellwachstum und eine vermehrte Bildung von Anaphase-Brücken zeigen.

Als Nächstes konnte ich zeigen, dass der Verlust von ARID1A zu einer verringerten FAS Expression und einer verminderten Empfindlichkeit gegenüber FASLG-induzierter Apoptose führt. Mittels detaillierter bioinformatische Auswertungen und funktioneller Experimente konnten wir den zugrundeliegenden molekularen Mechanismus aufklären. Zusammenfassend wirkt sich der Verlust von ARID1A nicht direkt auf die FAS-Expression aus. Stattdessen führt der ARID1A Verlust zu einer verringerten DNA Akzessibilität und Expression des Co-Transkriptionsfaktors *RUNX3*, wodurch die RUNX3-ETS1-Kooperativität und die ETS1-induzierte FAS-Expression behindert werden, was einen funktionell und klinisch relevanten immun-evasiven Phänotyp bewirkt.

Schließlich zeigte die RNA-Seq Analyse, dass der Verlust von ARID1A die Funktionen der Plasmamembran und des Zytoskeletts sowie die Expression von Liganden und Rezeptoren auf der Zelloberfläche verändert. *Ex vivo* Co-Kulturen von FL-ähnlichen Zellen mit T-Zellen deuteten darauf hin, dass die Bildung von Immunsynapsen mit CD4 T Lymphozyten bei ARID1A Verlust beeinträchtigt ist.

Diskussion und Schlussfolgerung: Insgesamt bieten unsere Analysen neue Einblicke in die funktionellen Folgen von *ARID1A* Mutationen beim FL und weisen insbesondere auf eine vermehrte Immunevasion hin. Ein besseres Verständnis der mutationsspezifischen Biologie, einschließlich der Auswirkungen von Mutationen auf die Interaktionen innerhalb der

Mikroumgebung des Tumors, hat das Potenzial, Patienten besser stratifizieren und personalisierter Behandlungsansätze entwickeln zu können.

List of Figures

Figure 1. The multistep process of lymphomagenesis.	16
Figure 2. Mutation profile of diagnostic FL biopsies from patients of the GLSG2000 cohort.	17
Figure 3. Germinal center reaction.	17
Figure 4. Transcription regulation by the SWI/SNF complex.	18
Figure 5. Composition of the SWI/SNF complexes.	19
Figure 6. Representative gating strategy.	42
Figure 7. Representative gating strategy for conjugation assay.	43
Figure 8. Representative gating strategy for cytotoxic assay.	44
Figure 9. <i>ARID1A</i> mutations in the GLSG2000 cohort.	47
Figure 10. Oncoplot of SWI/SNF subunits mutated in the GLSG2000 cohort.	47
Figure 11. ARID1A levels in CRISPR/Cas9-engineered clones.	48
Figure 12. ARID1A knockdown in BCL cells.	48
Figure 13. Principal component analysis (PCA) of <i>ARID1A</i> mutant and control samples from the RNA-Seq experiment.	49
Figure 14. Volcano plot showing differentially expressed genes (DEGs).	50
Figure 15. Top 10 down-regulated GO terms in OCI-Ly1 (MUT vs WT).	50
Figure 16. Growth curve of <i>ARID1A</i> mutant and WT CRISPR/Cas9-engineered clones.	51
Figure 17. Gene set enrichment analysis using the Reactome Pathway Database.	52
Figure 18. Anaphase chromatin bridges formation.	53
Figure 19. FAS quantification in primary FL biopsies.	54
Figure 20. FAS quantification in native FL-like cell lines.	55
Figure 21. FAS protein levels in CRISPR/Cas9 clones with and without <i>ARID1A</i> mutation.	55
Figure 22. FASLG-induced apoptosis assay.	56
Figure 23. FASLG-induced apoptosis assay.	57
Figure 24. T-cell mediated killing assay.	57
Figure 25. <i>FAS</i> gene expression levels upon ARID1A loss.	58
Figure 26. Overview ATAC-Seq analysis.	58
Figure 27. <i>FAS</i> promoter accessibility.	59
Figure 28. FAS-regulating TFs are not DE.	59
Figure 29. FAS-regulating co-TFs and ARID1A-dependent transcriptional network.	60
Figure 30. ETS1 and RUNX3 accessibility and expression levels.	61
Figure 31. Western blot of ETS1 immunoprecipitates (IP) from OCI-Ly1.	61
Figure 32. ETS1 but not RUNX3 alone regulates <i>FAS</i> transcription.	62
Figure 33. Western blot of RUNX3 over-expressing clones.	63
Figure 34. RUNX3 over-expression rescues <i>FAS</i> gene and protein levels.	63
Figure 35. <i>FAS</i> rescue upon RUNX3-overexpression is functionally relevant.	64
Figure 36. Novel <i>FAS</i> -regulatory network dependent on <i>ARID1A</i> mutation in FL.	65
Figure 37. TME-derived gene expression profile in primary FL.	66
Figure 38. Plasma membrane functions are altered upon ARID1A loss.	67
Figure 39. ARID1A loss impacts cellular stiffness and cell membrane plasticity.	67
Figure 40. Immune synapse formation in OCI-Ly8 clones.	68
Figure 41. Immune synapse formation in BCL cells.	69
Figure 42. <i>ARID1A</i> and <i>FAS</i> mutation frequency at advanced-stage or r/r disease.	74
Figure 43. LC/MS-MS of plasma membrane proteins in OCI-Ly8, OCI-Ly1, and DB cell lines with and without <i>ARID1A</i> mutation.	77
Figure 44. <i>In vitro</i> co-culture assay of CD8+ T cells with OCI-Ly8 cell lines, Mosunetuzumab effect.	78
Figure 45. BCL cells co-culture with autologous TME cells.	80

List of Tables

Table 1. List of used chemicals, reagents, and media.....	22
Table 2. List of used consumables	24
Table 3. List of used equipment.....	25
Table 4. List of used kits.....	26
Table 5. Protein standards and DNA ladder.....	26
Table 6. Buffers, solutions, and their composition	26
Table 7. Fluorescent dyes used for cell monitoring by FACS	27
Table 8. Primary and secondary antibodies used for Western blot	27
Table 9. Directly labeled antibodies used for cell monitoring by FACS	28
Table 10. Antibodies used for IHC.....	28
Table 11. List of used oligonucleotides and their application.....	28
Table 12. List of short hairpin RNA plasmids	29
Table 13. List of used plasmid.....	29
Table 14. References to patients' data.....	30
Table 15. CRISPR/Cas9 cell lines with and without <i>ARID1A</i> mutations.....	32
Table 16. TaqMan reaction mix (left) and PCR program (right)	41
Table 17. Proliferation dyes staining conditions	42

List of abbreviations

ANOVA	Analysis of variance
APC	Allophycocyanin
ARID1A	AT-rich interaction domain 1A protein
BCA	Bicinchoninic acid
BCL	B cell lymphoma-like
BCR	B cell receptor
CAR	Chimeric antigen receptor
CD	Cluster of differentiation
cDNA	Complementary DNA
CFSE	Carboxyfluorescein succinimidyl ester
CHOP	Cyclophosphamide, doxorubicin, vincristine, prednisone
CTL	Cytotoxic T lymphocytes
DAPI	4',6-diamidino-2-phenylindole
DE	Differentially express
DNA	Deoxyribonucleic acid
DO	Differentially open
ECL	Enhanced chemiluminescent
EV	Empty vector
FA	formaldehyde
FACS	Fluorescence-activated cell sorting
FASLG	FAS ligand
FAS-reg	FAS-regulatory
FDC	Follicular dendritic cells
FFPE	Formalin-fixed, paraffin-embedded
FFS	Failure-free survival
FL	Follicular lymphoma
FLIPI	Follicular Lymphoma International Prognostic Index
<i>g</i>	<i>g</i> force
GC	Germinal center
GC Bs	Germinal center B cells
GLSG	German Low-Grade Lymphoma Study Group
GO	Gene ontology
GSEA	Gene Set Enrichment Analysis
Het	Heterozygous
Hrs	Hours
HSA	Human serum albumin
Ig	Immunoglobulin
IHC	Immunohistochemistry
IL	Interleukin
IP	Immunoprecipitation
KO	Knock-out
LB	Lysogeny broth
LC-MS/MS	Liquid chromatography with tandem mass spectrometry
MACS	Magnetic-activated cell sorting
MHC	Major histocompatibility complex
Min	Minutes
MNCs	Mononuclear cells
mRNA	Messenger RNA
MUT	Mutant

NHL	Non-Hodgkin lymphoma
Nsc	Native single cell-derived clone
PAGE	Polyacrylamide gel electrophoresis
PBMCs	Peripheral blood mononuclear cells
PCA	Principal components analysis
PCR	Polymerase chain reaction
PRM	Parallel reaction monitoring assay
PVDF	Polyvinylidene difluoride
qPCR	Quantitative PCR
R	Rituximab
RFP	Red fluorescent protein
RIPA	Radioimmunoprecipitation assay buffer
RNA-seq	RNA sequencing
<i>Rpm</i>	Revolutions per minute
RT	Room temperature
SDS	Sodium dodecyl sulphate
shRNA	Short hairpin RNA
TBS	Tris-buffered saline
TBS-T	TBS with 0.2% (v/v) Tween20
TCR	T cell receptor
TFs	Transcription factors
TFH	T follicular helper cells
Th1	T helper cells type 1
TME	Tumor-microenvironment
TSS	Transcription starting site
VAF	Variant allele frequency
VPD	Violet proliferation dye
WT	Wild-type

1. Introduction

1.1 Follicular lymphoma

Follicular lymphoma (FL) is the most common form of indolent lymphoma worldwide, with a yearly incidence rate of 3-4 cases / 100.000 (Kumar, Pickard et al. 2021). FL derives from the clonal expansion of neoplastic B cells with a germinal center (GC) phenotype (Victoria, Dominguez-Sola et al. 2012, Basso and Dalla-Favera 2015, Carbone, Roulland et al. 2019). There is high heterogeneity in the clinical spectrum and molecular phenotype of FL (Weigert and Weinstock 2017, Perrett and Okosun 2021), rendering it a challenging disease in the clinics and research.

1.1.1 Clinical perspective of FL

1.1.1.1 Clinical manifestation and diagnosis

FL is typically diagnosed in older adults, with an average age of 65 years, and is slightly more frequent in men (Zoellner, Herfarth et al. 2021). Most patients present with painless peripheral lymphadenopathy. Patients can have constitutional symptoms, including fatigue, night sweats, weight loss, and fever (Nastoupil, Sinha et al. 2012).

To diagnose FL, a histopathological examination is needed, ideally on an entire lymph node. Morphology shows centrocytes and centroblasts in typical follicular structures. Immunohistochemistry shows mature B cells with a GC phenotype, typically positive for CD20, CD19, CD79A, CD10, BCL6 and BCL2 (Zoellner, Herfarth et al. 2021). Fluorescence in situ hybridization (FISH) or molecular studies are usually only needed in cases with atypical features.

Proper staging is needed to determine the most appropriate therapeutic strategy. Staging procedures comprise taking a thorough medical history and physical examination, blood tests, bone marrow biopsy, and imaging, such as computed tomography (CT) with or without positron emission tomography (PET) and -if needed- magnetic resonance imaging (MRI). Patients are then classified by the Ann Arbor system as having limited-stage disease (i.e. stage I or II) or advanced-stage disease (i.e. stage III or IV) (Zoellner, Herfarth et al. 2021).

At the time of diagnosis, most patients present with advanced-stage disease, with involvement of lymph nodes on both sides of the diaphragm and/or diffuse infiltration of extranodal sites, including the bone marrow (Ann Arbor stages III-IV). While patients with limited-stage disease (Ann Arbor I – II) can achieve long-term remissions with radiation-based therapies, patients with advanced-stage disease are still considered incurable with current standard therapies. Overall, the median survival of patients with FL is approaching two decades. However, patients typically have chronically relapsing clinical course with progressively shorter durations of remissions. Furthermore, a subset of patients has early progression and/or transformation to an aggressive clinical course with significantly shorter survival (Mounier, Bossard et al. 2015).

1.1.1.2 Therapeutic regimens

One of the major determinants in the management of patients with FL is the stage of the disease at the time of diagnosis. Patients diagnosed with limited-stage disease (less than 20% of the cases) can be treated with curative intent. Treatment primarily consists of “involved site” radiotherapy, often in combination with CD20 antibody (Zoellner, Herfarth et al. 2021). If radiotherapy

is not feasible, patients may be candidates for watchful observation (“watch and wait”) or receive systemic treatment. Patients who present with advanced-stage disease will be managed with the intent to alleviate disease-related symptoms and increase progression-free and overall survival. Patients who are asymptomatic with low tumor burden will be managed with “watch and wait”. Patients with symptoms and high tumor burden, depending on their physiological conditions, should be offered a CD20 antibody (e.g. rituximab (R) or obinutuzumab (O)) in combination with standard immunochemotherapy (e.g. CHOP, bendamustine, or CVP). If they are ineligible for chemotherapy, they should be offered CD20 antibody monotherapy, palliative radiation or best supportive care (Dreyling, Ghilmini et al. 2016, Adolph and Weigert 2020, Dreyling, Ghilmini et al. 2021). Currently, molecular- and/or immune-targeting chemotherapy-free treatment regimens are still considered experimental as first line treatment for patients with previously untreated advanced-stage FL, who require therapeutical intervention.

Novel therapeutic options have recently been developed and become increasingly available. Some of them are approved for patients with relapsed and refractory disease, and others are undergoing clinical testing. This includes agents which target specific pathways (e.g., PI3K inhibitors and BTK inhibitors) or which have immunomodulatory effects (e.g., lenalidomide). In addition, new immunotherapies include novel antibodies (e.g. anti-CD19, CD20xCD3 bispecific antibodies) and CD19- and CD20-targeting chimeric antigen receptor (CAR) T cells.

Despite these therapeutic advances, FL is still considered incurable. A subset of patients does not benefit from standard therapies. These patients have a high risk of early relapse and of undergoing histologic transformation. With the current diagnostic and prognostic tools, it is difficult to identify these subsets of high-risk patients. The advance of targeted therapies and immunotherapies highlights the need to understand individual disease biology better. This could help make treatment decisions and develop personalized therapies with low toxicity and high efficacy. Therefore, studies are needed to better define the disease biology and the functional consequences associated with specific genetic alterations.

1.1.2 Molecular perspective of FL

Modern omics technologies have helped define an increasingly comprehensive landscape of molecular alterations that drive the development and progression of FL and determine the biology and clinical course of the disease (Kumar, Pickard et al. 2021). The hallmark t(14;18)(q32;q21) translocation is an early transformative event in FL development and results in constitutive overexpression of antiapoptotic BCL2. The t(14;18) alone is not sufficient for lymphomagenesis, multistep process (Haebe, Keay et al. 2022) characterized by the subsequent acquisition of numerous cell-intrinsic alterations (such as gene mutations, epigenetic dysregulation, etc.) as well as perturbations in the cross-talk between lymphoma cells and their tumor microenvironment (TME) (Basso and Dalla-Favera 2015, Carbone, Roulland et al. 2019).

1.1.2.1 The genetic drivers of FL

The acquisition of the t(14;18)(q32;q21) translocation is considered the earliest transformative event in the development of FL and occurs early during B cell development in the bone marrow (Yunis, Oken et al. 1982). It is found in more than 80% of patients with advanced-stage disease. The t(14;18) translocation results from impaired V(D)J rearrangement and leads to overexpression of BCL2. The juxtaposition of antiapoptotic *BCL2* places it under the transcriptional control of the immunoglobulin heavy chain (*IGH*) enhancer and thereby drives constitutive expression

(Tsujiimoto, Cossman et al. 1985). Circulating clones with a t(14;18) translocation are frequently detected in older patients who have not been diagnosed with FL.

Following bone marrow exit, t(14;18)+ B cells enter the GC of secondary lymphoid organs, where they encounter antigens (Ag) and undergo multiple rounds of somatic hypermutation (SHM) and class-switch recombination (CSR), subsequently constituting the so-called FL-like cells (FLLCs) (Carbone, Roulland et al. 2019). FLLCs iteratively re-enter the GC reaction, acquire additional oncogenic mutations and expand clonally while evading immune selection (Roulland, Faroudi et al. 2011, Kridel, Sehn et al. 2012) (**Figure 1**).

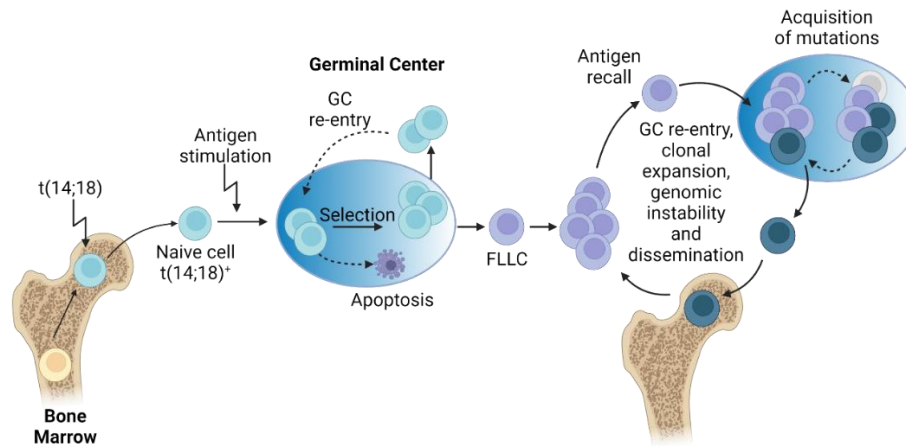


Figure 1. The multistep process of lymphomagenesis. Naïve B cells acquire the t(14;18) translocation in the bone marrow due to aberrant V(D)J rearrangement. They acquire additional mutations in the germinal center of secondary lymphoid organs. Here, they undergo various rounds of SHM and CSR and clonally expand, giving origin to FL-like cells (FLLC) (adapted from (Carbone, Roulland et al. 2019)).

Recurrent genetic mutations in FL are well described. Together with *BCL2* translocations, the loss-of-function mutations of *KMT2D* and *CREBBP* are identified in 80% of the patients (Weigert and Weinstock 2017). Several other frequent gene mutations are detected in FL, likely affecting the disease biology and patients outcome. Yet, their specific contribution to the molecular ontogeny of the disease remains to be thoroughly investigated.

1.1.2.2 Epigenetic dysregulation in FL

Somatic mutations affecting epigenetic regulators are the most recurrent in FL. These include histone modifiers and chromatin remodeling factors (Morin, Mendez-Lago et al. 2011, Okosun, Bödör et al. 2014, Korfi, Ali et al. 2017, Weigert and Weinstock 2017, de Leval, Alizadeh et al. 2022). As depicted below (**Figure 2**), *KMT2D*, *CREBBP*, *EZH2*, and *EP300* are the most frequently mutated histone-modifying genes (Pastore, Jurinovic et al. 2015). *ARID1A* is the most commonly mutated chromatin remodeling factor. *ARID1A* mutations are mostly disruptive (i.e. frame-shift, nonsense, or splice-site mutations) and found in up to 15% of FL at initial diagnosis (Pastore, Jurinovic et al. 2015).

Primary cases frequently harbor more than one genetic mutation affecting genes coding for epigenetic modifiers, indicating that epigenetic dysregulation is a hallmark of FL.

1.1.2.3 Re-education of the tumor microenvironment in FL

FL cells dynamically interact and re-educate their surrounding tumor microenvironment, including follicular dendritic cells and immune cells (e.g. T follicular helper cells), to support their growth and to escape negative selection (Gascoyne, Nadel et al. 2017).

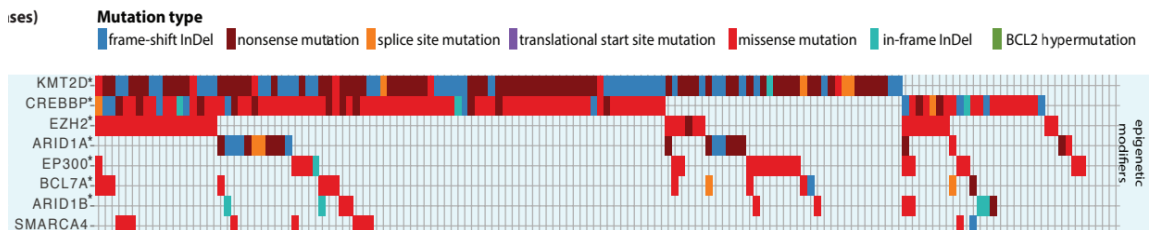


Figure 2. Mutational profile of diagnostic FL biopsies from patients of the GLSG2000 cohort. Adapted from (Pastore, Jurinovic et al. 2015)

GC immunosurveillance is critical in lymphomagenesis. During the GC reaction, cells with a low BCR affinity are selected to undergo apoptosis after interaction with follicular dendritic cells (FDCs). Negative B cell selection involves FAS-FASLG-induced apoptosis (**Figure 3**). Aberrant FAS signaling and checkpoint evasion results in the proliferation and clonal expansion of potentially malignant subgroup of B cells, called FLLCs (Takahashi, Ohta et al. 2001, Hao, Duncan et al. 2008, Butt, Chan et al. 2015). FLLCs undergo multiple rounds of SHM, escaping the canonical antigen-dependent regulation.

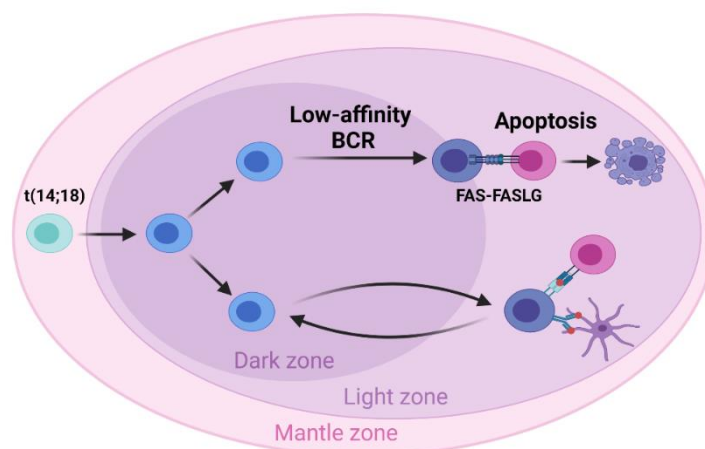


Figure 3. Germinal center reaction. B cells with low BCR affinity are negatively selected in the GC via FAS-FASLG-induced apoptosis.

1.2 AT-rich interaction domain 1A (ARID1A) and the SWI/SNF complex

1.2.1 Epigenetics: a short introduction

Epigenetics functionally alters the genome without changing the nucleotide sequence. Epigenetic regulation occurs at different levels and includes DNA methylation, histone modification, and chromatin remodeling. Here, I will focus on chromatin remodeling, specifically on ARID1A – a subunit of the SWI/SNF complex, in FL.

ARID1A is part of a mammalian SWItch/Sucrose Non-Fermentable (SWI/SNF) complex. SWI/SNF complexes are large multisubunit complexes, highly conserved. Their function is nucleosome remodeling, which determines chromatin accessibility alteration, and modulates gene transcription in an ATP-dependent manner (Wilson and Roberts 2011).

Nucleosomes are the major components of chromatin and enable DNA condensation. Each nucleosome consists of eight histones, known as histone octamer, with nearly two turns of DNA wrapped around. The nucleosomes are compacted and organized in a well-defined yet dynamic structure. Nucleosome mobilization and chromatin remodeling are critical mechanisms in gene transcription regulation.

1.2.2 The chromatin remodeling role of the SWI/SNF complexes

Remodeling chromatin accessibility is the primary function of the SWI/SNF complexes. They can relax or compact the chromatin structure by mobilizing nucleosomes. Nucleosomes are stable structures consisting of many weak histone–DNA interactions (Luger and Richmond 1998), which require biochemical energy to be broken. Nucleosome remodeling involves the alteration of these histone–DNA interactions. Typically, the nucleosome can slide along the chromatin and be ejected or inserted in specific regions (Wilson and Roberts 2011). The SWI/SNF complex subunits have particular functions. ARID1A targets DNA sequences AT-rich, and another subunit, BRG1, breaks the interaction between DNA and the histone octamer. BRG1 has an ATPase function and, by promoting ATP-hydrolysis, produces the energy necessary for histones mobilization (Alfert, Moreno et al. 2019).

The SWI/SNF complexes have a dual function, as they can either activate or repress gene expression (Figure 4). The specific role is determined by the nucleosome position, and the other molecules recruited to the site of action. On the one hand, if the complex is targeted to the transcription-starting site (TSS) of a gene, it can mobilize the histones and render the TSS accessible for the RNA polymerase and other elements to bind and initiate transcription. On the other hand, it can act as a repressor by occupying the TSS or recruiting co-repressor complexes or histone deacetylases, which remove the activation markers from the histone tails (Wilson and Roberts 2011, Alfert, Moreno et al. 2019).



Figure 4. Transcription regulation by the SWI/SNF complex. The positioning of the SWI/SNF complex and the nucleosomes at the TSS (arrow) is crucial to determine gene transcription. As well as the recruitment of activator or repressor complexes (adapted from Wilson and Roberts, 2011).

The SWI/SNF complexes play an essential role in regulating gene transcription by controlling chromatin accessibility, including the possibility of transcription and co-transcription factors to bind to DNA (Clapier, Iwasa et al. 2017). Mutations affecting subunits of this complex have been reported to be highly recurrent across cancers and shown to promote tumorigenesis (Kadoch and Crabtree 2015). Exome sequencing data show that subunit-specific mutations vary across cancer entities, indicating context-specific functions of the different SWI/SNF components (Kadoch and Crabtree 2015).

1.2.3 The SWI/SNF complexes: BAF and PBAF

Chromatin remodeling is evolutionary highly conserved. Homologs of the mammalian SWI/SNF complex were first identified in *Saccharomyces cerevisiae* and *Drosophila melanogaster*. In yeast, they were described in genetic screens for identification of essential factors in sucrose metabolism (SNF, sucrose non-fermenting) and mating type switch (SWItch) (Neigeborn and Carlson 1984, Stern 1984). In *Drosophila melanogaster*, this complex was found to be responsible for embryonic development, specifically body segmentation (Kennison and Tamkun 1988).

The mammalian SWI/SNF complexes (Wilson and Roberts 2011) are ubiquitously expressed and formed by assembling several subunits (**Figure 5**). Two major subclasses of this complex are the BRG1-associated factor (BAF) complex and the polybromo BRG1-associated factor (PBAF) complex. They consist of one ATPase catalytic subunit (BRM or BRG1), a set of conserved core subunits, and variable subunits responsible for the targeting, assembly and regulation of lineage-specific functions. The BAF complex is characterized by the presence of ARID1A or ARID1B, mutually exclusive. The PBAF complex comprises three unique subunits BAF200, BAF180, and BRD7.

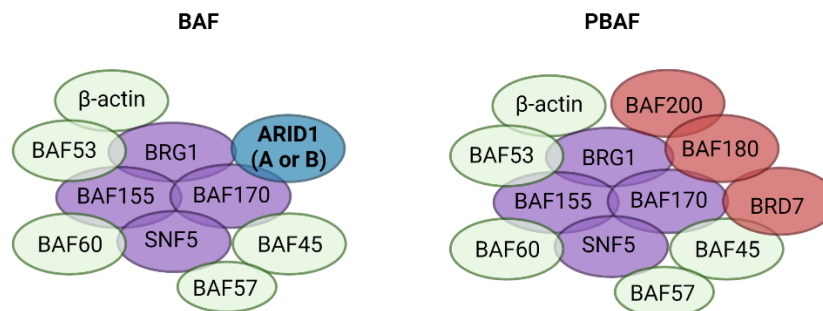


Figure 5. Composition of the SWI/SNF complexes. BAF and PBAF comprise the two major subclasses of SWI/SNF complexes. They consist of a core of conserved subunits (purple) and variable subunits (green). In addition, there are complex-specific subunits, ARID1A or ARID1B (blue) that are BAF-specific, and BAF200, BAF180, and BRD7 (red) that are PBAF-specific (adapted from Wilson, 2011).

1.2.4 ARID1A mutations are recurrent across cancers and inactivating

ARID1A, and its homologs ARID1B and ARID2, are the mammalian SWI/SNF complexes subunits with the function of binding to the DNA. They are characterized by a 100-amino acid DNA binding domain ARID to target DNA regions rich in AT nucleotides. Thereafter, the protein is named ARID1A, AT-rich interaction domain 1A (Wu and Roberts 2013). ARID1A is involved in several critical cellular functions. It plays a pivotal role mainly in double-strand breaks (DSB) repair (Shen, Peng et al. 2015), but also in controlling the nonhomologous end joining repair (NHEJ) pathway (Bararia, Heide et al. 2014). As part of a chromatin remodeling complex, ARID1A regulates the transcription of several genes and pathways, as we will discuss below.

1.2.4.1 ARID1A mutations in cancer

ARID1A and other members of the SWI/SNF complexes are recurrently mutated in cancer. Mutations in subunits of the SWI/SNF complexes were identified in 20% of cancer patients (Kadoch, Hargreaves et al. 2013).

ARID1A is the most commonly mutated SWI/SNF gene across different tumor types (Mathur 2018). Pan-cancer analyses reported ARID1A to have a mutation frequency of 6% across all

samples (Jiang, Chen et al. 2020, Mullen, Kato et al. 2021). *ARID1A* mutations are mostly disruptive (i.e. frame-shift, nonsense, and splice-site), heterozygous, with no specific hotspot, and result in protein haploinsufficiency (Wu and Roberts 2013, Kadoch and Crabtree 2015, Pavlidou and Balis 2020). The high frequency of inactivating mutations in *ARID1A* suggests that it functions as a *bona fide* tumor suppressor (Jones, Wang et al. 2010, Birnbaum, Adélaïde et al. 2011, Wang, Kan et al. 2011, Wiegand, Lee et al. 2011, Abe, Maeda et al. 2012, Fujimoto, Totoki et al. 2012, Guichard, Amaddeo et al. 2012, Huang, Deng et al. 2012, Jones, Li et al. 2012, Mamo, Cavallone et al. 2012, Shain, Giacomini et al. 2012, Zang, Cutcutache et al. 2012, Wu and Roberts 2013).

Even though inactivating *ARID1A* mutations are recurrent across cancers, tumors' specific molecular and functional consequences are incompletely understood.

1.2.4.2 *ARID1A* mutations in FL

ARID1A mutations in FL were first suggested to be functionally relevant in a case of convergent evolution. Specifically, following an allogeneic bone marrow transplantation, both the donor and the recipient developed FLs, which evolved from a common precursor clone (Weigert, Kopp et al. 2012). Both FLs showed *ARID1A* loss, yet through independently acquired mutations. The recipient's FL harbored a premature stop codon in *ARID1A*, while the donor's FL showed *ARID1A* copy number loss.

Subsequently, Pastore and colleagues (Pastore, Jurinovic et al. 2015) showed that *ARID1A* mutations in FL are highly recurrent. Specifically, in a cohort of patients with advanced-stage FL (GLSG2000), *ARID1A* was mutated in 15% of diagnostic biopsies, ranking among the most recurrent mutations. The mutations were mainly monoallelic and disruptive (frame-shift, nonsense, and splice-site) and were shown to result in reduced *ARID1A* protein expression (Weigert, Kopp et al. 2012).

ARID1A mutations have been shown to be clinically relevant in FL. Specifically, *ARID1A* mutation status is a component of the clinicogenetic risk models that have been shown to improve the stratification of patients who receive standard immunochemotherapy like R-CHOP or R-CVP as frontline treatment for advanced-stage FL (Pastore, Jurinovic et al. 2015, Jurinovic et al., Blood 2016).

ARID1A mutations are described to have both functional and clinical relevance in FL. Therefore, we decided to focus on the functional characterization of *ARID1A* mutations in human FL model systems.

2. Aims of the study

ARID1A mutations are among the most recurrent mutations in FL (Pastore, Jurinovic et al. 2015). Previously published data suggest that they have functional relevance (Weigert, Kopp et al. 2012) and clinical relevance (Weigert and Weinstock 2017). Yet, little is known about the molecular and functional downstream effects upon *ARID1A* loss in FL.

The overall aim of this study is to functionally characterize *ARID1A* mutations in FL. We decided to investigate the impact of *ARID1A* loss mutations in *ex vivo* model systems of human FL. I had the following specific working steps:

1. Re-analysis of the mutational landscape of *ARID1A* and other SWI/SNF genes in a large cohort of primary FL biopsies.
2. Identification and generation of suitable *ex vivo* FL model systems with and without *ARID1A* loss.
3. Transcriptional profiling of FL-like cells with and without *ARID1A* loss to identify mutation-specific phenotypes for further functional studies.
4. Functional characterization of the following transcriptional phenotypes that we identified to be linked to *ARID1A* loss:
 - a. Reduced cell growth and cell division
 - b. Resistance to FASLG-induced apoptosis
 - c. Impact on the interaction of FL-like cells and T cells

3. Material and Methods

3.1 Material

3.1.1 Chemicals, reagents, and media

Table 1. List of used chemicals, reagents, and media

Chemicals, media, and reagents	Supplier
7-AAD Viability solution	BioLegend
Advanced RPMI1640	ThermoFisher Scientific
Agarose Molecular Grade	Bioline
Select agar	Sigma-Aldrich
BD Annexin V Binding Buffer, 10x concentrate	BD Biosciences
Ampicillin	Carl Roth
Anti-Anti 100x	Gibco
Anti-human IgD-biotin, clone: IADB6	SouthernBiotech
Ascorbic acid	Sigma-Aldrich
Bolt™ Antioxidant	Novex
BD CellFIX, 10x concentrate	BD Biosciences
Anti-human CD44– biotin, clone: F10-44-2	SouthernBiotech
CD90.1 Microbeads	Miltenyi Biotec
Clarity Western ECL Substrate	Bio-Rad Laboratories
Collagenase Type 4	Worthington
CytoStim™, human	Miltenyi Biotec
DMEM	PAN
DMSO - Dimethyl sulfoxide	Sigma-Aldrich
DNase I (6316,7 U/mg)	AppliChem
DNase I recombinant, RNase-free	Roche
Dpnl	New England Biolabs
DMEM	Biochrom
Dulbecco's Phosphate Buffered Saline (PBS)	Gibco®
Dynabeads® Human T-Activator CD3/CD28	Gibco®
5-Ethynyl-2'-deoxyuridine (EdU)	Lumiprobe
Ethylenediaminetetraacetic acid (EDTA), 0.5 M, pH 8.0	Merck
Ethanol, pure	Merck
FACS Clean	BD Biosciences
FACS Flow	BD Biosciences
FACS Rinse	BD Biosciences
Fast SYBR™ Green Master Mix	ThermoFisher Scientific
Fetal calf sera (FCS)	PAN-Biotech
Formaldehyde 4%	ThermoFisher Scientific
Gel Loading Dye, Purple (6x), no SDS	New England Biolabs
GlutaMAX™	ThermoFisher Scientific
Glycine	Carl Roth
Hank's Balanced Salt Solution (HBSS)	Gibco®
HEPES Buffer 1M	Biochrom
Human serum albumin (HSA)	Biotest, Octapharma AG
Human serum type AB	c.c.pro

Table 1 - continued

Hydrogen peroxide (H ₂ O ₂)	Merck
IMDM	PAN™ BIOTECH
Pierce IP Lysis Buffer	ThermoFisher Scientific
2-Propanol, ROTIPURAN® (Isopropanol)	Carl Roth
LB-Agar (Lennox)	Carl Roth
LB-Medium (Lennox)	Carl Roth
Laemmli Sample Buffer 4x	Bio-Rad Laboratories
MgCl ₂ - Magnesiumchloride 1M	ThermoFisher Scientific
Mini-PROTEAN TGX Precast Protein Gels, 12-well	Bio-Rad Laboratories
Methanol, pure	Merck
β-mercaptoethanol (β-ME)	Carl Roth
β-mercaptoethanol (β-ME) for cell culture (50 mM)	Gibco®
Mitomycin C (10 mg)	Tocris
Bolt™ MOPS SDS Running Buffer 20x	Novex
NEBNext® High-Fidelity 2X PCR Master Mix	New England BioLabs
Nocodazole	Sigma-Aldrich
Nonfat milk powder	Carl Roth
NP40 Substitute	Ambion
Nuclease-Free-Water	Ambion
Nucleofector™ solution V	Lonza
One Shot™ TOP10 Chemically Competent <i>E. coli</i>	Invitrogen
One Shot™ Stbl3™ Chemically Competent <i>E. coli</i>	Invitrogen
Opti-MEM® I	Gibco®
Pancoll human (lymphocyte separating solution, density: 1.077 g/ml)	PAN-Biotech
Passive Lysis Buffer, 5x	Promega
PenStrep (Penicillin 10.000 U/mL, Streptomycin 10.000 µg/ml)	Gibco®
Phosphatase Inhibitor Cocktail 2	Sigma-Aldrich
Phosphatase Inhibitor Cocktail 3	Sigma-Aldrich
Polybrene Transfection Reagent	Merck Millipore
Poly-L-Lysine solution	Sigma-Aldrich
Protease inhibitor cocktail	Sigma-Aldrich
Pierce™ IP Lysis buffer	ThermoFisher Scientific
Pierce™ RIPA buffer	ThermoFisher Scientific
Restore™ Plus Western Blot Stripping Buffer	ThermoFisher Scientific
Roti®-Safe Gel stain	Carl Roth
Roti®garose	Carl Roth
RPMI1640, without L-Glutamine	PAN-Biotech
Bolt™ Sample Reducing Agent 10x	Novex
S.O.C Medium	Invitrogen
NaCl - Sodium chloride	Merck
SDS - Sodium dodecyl sulfate	Merck
NaF - Sodium fluoride	Merck
Na ₃ VO ₄ - Sodium orthovanadate	Sigma-Aldrich
Sodium pyruvate (100 mM)	PAN-Biotech
CuSO ₄ - Copper sulfate solution	Sigma-Aldrich
Sulfo Cyanine 5-azide	Lumiprobe
FASLIGAND® Protein (soluble) (human), (recombinant)	Enzo
SureBeads™ Protein G Magnetic Beads	Bio-Rad Laboratories

Table 1 - continued

TaqMan™ Fast Advanced Master Mix	ThermoFisher Scientific
TBE buffer 10x	Invitrogen
TBS Buffer 10x, pH 8.0	In-house
TexMACS Medium	Miltenyi Biotec
Tris(hydroxymethyl)-aminomethane (Tris), pH 8.8	Serva
UltraPure™ 1 M Tris-HCl-Buffer, pH 7.5	ThermoFisher Scientific
Triton X-100	Merck
Trypan Blue Stain Solution, 0.4 %	Gibco®
Trypsin-EDTA (0.5 %) in DPBS 10x	Gibco®
Tween20	Merck

3.1.2 Consumables

Table 2. List of used consumables

Consumables	Manufacturer
Bacterial plates	Carl Roth
Bacterial spreaders	Carl Roth
Bolt™ 4-12% Bis-Tris Plus Gels, 10- and 12-wells	Invitrogen
Cell strainer (40 µm, 70 µm; Nylon)	Falcon® (Corning)
Centrifuge tubes (0.5 ml, 1.5 ml, 2.0 ml)	Eppendorf, Sarstedt
Combitips advanced (0.2 ml, 0.5 ml, 2.5 ml, 5 ml, 10 ml)	Eppendorf
DURAN® flask	Schott
Epredia™ Cytoslide™, coated with circle	Erpedia
Filter tips (10 µl, 100 µl, 200 µl, 1.000 µl)	Biozym
Flow-cytometry tubes	Sarstedt, Falcon® (Corning)
gentleMACS C tubes	Miltenyi Biotec
LS cell separation columns	Miltenyi Biotec
Hard-Shell PCR Plates	Bio-Rad Laboratories
Ibidi 8 well µSlide (Glass Bottom)	Ibidi
Ibidi µ-Slide VI 0.4	Ibidi
MicroAmp Clear Adhesive Film	ThermoFisher Scientific
Microscope Slide Coverslips, Glass, 22mm x 22mm	Polyscience
PARAFILM®	Sigma-Aldrich
PCR strip tubes and caps (Multiply)	Sarstedt
Pipettes Pasteur	Hartenstein
Pipette tips (10 µl, 100 µl, 200 µl, 1.000 µl)	Starlab
Power Blotter Select PVDF Transfer sandwich	ThermoFisher Scientific
Reservoir reagent	Corning
Screw cap sterile tubes (15 ml, 50 ml)	Falcon® (Corning)
Serological pipettes (5 ml, 10 ml, 25 ml, 50 ml)	Corning, Greiner Bio-One Int.
Standard Cell culture plate (6-, 12-, and 24-well)	Sarstedt
Standard Culture flasks, Vent. Cap, (T25, T75, T175)	Sarstedt
Stericup® Filter Units (0.22 µm)	Merck Millipore
Sterifix® filter (0.2 µm) and syringes	Braun
Suspension Culture flasks, Vent. Cap, (T25, T75, T175)	Sarstedt
Suspension Cell culture plate (6-, 12-, and 24-well)	Sarstedt
96-well tissue culture-treated plates (U-bottom)	Falcon® (Corning)

3.1.3 Equipment

Table 3. List of used equipment

Equipment	Manufacturer
Analytical balance	Kern&Sohn
Autoclave VX-150	Systec
Autoclave VARIOKLAV® Typ 500	HP Medizintechnik
Benchtop Shaker, Titramax 101	Heidolph Instruments
BD FACSCanto™ II flow cytometer	BD Bioscience
Bioruptor® Pico sonication device	Diagenode
Table top Centrifuges	Eppendorf
Centrifuge Heraeus™ Multifuge™ X1R	ThermoFisher Scientific
CO ₂ Incubator CB 220	Binder
E-BOX VX2, Gel documentation system	Vilber Lourmat
Easypet / Pipetboy	Eppendorf
EasySep™ Magnet	Stemcell Biotechnologies
FlowSafe® B-[MaxPro] ² -130, Laminar Flow Cabinet	Berner Safety
Fluorescence Microscope DMI8	Leica
Fluorescence Microscope BZ-X	Kyence
Freezer GNP 3056 Premium	Liebherr
Freezer HERAFreeze™ HFU240BV	ThermoFisher Scientific
Fusion SL, Gel Chemiluminescence imaging system	Vilber Lourmat
gentleMACS Dissociator	Miltenyi Biotec
GloMax® Discover, Microplate reader	Promega
Hemocytometer (Neubauer chamber, improved)	Marienfeld
Ice machine, FM-170AKE	Hoshizaki
Inverted Phase Contrast Microscope ID03	Zeiss
LS Columns (MACS)	Miltenyi Biotec
Magnetic stirrer, IKAMAG R RET	IKA-Werke
MidiMACS™ and QuadroMACS™ Separators	Miltenyi Biotec
Mini-PROTEAN Tetra Cell vertical gel electrophoresis system	Bio-Rad Laboratories
Mr. Frosty® Freezing container, Cryo 1°C	Nalgene®
Multipettes® (M4, plus, stream)	Eppendorf
NanoDrop 1000, Spectrophotometer	ThermoFisher Scientific
nCounter Pro Analysis System	Nanostring
nCounter SPRINT Profiler	Nanostring
Nucleofector™2b	Lonza
PowerPac™ Basic, Gel chamber power supply	Bio-Rad Laboratories
Pipettes	Eppendorf
PowerPac™ Basic Power Supplies	Bio-Rad Laboratories
QuadroMACS Separator and MACS MultiStand	Miltenyi Biotec
Shandon Cytospin 2	Marshall Scientific
C1000 Touch Screen PCR Thermal Cycler	Bio-Rad Laboratories
CFX96 Touch Real-Time PCR Detection System	Bio-Rad Laboratories
ThermoMixer® C	Eppendorf
Trans-Blot® Turbo™ Transfer System	Bio-Rad Laboratories
Vi-CELL™ XR, Cell counting and cell viability	Beckman Counter
Vortex-Genie 2	Scientific Industries
Precision™ Coliform-Water bath	ThermoFisher Scientific

3.1.4 Kits

Table 4. List of used kits

Kit	Manufacturer
BD Cytotfix/Cytoperm™ Fixation/Permeabilization Kit	BD Biosciences
B Cell Isolation Kit II, human	Miltenyi Biotec
Direct-zol™ RNA MicroPrep kit	Zymo Research
Dual-Glo® Luciferase Assay	Promega
EasySep™ Human CD19 Positive Selection Kit II	Stemcell Biotechnologies
EasySep™ Human CD4+ T Cell Isolation Kit	Stemcell Biotechnologies
EasySep™ Human CD8+ T Cell Isolation Kit	Stemcell Biotechnologies
EasySep™ Human T Cell Isolation Kit	Stemcell Biotechnologies
HighPrep™ PCR Clean-Up Kit	Sigma-Aldrich
Illumina Tagment DNA TDE1 Enzyme and Buffer Kit	Illumina
iProof High-Fidelity PCR Kit	Bio-Rad Laboratories
iScript™ Select cDNA Synthesis Kit	Bio-Rad Laboratories
KAPA HiFi PCR Kit	Roche
KAPA Library Quantification Kit	Roche
LEGENDplex™ Human B Cell Panel (13-plex)	BioLegend
MinElute PCR Purification Kit	Qiagen
PE Annexin V Apoptosis Detection Kit I	BD Bioscience
Pierce™ BCA Protein Assay Kit	ThermoFisher Scientific
Pierce™ Cell Surface Protein Isolation Kit	ThermoFisher Scientific
PureYield™ Plasmid Midiprep System	Promega
QIAamp® DNA Blood Mini Kit	Qiagen
QIAquick® Gel Extraction Kit	Qiagen
SuperScript® III First-Strand Synthesis System for RT-PCR	Invitrogen

3.1.5 Standards

Table 5. Protein standards and DNA ladder

Standard	Supplier
Bovine Serum Albumin (BSA), Set Protein Assay Standards	ThermoFisher Scientific
MagicMark™ XP	Invitrogen
PageRuler™ Plus Prestained Protein Ladder, 10-250 kDa	ThermoFisher Scientific
Quick-Load® 1 kb DNA ladder	New England Biolabs

3.1.6 Buffers and Solutions

Table 6. Buffers, solutions, and their composition

Buffer and Solution	Concentration	Composition
BCM20	20 %	FCS
	1 %	PenStrep
	1 %	GlutaMAX In Advanced RPMI 1640
FCS/DMSO	10 %	DMSO in FCS
Feeder Media	10 %	FCS
	1 %	PenStrep In RPMI 1640 (w Glutamine)

Table 6 - continued

Co-IP buffer (wash buffer same)	0,25 x 0,25 x 0,25 x	Protease inhibitor cocktail Phosphatase inhibitor cocktail 2 Phosphatase inhibitor cocktail 3 In Pierce IP Lysis buffer
5 % nonfat milk solution	5 %	Nonfat milk powder in TBS/Tween
MACS buffer	1 mM 2 %	EDTA HSA In 1x PBS
PBS/FCS	10%	FCS in 1x PBS
RIPA lysis buffer	25 mM 150 mM 1 % 1 x 1 x 1 x	Tris-HCl, pH 7.6 NaCl sodium deoxycholate Protease inhibitor cocktail Phosphatase inhibitor cocktail 2 Phosphatase inhibitor cocktail 3
TBS/Tween	1 %	Tween20 in 1x TBS
Transfer buffer	1 x 10 % 1 %	20x Bolt™ Transfer Buffer Ultrapure methanol Bolt™ Antioxidant In DI water

3.1.7 Fluorescent Dyes

Table 7. Fluorescent dyes used for cell monitoring by FACS

Dye	Fluorescence	Supplier
AnnexinV APC	APC	BioLegend
AnnexinV PE	PE	BD Bioscience
CFSE - 5(6)-Carboxyfluorescein diacetate N-succinimidyl ester	FITC	Sigma-Aldrich
VPD - Violet proliferation dye 450	BV™ 421	BD Bioscience

3.1.8 Antibodies

3.1.8.1 Antibodies used for Western blot analysis and co-IP

Table 8. Primary and secondary antibodies used for Western blot

Antibody	Supplier	Specie	Clone	Dilution	Cat #
ARID1A	Sigma-Aldrich	rabbit	Polyclonal	1:2.500	HPA005456
RUNX3	BioLegend	mouse	R3-5GA	1:2.000	697902
ETS1	Cell Signaling	rabbit	D8O8A	1:2.000	14069
GAPDH	Thermo Fisher	mouse	6C5	1:10.000	AM4300
anti-Mouse IgG (H+L), HRP	Thermo Fisher	goat	Polyclonal	1:5.000	31430
anti-Rabbit IgG (H+L), HRP	Thermo Fisher	goat	Polyclonal	1:5.000	31460

3.1.8.2 Antibodies used for Flow-cytometry analysis

Table 9. Directly labeled antibodies used for cell monitoring by FACS

Antibody	Supplier	Specie	Clone	Conjugate	Dilution	Cat #
CD95 (FAS)	BioLegend	Mouse	DX2	PE	1:25	305608
CD95 (FAS)	BioLegend	Mouse	DX2	Alexa 647	1:50	305618
CD19	BioLegend	Mouse	HIB19	PE/Cyanine7	1:200	302216
CD19	BioLegend	Mouse	V CD19.11	BV510	1:200	302242
CD10	BD Pharmingen	Mouse	HI10a	APC	1:100	332777
CD20	Miltenyi Biotec	Cell line	REA780	APC-Vio 770	1:100	1301113 41
CD38	BioLegend	Rat	90	BV421	1:200	102732
CD2	BioLegend	Mouse	TS1/8	PerCP/Cy5.5	1:200	309225
CD4	BioLegend	Rat	GK1.5	APC	1:100	100411
CD8a	BioLegend	Mouse	SK1	BV510	1:100	344732
CD8a	BioLegend	Mouse	RPA-T8	APC/Cyanine7	1:100	301015
CD56	BioLegend	Mouse	5.1H11	PE/Cyanine7	1:100	362510
CD25	BioLegend	Mouse	M-A251	BV510	1:100	356119
CD25	BioLegend	Mouse	M-A251	APC/Cyanine7	1:100	356121
CD45RA	BioLegend	Mouse	HI100	PE/Cyanine7	1:100	304125
HLA-DR DP DQ (MHC II)	BioLegend	Mouse	Tü39	PE/Cyanine7	1:100	361708
HLA-A/B/C (MHC I)	BioLegend	Mouse	W6/32	APC	1:100	311410

3.1.8.3 Antibodies used for immunohistochemistry

Table 10. Antibodies used for IHC

Antibody	Supplier	Specie	Clone	Dilution	Cat #
FAS	Abcam	Rabbit	EP208	1:100	
CD3	Zytomed	Rabbit	SP7	1:150	ZYT-RBK024-05
CD20	Cell Marque	Mouse	L26	1:200	120M-85

3.1.9 Oligonucleotides

Table 11. List of used oligonucleotides and their application

Name	Sequence 5'-3'	Application	Reference
ARID1A_Q200st_F	GCGGGGCCCCAG- TAGAACTCTCACG	CRISPR/Cas9	Benchling
ARID1A_Q200st_R	CGCCCCGGGGTTCATC TTGAGAGTGC	CRISPR/Cas9	Benchling
ARID1A_Q2176fs_F	TTGGAAACCCTCAG- CAAACCTC	CRISPR/Cas9	Benchling
ARID1A_Q2176fs_R	GTTGCCGA- TACTGCCCTTC	CRISPR/Cas9	Benchling
M13 forward	GTA AACGACGGCCA G	Sanger sequencing	ThermoFisher Scientific #N52002
ARID1A_TOPO_F	GTTGAAATGCCTGTG TGGCA	TOPO TA cloning	ThermoFisher Scientific #A15629
ARID1A_TOPO_R	CAATATGCCACCTCA GGTTGG	TOPO TA cloning	ThermoFisher Scientific #A15630

Table 11 - continued

FASprom_P1_F	CCGCTCGAGCCCCGC AAGTCTTTCTCTGA	Luciferase assay	This work
FASprom_P1_R	CCCAAGCTTCGGGAC TAAGACGGGGTAAG	Luciferase assay	This work
FASprom_P2_F	CCGCTCGAGCTGAAG TGAGCATGCCAG C	Luciferase assay	This work
FASprom_P2_R	CCCAAGCTTGTGTGT TCCGTGCCAGTG	Luciferase assay	This work

All oligonucleotides designed with Benchling were purchased from Metabion.

3.1.10 Short hairpin RNA plasmid

Table 12. List of short hairpin RNA plasmids

Vector	Target gene	Catalog ID	Supplier
pTRIPz	Non-target	RHS4750	Horizon
pTRIPz	ARID1A	RHS4696-200767038	Horizon

3.1.11 Plasmid

Table 13. List of used plasmid

Name	Description	Supplier
psPAX2	2nd generation lentiviral packaging plasmid.	Addgene #12260
phCMV-GALV-MTR	Retro and Lentiviral transduction of primary human germinal center B cells. Viral envelope.	Addgene #163612
pSpCas9(BB)-2A-GFP	Cas9 from <i>S. pyogenes</i> with 2A-EGFP and cloning backbone for sgRNA.	Addgene #48138
pHAGE-CMV-MCS-ARID1Awt-IHRES – ZsGreen	Lentiviral expression of ARID1A <i>wild-type</i> in human cell lines	In house
pHAGE-CMV-MCS-Gw-IHRES-ZsGreen -ARID1A Q200	Transient transfection of a stop codon at position Q200, together with Cas9	In house
pHAGE-CMV-MCS-Gw-IHRES-ZsGreen - ARID1A Q1276	Transient transfection of stop codon at position Q1276, together with Cas9	In house
pGL3-basic vector	Luciferase reporter vector for quantitative analysis of regulatory elements	Promega #E1751
pRL-CMV-Renilla	Wild-Type Renilla Luciferase for Normalization in Reporter Assays	Promega #EE2261
pTet-O-RUNX3-T2A-PuroR	Lentiviral expression of RUNX3 under the control of the TetON promoter	Addgene #162349
pDONR223_ETS1_WT	Gateway Donor vector containing ETS1	Addgene #82118

3.1.12 Primary patients data

Primary patients' data were analyzed with the support of Verena Passerini.

Table 14. References to patients' data

Cohort	Reference	GSE number	Purpose of analysis
GLSG2000	(Pastore, Jurinovic et al. 2015)	NA	Identification of <i>ARID1A</i> mutational status
GLSG2000	(Tobin, Keane et al. 2019)	147125	TME sample composition and GSEA analysis (<i>ARID1A</i> WT vs MUT)
CoEvoL	Unpublished in-house study	NA	Analyze <i>ARID1A</i> mutational status at different stages of disease

3.2 Methods

3.2.1 Patients data

3.2.1.1 Analysis of *ARID1A* mutation status

The German Low-Grade Lymphoma Study Group 2000 (GLSG2000) cohort comprised 151 fully evaluable patients enrolled between 2000 and 2010. All patients had advanced-stage FL and received R-CHOP as frontline therapy. Targeted DNA sequencing was available from previous work of our lab (Pastore, Jurinovic et al. 2015). *ARID1A* mutation status was defined using variant allele frequency greater than 0.1. *ARID1A* mutations were classified into two groups, truncating mutations (including nonsense mutations, frameshift and splice site mutations) and missense mutations.

The Co-Evolution (CoEvoL) study cohort comprised 70 primary FL biopsies, from patients diagnosed with advanced-stage FL, before the initiation of frontline therapy, or relapsed and refractory (r/r) disease. *ARID1A* and *FAS* mutation status was defined by targeted DNA sequencing. Non-silent variants (Missense_Mutation, Nonsense_Mutation, Nonstop_Mutation, Splice_Site, Translation_Start_Site) at a variant allele frequency of 0.1 were kept for further investigations.

3.2.1.2 Analysis of FAS protein levels by multispectral immunofluorescence imaging

Material belonging to the GLSG2000 study cohort was assayed. FFPE slides for analysis were prepared as described previously (Bararia, Hildebrand et al. 2020). Briefly, 10µm-thick slices were obtained from tumor microarray samples. FFPE blocks were cut, deparaffinized and dried overnight. After gradual rehydration, slides were incubated with formalin and washed. The staining was performed with antibodies listed in [Table 10](#). Pictures were acquired using the quantitative slide scanner (PerkinElmer) with the Vectra® Polaris 1.0.7 and Phenochart 1.0.8 software. Image quantification was done using the inform 2.4.2 software.

3.2.2 FL-like cell lines model system

B-NHL cell lines, characterized by the t(14;18)(q32;q21)[BCL2/IGH] translocation, were cultured in an incubator with 5% CO₂ at 37°C. OCI-Ly1, OCI-Ly8, and DB, which are *ARID1A* WT, and Karpas422 and WSU, harboring a truncating *ARID1A* mutation, were cultured in IMDM and RPMI1640, respectively. Cell culture media was supplemented with 10% heat-inactivated FCS. All cell lines were authenticated by short tandem repeat profiling (Eurofins) and tested negative for mycoplasma contamination by MycoAlert PLUS mycoplasma detection kit (Lonza).

3.2.2.1 Establishment of *ARID1A* mutant cell lines via CRISPR/Cas9

Deepak Bararia, Eslam Katab and Michale Heide used CRISPR/Cas9-mediated strategy to introduce heterozygous (het) and homozygous (KO) *ARID1A* mutations in the FL-like cell lines OCI-Ly1, OCI-Ly8, and DB. The sgRNAs (listed in [Table 11](#)) were designed by the Benchling CRISPR design online tool (<https://benchling.com>). To generate *ARID1A* mutant cell lines, the sgRNAs

were cloned into the pSpCas9(BB)-2A-GFP backbone (PX458, Addgene plasmid #48138), as described elsewhere (Ran, Hsu et al. 2013).

Nucleofector™ Solution V and the Nucleofector™2b were used to transiently transfect (according to manufacturer's instruction) 10^6 cells with pSpCas9(BB)-2A-GFP co-expressing the sgRNA targeting *ARID1A*. Two days after transfection, GFP+ cells were single-cell sorted into 96-well U-bottom plates. Control clones were generated by transfection of pSpCas9(BB)-2A-GFP only. Clone validation was performed by western blotting and/or TOPO® TA cloning (Table 15).

Table 15. CRISPR/Cas9 cell lines with and without *ARID1A* mutations

Clone	<i>ARID1A</i> status	Validation strategy	Application
DB ctrl#2	WT	WB	Omics
DB ctrl#3	WT	WB	Omics
DB ctrl#7	WT	WB	Omics
DB #B5	Wt / 52 bp del	WB + TOPTA cloning	Omics
DB #C9	Wt / 2 bp + 22 bp del	WB + TOPTA cloning	Omics
DB #H2	Wt / 16 bp del + 64 bp insert	WB + TOPTA cloning	Omics + wet lab
DB #D1	Multiple insert and del	WB + TOPTA cloning	Omics + wet lab
OCI-Ly8 ctrl#3	WT	WB	Omics
OCI-Ly8 ctrl#6	WT	WB	Omics
OCI-Ly8 ctrl#11	WT	WB	Omics
OCI-Ly8 #A9	Wt / 52 bp del	WB + TOPTA cloning	Omics + wet lab
OCI-Ly8 #G5	66 bp and 107 insert	WB + TOPTA cloning	Omics
OCI-Ly8 #G10	Wt / 225 bp del	WB + TOPTA cloning	Omics
OCI-Ly8 #G6	7 bp del / 53 bp del	WB + TOPTA cloning	Omics + wet lab
OCI-Ly1 ctrl#1	WT	WB	Omics
OCI-Ly1 ctrl#7	WT	WB	Omics
OCI-Ly1 ctrl#9	WT	WB	Omics
OCI-Ly1 #F9	Het	WB	Omics + wet lab
OCI-Ly1 #F10	Het	WB	Omics
OCI-Ly1 #E8	KO	WB	Omics
OCI-Ly1 #G1	KO	WB	Omics + wet lab
OCI-Ly1 #H3	KO	WB	Omics

3.2.2.2 TOPO®TA cloning

Clone validation was performed by western blotting and TOPO® TA Cloning® (ThermoFisher). Briefly, sorted single cells were allowed to grow, and subsequently, genomic DNA (gDNA) was

isolated using Blood & Cell Culture DNA Mini Kit (Qiagen), according to the manufacturer's instructions. gDNA was amplified by using ARID1A_TOPO_F and ARID1A_TOPO_R primers listed in [Table 11](#). Following PCR amplification, a single deoxyadenosine (dA) was added to the 3' ends of the PCR products to facilitate the cloning into the linearized pCR™2.1-TOPO® vector. The ligation product was then transformed into One Shot® Top 10 Chemically Competent *E. coli* (ThermoFisher Scientific). Transformed DNA was isolated from a bacterial culture grown in LB media and sequenced using M13 forward primer by Sanger sequencing. TOPO® TA Cloning® was designed and performed by Deepak Bararia and Eslam Katab.

3.2.2.3 Lentivirus production

HEK 293T packaging cells were transfected as described in Caesar et al., 2019 (Caesar, Di Re et al. 2019). Briefly, HEK 293T packaging cells were seeded one day before transfection at a confluency of 50% in a 10 cm dish in DMEM supplied with 10% FCS. On the day of transfection, Opti-MEM was mixed with TransIT-293 and incubated for 10 min at RT. Packaging plasmids (psPAX2, Addgene #12260 and pHCMV-GaL-MTR, kind gift from Dan Hodson, Addgene #163612) and lentiviral construct were added and incubated for 30 min at RT. The mix was then added drop-wise to the cells. Two days after transfection, the media was harvested, spun down and filtered through a low-binding 0.45 µm syringe filter. The virus was concentrated by centrifugation 5.000 x g at 4° C for 24 hrs.

3.2.2.4 Lentiviral over-expression of RUNX3 in FL-like cells

Stable transduction of pTet-O-RUNX3-T2A-PuroR (Addgene #162349) construct for RUNX3 over-expression was performed as described in Caesar et al. (2019 and 2021) (Caesar, Di Re et al. 2019, Caesar, Gao et al. 2021). Briefly, 10⁶ cells were seeded in a 12-well plate, and the concentrated virus was added to the cells with 25 µM HEPES and 10 µg/ml Polybrene. The plate was then centrifuged at 1.500 x g at 32° C for 90 min. After centrifugation, the cells were incubated for several hours before exchanging the media. Successful transduction was validated by western blotting.

3.2.2.5 Puromycin selection

Two rounds of puromycin selection were performed on transduced cells. Each round consisted of 3 to 5 days of puromycin (10 µg/mL for OCI-Ly1 and OCI-Ly8) treatment. For the selection of GC B cells, 6 µg/mL were used. Untransduced control was included to test puromycin selection efficacy.

3.2.2.6 Doxycycline stimulation

To induce the expression of the RUNX3 over-expression vector and of the shRNA for *ARID1A* knockdown, cells were treated with a final concentration of 700 ng/mL doxycycline. Stimulation lasted 48 hrs before cells were analyzed.

3.2.3 *Ex vivo* BCL culture model system

B cell lymphoma-like (BCL) culture and establishment of the *ex vivo* co-culture system were performed with the support and advice of Carolin Strobl.

3.2.3.1 Isolation of MNCs from human tonsils (gentleMACS method)

Isolation of MNCs from human tonsils was performed according to an adapted protocol from www.gentleMACS.com/protocols and Caesar et al., 2021 (Caesar, Gao et al. 2021). Pediatric tonsils were collected after surgery, kept on ice and processed as quickly as possible. Before proceeding with tissue dissociation, the fatty tissue was removed from the tonsil. Tonsils with a maximum weight of 4 gr were cut into pieces and transferred into gentleMACS C tubes with 8 ml warm PBS. 0.5 mg/mL Collagenase Type 4 and 3.000 U/ml DNase I were added to the PBS suspension. The tubes were then applied to the gentleMACS Dissociator, and gentleMACS Program C was run. RPMI 1640 (+10% FCS and + 1% PenStrep) was added (1:1) to the gentleMACS C tube, and the suspension was filtered with a 100 µM nylon filter. The sample was spun down at 1.300 rpm for 6 min, and the pellet was resuspended in 10 mL RPMI 1640 (+10% FCS and + 1% PenStrep). Finally, 14 mL Pancoll density medium (RT) were applied to the cell suspension and centrifuged at 2.000 rpm for 20 min at RT. Acceleration and deceleration of the centrifuge were performed at minimal speed. The upper layer was removed, and the MNC layer at the interphase was harvested. MNCs were diluted 1:2 with cold RPMI 1640 (+10% FCS and + 1% PenStrep) and centrifuged at 1.700 rpm for 10 min at 4°C. Cell count was assessed via a hemocytometer.

3.2.3.2 Germinal center B cells isolation from MNCs

Germinal center B cells isolation from MNCs was performed according to Caesar et al., 2021 (Caesar, Gao et al. 2021). MNCs obtained from tonsil tissue by gentleMACS dissociation were resuspended in MACS buffer. The cell suspension was incubated for 25 min while gentle shaking, with B-cell depletion cocktail, anti-IgD and biotinylated anti-CD44. The sample was pelleted, resuspended in MACS buffer with anti-biotin beads, and incubated for 15 min at 4°C. Afterward, the cells were spun down and resuspended in MACS buffer. The cell suspension was applied to LS columns, previously assembled on MCAS magnetics stands and primed with MACS buffer. The flow-through containing the purified GC B cells was collected and stored.

3.2.3.3 YK6-CD40L-IL21 feeder cells culture

YK6-CD40L-IL21 FCD-like cells, kind gift from Dan Hodson, were cultured in feeder media (see [Table 6](#)), as described in Caesar et al. (2019 and 2021) (Caesar, Di Re et al. 2019, Caesar, Gao et al. 2021). For support culture, FCD-like cells (YK6) engineered to provide essential TME signals, specifically CD40L and IL 21, were treated with mitomycin C (final concentration of 10 µg/mL) for 50 min at 37°C. After treatment, cells were washed twice with PBS and harvested after adding 0.05 % Trypsin/EDTA.

3.2.3.4 BCL cells culture

GC B cells were cultured in BCM20 media (see [Table 6](#)), as described in Caesar *et al.* (2019 and 2021) (Caesar, Di Re et al. 2019, Caesar, Gao et al. 2021). Briefly, a confluent layer of mitomycin C-treated feeder cells was seeded in a cell-culture plate. For long-term culture, the GC B cells were immortalized by transduction of BCL2 and BCL6 using optimized protocols, which allows essentially unlimited growth of these cells. After immortalization, GC B cells were named B cell lymphoma-like (BCL) cells.

For maintenance culture, BCL cells were mechanically resuspended, and the cell suspension was transferred into a conical tube. Cells were spun down (400 x g for 5 min) and washed with PBS.

Cell count was assessed by hemocytometer, and cells were resuspended at the proper density ($5 \times 10^5/\text{mL}$) in BCM20 and plated on the feeder layer.

3.2.3.5 Establishment of *ARID1A* knockdown in BCL cells

BCL cells were further engineered by stable lentiviral expression of short hairpin RNA for *ARID1A* knockdown (Table 12), as described (Caeser, Di Re et al. 2019, Caeser, Gao et al. 2021). Successful transduction was validated by FACS (RFP+) and western blotting.

3.2.4 RNA Sequencing (RNA-Seq)

3.2.4.1 RNA-Seq sample preparation

RNA-Seq library preparation was performed in collaboration with the Enard Laboratory at Anthropology and Human Genomics LMU München.

Twenty-two single cell-derived clones were assayed in DB, OCI-Ly1, and OCI-Ly8. For each cell line, three control clones (ctrl#2, ctrl#3 and ctrl#7 in DB; ctrl#1, ctrl#7, and ctrl#9 in OCI-Ly1; ctrl#3, ctrl#6, and ctrl#11, in OCI-Ly8) transduced with the empty pSpCas9(BB)-2A-GFP backbone, were assayed. In DB, three single-cell clones with heterozygous *ARID1A* mutation (#B5, #C9, and #H2), and one *ARID1A* knock-out clone (#D1), were sequenced. In OCI-Ly1, two single-cell clones with heterozygous *ARID1A* mutation (#F9 and #F10), and three *ARID1A* knock-out clones (#E8, #G1, and #H3), were sequenced. In OCI-Ly8, three single-cell clones with heterozygous *ARID1A* mutation (#A9, #G5 and #G10), and one *ARID1A* knock-out clone (#G6), were sequenced. All clones were assayed in duplicates. RNA was isolated using Direct-zol™ RNA MicroPrep kit (Zymo Research), and each sample was normalized to 10 ng/μl. A total of 10 ng of RNA per sample were subjected to RNA sequencing using a version of the prime-seq protocol (Janjic, Wange et al. 2021).

The step-by-step protocol can be found on protocols.io (<https://www.protocols.io/view/prime-seq-s9veh66>). Prime-seq is a three-prime counting method that introduces a sample-specific barcode sequence and unique molecular identifiers (UMI) for accurate quantification of gene expression. Illumina paired-end sequencing was performed on an HiSeq 1500 instrument. The first read was 16 bases long to identify the sample barcode and UMI, and the second read was 50 bases long to identify the gene. Raw data were demultiplexed using deML (Renaud et. al.) and further processed using the zUMIs pipeline (2.5.4) (Parekh, Ziegenhain et al. 2018) with STAR (2.6) (Dobin, Davis et al. 2012). Reads were mapped to the human genome (hg38) with Ensemble gene annotations (GRCh38.84).

3.2.4.2 RNA-Seq data analysis

RNA-Seq data analysis was performed in collaboration with Maria Solovey and Maria Colomé-Tatché at the Institute of Computational Biology, Helmholtz Zentrum München, Germany.

In each cell line, low-expressed genes with a mean raw count less or equal to 5 were filtered out. Gene symbols were annotated using biomaRt (v2.44.4) library with *hsapiens_gene_ensembl* as dataset and <http://dec2017.archive.ensembl.org> as host. Counts were normalized using DESeq2 package (v1.28.1). Differentially expressed genes were computed individually in each cell line. The set comparison was control *versus* mutant clones. The mutant group comprised both heterozygous and homozygous knock-out clones. Only genes with log₂ fold change greater than 1 or lower than -1, and the p-adjusted value lower than 0.1 were considered significant.

3.2.5 Assay for Transposase-Accessible Chromatin (ATAC-Seq)

3.2.5.1 ATAC-Seq sample preparation

ATAC-Seq samples' preparation was performed in collaboration with Susanne Thieme.

For ATAC-Seq analysis, the same clones used for RNA-Seq experiment were assayed (see section above). Transposased fragments were prepared and pre-amplified as described in the optimized Omni-ATAC protocol (Corces, Trevino et al. 2017). Briefly, nuclei extracted from 2.5×10^5 cells were incubated with 2.5 μ L TDE enzyme at 37°C for 30 min during constant shaking. 20 μ l of pre-amplified transposased DNA were amplified using Nextera XT Index pair (i5 Index Name, Illumina), specific for every sample, and the KAPA HiFi PCR Kit (Roche Diagnostics), as described by the manufacturer. The DNA concentration of every reaction was assayed by Qbit (Qubit dsDNA HS Assay Kit, 500 assays, 0.2-100 ng, CatNr. Q32854, Invitrogen) before performing PCR amplification and after 10 cycles. Amplification was repeated until every reaction had 20-30 ng/ μ l DNA. 150 ng of amplified DNA were used for amplification with 10 μ M universal Nextera adapters (T_m 60°C). Each reaction was purified with a two-steps clean-up protocol with AMPure XP beads (Agencourt AMPure XP, CatNr. A63881, Beckman Coulter), washed twice with 70% ethanol, and eluted with 15 μ l UltraPure water (Invitrogen). Before proceeding with sequencing, sample quality was assayed by Nanodrop and BioAnalyzer. HiSeq 1500 instrument was used for Illumina paired-end sequencing. The first read was 58 (50+8) bases long and covered the sample barcode and UMI, and the second read was 50 bases long and was used to identify the gene.

3.2.5.2 ATAC-Seq data analysis

ATAC-Seq data analysis was performed in collaboration with Maria Solovey and Maria Colomé-Tatché at the Institute of Computational Biology, Helmholtz Zentrum München, Germany.

Reads were trimmed using TrimGalore (v0.6.5; default parameters) and aligned to the reference genome (hg38) with Bowtie2 (v2.3.5; --very-sensitive -X 2000). The alignments were sorted by position and indexed using samtools (v1.2). Three criteria were applied for filtering the mapped reads. From further analysis, reads mapping to the mitochondria genome were removed, as well as those with less than 6 bases coverage or reads with a MAPQ below 10. Besides, aligned fragments longer than 150bp were excluded using Deeptools-alignmentSieve (v3.3.1). Peak calling was done using MACS2-callpeak (v2.2.6; --nomodel --keep-dup 1 -g mm), and peaks overlapping with the blacklisted ones (<https://sites.google.com/site/anshulkundaje/projects/blacklists#TOC-Downloads>; <https://www.encodeproject.org/annotations/ENCSR636HFF/>) were filtered using bedtools-intersect (v2.29.2; -v) and then sorted (bedtools sort) and merged (bedtools merge) into non-overlapping peaks. A consensus peakset was generated in two steps, first finding a consensus peakset per condition, and then one for all using the last ones with bedtools sort and merge. The final counts of aligned reads in the global consensus peakset were done using featureCounts (subread package, v1.6.4). High-quality peaks were defined by having at least 50 counts in one or more samples. Low-quality peaks not matching this threshold were filtered out. Normalization of counts was performed using the DESeq2 package (v1.28.1). The annotatePeak function from the ChIPseeker package (v1.24.0) was used for peak annotation. The following parameters were applied to the function: tssRegion parameter set as -5000 to 5000, TxDb=TxDb.Hsapiens.UCSC.hg38.knownGene and annoDb="org.Hs.eg.db". Differentially accessible peaks were assayed individually in each cell line. The set comparison was controls versus mutants. The mutant group comprised both heterozygous and homozygous knock-out clones.

Differentially accessible peaks were defined by applying the DESeq function of the DESeq2 package (v1.28.1) to all peaks. Only peaks with log₂ fold change greater than 1 or lower than -1, and the p-adjusted value lower than 0.1 were considered significant.

3.2.6 Mass Spectrometry

LC-MS/MS sample preparation, data acquisition and analysis were performed in collaboration with Julia Mergner and Christina Ludwig at the Bavarian Center for Biomolecular Mass Spectrometry (BayBioMS), Freising, Bayern, Deutschland.

3.2.6.1 LC-MS/MS sample preparation

Cell surface proteins were isolated using Pierce Cell Surface Protein Isolation Kit (ThermoFisher Scientific, cat#89881).

In-gel trypsin digestion was performed according to standard procedures (Shevchenko, Tomas et al. 2006). Briefly, the samples were run on a NuPAGETM 4-12% Bis-Tris protein gel (ThermoFisher Scientific) for 5 min. Subsequently, the still not size-separated single protein band per sample was cut, reduced (50 mM dithiothreitol), alkylated (55 mM chloroacetamide) and digested overnight with trypsin. The generated peptides were dried in a vacuum concentrator and dissolved in 2% (v/v) acetonitrile, 0.1% (v/v) formic acid in HPLC grade water and spiked with PROCAL retention time standard peptide mix (Zolg, Wilhelm et al. 2017).

For total proteome analysis, 5×10^6 cells were pelleted at $500 \times g$ for 4 min and washed with 1 x PBS (PAN). Cells were lysed in 2% SDS and 50 mM Tris-HCl pH 7.5 and heated to 95°C for 5 min. 1 μ l 100 TFA was added to each sample to hydrolyze DNA, and the pH was subsequently adjusted to 8.5 with 3 M Tris solution. Prior to tryptic digestion, the detergent was removed from lysates by SP3 clean-up, following the protocol first described by Hughes et al. (Hughes, Moggridge et al. 2019). Briefly, lysate containing 20 μ g of protein was mixed with SP3 beads, and proteins were precipitated onto a 50:50 mixture of Sera-Mag Speed Bead types A and B (Thermo Fisher Scientific) in 70% acetonitrile. Beads were washed three times with 80% ethanol in water and once with acetonitrile. Disulfide bonds were reduced with 10 mM DTT for 45 min at 37 °C, followed by alkylation of cysteines with 55 mM CAA for 30 min at room temperature in 100 μ L of digestion buffer (2 mM CaCl₂ in 50 mM Tris-HCl, pH 8.5). Trypsin [1:50 (wt/wt) enzyme-to-protein ratio] was added, and bead-precipitated proteins were digested at 37 °C overnight. The next day, beads were settled using a magnet, and the supernatant was transferred to a new tube. Beads were washed by adding 50 μ L water, sonicated (3 \times 30 s), and the supernatants were combined. Samples were acidified with FA to pH < 3 and desalted on self-packed StageTips (three disks, \varnothing 1.5 mm C18 material, 3M EmporeTM, elution solvent 0.1% FA in 50% ACN). The generated peptides were dried in a vacuum concentrator and dissolved in 2% (v/v) acetonitrile, 0.1% (v/v) formic acid in HPLC grade water and spiked with PROCAL retention time standard peptide mix (Zolg, Wilhelm et al. 2017).

3.2.6.2 LC-MS/MS data acquisition

Liquid chromatography-coupled mass spectrometry (LC-MS/MS) analysis was performed on a Q Exactive HF-X Orbitrap (Thermo Fisher Scientific) coupled online to a Dionex Ultimate 3000 RSLCnano system. The liquid chromatography setup consisted of a 75 μ m \times 2 cm trap column and a 75 μ m \times 40 cm analytical column, packed in-house with Reprosil-Pur C18 ODS-3 5 μ m or Reprosil Gold C18 3 μ m resin (Dr. Maisch GmbH), respectively. Peptides were loaded onto the

trap column using 0.1% FA in water at a flow rate of 5 $\mu\text{L}/\text{min}$ and separated using a 50 min linear gradient from 4% to 32% of solvent B (0.1% (v/v) formic acid, 5% (v/v) DMSO in acetonitrile) at 300 nL/min flow rate. nanoLC solvent A was 0.1% (v/v) formic acid, 5% (v/v) DMSO in HPLC grade water. FAS protein abundance was monitored using a parallel reaction monitoring assay (PRM) and an inclusion list of tryptic FAS peptides and the PROCAL retention time calibration mixture. Full scan MS1 spectra were recorded in the Orbitrap (360 to 1300 m/z) with 60,000 resolution, an AGC target value of 3×10^6 and maxIT of 100 ms. Targeted MS2 spectra were acquired at 30,000 resolution, after HCD with 27% NCE, and using an AGC target value of 1×10^6 charges, a maxIT of 100 ms, an isolation window of 1.3 m/z and loop count of 23. The number of targeted precursors was adjusted to a cycle time of at maximum 3 s.

3.2.6.3 LC-MS/MS data analysis

The recorded RAW files were imported into Skyline (64-bit, v.20.2.0.343) for data filtering and analysis. The library ion match tolerance was set to 0.02 m/z, and the m/z extraction range to 300 m/z-1500 m/z. Transitions were extracted using the centroided product mass analyzer with 10 ppm mass accuracy. A spectral library for the selected peptides was constructed using the PRO-SIT prediction algorithm implemented in Skyline (64-bit, v.20.2.0.343) with standard settings (MacLean, Tomazela et al. 2010, Gessulat, Schmidt et al. 2019). FAS peptides with at least four consistently identified transitions in the WT samples were used for the quantification. Peaks were integrated using the automatic settings followed by manual curation of all peak boundaries. Peaks with a dotp product < 0.7 compared to the predicted peptide spectrum were excluded from the analysis. The summed area of fragment ion traces was exported for every transition, and the data was further analyzed in Microsoft Excel (version 2016). The allPeptides.txt file from a MaxQuant search of the PRM raw files was used to normalize the summed peptide intensities between all samples. Peptide and protein identification of a downstream cation was performed with MaxQuant (Cox and Mann 2008) using standard settings (version 1.6.3.3). Raw files were searched against the human reference proteome (UP000005640, 75,777 entries, download 23/01/2021) and common contaminants. Carbamidomethylated cysteine was set as fixed modification and oxidation of methionine, and N-terminal protein acetylation as variable modifications. Trypsin/P was specified as the proteolytic enzyme, with up to two missed cleavage sites allowed and the match between run function enabled. Results were filtered to 1% PSM, protein and Site FDR.

3.2.7 Functional Assays

3.2.7.1 Growth curve

FL-like cell lines were seeded at an initial density of 2×10^5 cells/mL, final volume of 10 mL. With 24 hrs interval time, 500 μL cell suspension was taken cell number was quantified by Vi-CELL™ XR. Every sample was counted twice. Cells were split before they reached the plateau phase, and cell count was normalized to the dilution factor.

3.2.7.2 Serum starvation

The desired amount of FL-like cells was harvested, washed and seeded at a density of 5×10^5 cells/mL. Cells were serum-starved in media supplemented with 0.4% FCS for 48 hrs. After serum starvation, the cells were released for 4 hrs in 10% FCS media and assayed.

3.2.7.3 Nocodazole treatment and anaphase cells assessment

FL-like cell lines were counted, and 3×10^4 cells were cultured overnight in a μ -Slide 8 Well ibiTreat, previously coated with poly-L lysine. Nocodazole was added to a final concentration of 150 ng/mL for 18 hrs. At the end of the synchronization process, cells were arrested in the G2/M phase. The cells were washed twice with warm PBS to remove the nocodazole and to allow them to progress through the cell cycle for 75 min until they entered anaphase. Next, the samples were fixed with 4% FA for 10 min, washed with PBS and stained with ActinGreen™ 488 Ready-Probes™ Reagent (ThermoFisher Scientific) for 10 min. After washing with PBS, the samples were mounted with Fluoromount-G™ Mounting Medium with DAPI (ThermoFisher Scientific).

3.2.7.4 FASLG-induced apoptosis assay

FASLG-induced apoptosis was assayed by treating the cells with a soluble, human FASLG trimeric protein named SUPERFASLIGAND™ (Enzo LifeScience). The day before treatment, 5×10^5 cells/mL were seeded in a 24-well plate. Every clone was plated in 4 wells to be independently treated with different concentrations. The next day, one vial of SUPERFASLIGAND™ (5 μ g) was resuspended in 50 μ L ultra-pure water. The stock solution was diluted with cell culture media to obtain the desired working concentrations of 3 ng/mL (0,6 μ L stock solution + 19,4 μ L media), 30 ng/mL (3 μ L stock solution + 17 μ L media), and 300 ng/mL. Cells were incubated for 24 hrs. Apoptosis was then assayed by FACS, and viable cells (PE::AnnexinV-DAPI-) were quantified. Every condition was normalized to the untreated control clone.

3.2.7.5 Density gradient centrifugation

For the isolation of mononuclear cells from peripheral blood (PBMCs), 27 mL of peripheral blood were typically withdrawn and used for isolation. The blood was diluted 1:1 with PBS, and 30 mL Ficoll-Paque at RT were slowly added to the diluted blood suspension. The samples were centrifuged at 400xg for 30 min in a swinging bucket rotor. Acceleration and deceleration of the centrifuge were performed at minimal speed. After centrifugation, several layers become visible due to the differential migration of the cell types. Mononuclear cells MNCs, including lymphocytes, monocytes and thrombocytes, sat at the interphase and were removed by careful aspiration with a pipette.

3.2.7.6 Lymphocytes isolation

Human lymphocytes were isolated from MNCs by magnetic-activated cell sorting (MACS). CD4+ or CD8+ T lymphocytes were enriched using StemCell negative selection Kits, EasySep™ Human CD4+ T Cell Isolation Kit or EasySep™ Human CD8+ T Cell Isolation Kit, according to manufacturer's instruction. Briefly, MNCs were thawed in RPMI media supplemented with 10% FBS and spun down at 200xg for 10 min. Cells were resuspended in MACS buffer and counted. First, MNCs were incubated with biotinylated antibodies against all cell types to be depleted. Second, anti-biotin-coupled magnetic MicroBeads were added to capture all antibody-bound cells. Antibody-bound cells were retained by a magnet, allowing unlabeled CD4+ or CD8+ T-lymphocytes to pass through.

Human CD19+ lymphocytes were isolated with EasySep™ Human CD19 Positive Selection Kit II. CD19+ cells were labeled with anti-CD19 antibody coupled with dextran-coated magnetic particles. Labeled cells were separated using an EasySep™ magnet. Unlabeled cells could be poured off, washed and used for further applications.

3.2.7.7 *In vitro and ex vivo* co-culture with T lymphocytes

When indicated, target cells (2.5×10^5) were stained with 1 μM CellTrace™ CFSE Cell Proliferation Dye, 4 min at RT, according to the manufacturer's instructions. Effector cells were stained with 10 μM CellTrace™ Violet Cell Proliferation Kit (VPD) for 10 min at 37°C and treated with or without CytoStim™, following the manufacturer's instructions. Target and effector cells (1:1) were seeded in 100 μL TexMACS in a 96-well-U-bottom plate and centrifuged at 200xg for 5 min. Co-cultured cells were incubated at 37°C for 15 min, up to several days and assayed by FACS or microscopy.

3.2.7.8 Luciferase reporter assay

Two regions of *FAS* promoter were cloned into pGL3-basic vector following the manufacturer's instruction (Promega). Briefly, two primer pairs flanking ETS1 TF binding motifs (Hollenhorst, Chandler et al. 2009) at the *FAS* promoter (chr10: 8899.... – 8899....) were designed using Primer3 tool (Table 11). XhoI and HindIII restriction sites were added to the primers. Digest resulted in a 332 bp and 537 bp insert that was ligated into the pGL3-basic vector. Successful cloning was validated by Sanger sequencing. *FAS*-pGL3 vectors (200 ng) were transfected together with the control luciferase reporter pRL-CMV-Renilla (40 ng, Promega) and increasing amounts of ETS1 expression plasmid (Addgene #82118) or RUNX3 expression vector (Addgene #162349) into 293T HEK cells. The tested concentrations of the expression plasmids were 50, 200 and 500 ng. After 24 h, cells were analyzed by Dual-Glo® Luciferase Assay (Promega). Luciferase reporter assay was performed by Johannes Hildebrand.

3.2.8 Nucleic acid methods

3.2.8.1 *E. Coli* transformation

One Shot™ TOP10 chemically competent *E. coli* strain (ThermoFisher Scientific) was transformed by heat shock. *E. coli*, 15 μL , were incubated with 30 ng of plasmid on ice for 30 min. Heat shock was performed at 42°C for 30 s, followed by 3 min incubation on ice. Next, 700 μL S.O.C. medium was added, and the mix was incubated at 37°C for 1 h while shaking (900 rpm). Samples were plated on Lysogeny broth (LB) agar plates with the suitable selection substance. Afterward, they were incubated at 37°C overnight.

3.2.8.2 Plasmid DNA Midiprep isolation

After successful transformation, two bacteria colonies grown overnight on the agar plate were picked. Each colony was inoculated in 20 mL LB medium supplemented with the suitable selection substance. The samples were incubated overnight at 37°C while shaking. The plasmid DNA was isolated according to the manufacturer's instructions using the PureYield™ Plasmid Midiprep System.

3.2.8.3 Isolation of genomic DNA (gDNA)

Genomic DNA (gDNA) was isolated from cell lines using QIAamp® DNA Blood Mini Kit according to the manufacturer's instructions.

3.2.8.4 Sanger sequencing

Sanger sequencing was performed using Lightrun sequencing service (GATC Biotech). DNA was sequenced with M13 primer (Table 11). Sequences were analyzed and aligned to a reference using SnapGene software (v6.0).

3.2.8.5 Isolation of total RNA

Total RNA was isolated using the Direct-zol™ RNA Kit, following the manufacturer's instructions. Briefly, 10^6 cells were synchronized via serum starvation, harvested and washed with PBS. The cell pellet was vortexed, and 500 μ L TRI-Reagent was added. The samples were vortexed again and frozen at -80°C overnight. The next day, DNase I treatment was performed, and the samples were diluted in 16 μ L DNase/RNase-Free Water.

3.2.8.6 Synthesis of complementary DNA (cDNA)

Complementary DNA (cDNA) was synthesized using the iScript cDNA Synthesis Kit. As starting material, 1 μ g of RNA template was used. The reaction was set up according to the manufacturer's instructions, using random hexamer primers. The total reaction volume was 10 μ L.

3.2.8.7 Quantitative real-time PCR analysis (TaqMan™ Assay)

The abundance of target genes, FAS and RUNX3, was quantified by TaqMan assay. The reactions were performed, as described in Table 14, using TaqMan™ Fast Advanced Master Mix, FAS (Hs00236330_m1 FAM-MGB FAS), RUNX3 (Hs01091094_m1 FAM-MGB RUNX3), and TBP (Hs00427620_m1 VIC-MGB TBP) as control. DNA amplification and fluorophore intensity detection were performed, as stated in Table 14. Data analysis was performed using the BIO-RAD CFX Maestro software (v 1.1). Target abundance was normalized per each sample to the housekeeping gene TBP and the native control.

Table 16. TaqMan reaction mix (left) and PCR program (right)

Reagent		Volume	Thermal cycling condition		
TaqMan Fast Advanced Master Mix 2x		5 μ L	Stage	Temp ($^{\circ}\text{C}$)	Time (mm:ss)
Primer mix 20x			Hold	50	2:00
Primer target gene		0.5 μ L	Hold	95	0:20
Primer housekeeping gene		0.5 μ L	Cycle	95	0:01
Nuclease-free water		2 μ L	(40 cycles)	60	0:20
cDNA (100 ng/ μ L)		2 μ L			

3.2.9 Flow-cytometry

Flow-cytometry methods are adapted from Strobl, C.D. Doctoral Dissertation (Strobl C. D., 2022, p. 35-37).

3.2.9.1 Surface protein staining

Cells were counted, and 2×10^5 cells were harvested in FACS tubes. After washing with PBS at 500x g for 4 min, cells were resuspended in 100 μ L PBS and incubated for 10 min at 4°C in the dark, with the optimized antibody dilution. Stained cells were washed with PBS and resuspended in 200 μ L 1x BD CellFIX™ or PBS. Lymphocytes were identified by the forward scatter (FSC A),

and the sideward scatter (SSC A). Single cells by FSC W, FSC H or FSC W and a fluorescent marker. Representative gating strategy in **Figure 6**.

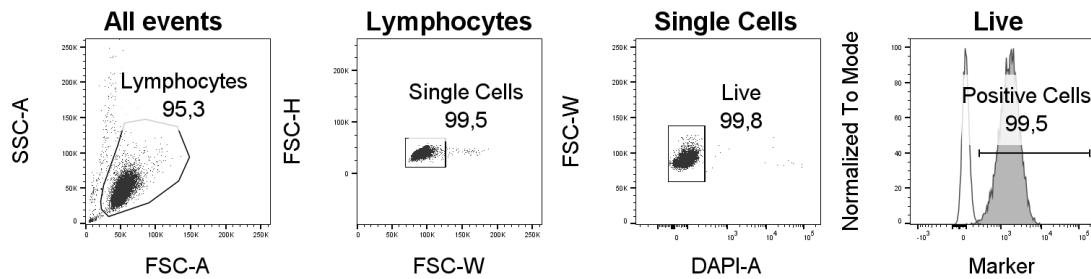


Figure 6. Representative gating strategy. Lymphocytes were identified by the forward scatter (FSC A), and the sideward scatter (SSC A). Single cells by FSC W and FSC H. Live population was determined by fluorescent DNA staining. The marker-positive gate was set compared to the isotype (negative) control.

3.2.9.2 Intracellular protein staining

Following surface marker staining, cells were washed with PBS. The BD Cytfix/Cytoperm™ Fixation/Permeabilization Kit was used for intracellular protein staining. Cells were incubated in the dark with 250 μ L BD Cytfix™ Fixation Buffer for 20 min at 4 °C. Meanwhile, 1x BD Perm/Wash buffer was prepared by diluting 1:10 the 10x BD Perm/Wash with sterile water. Fixed cells were washed twice with 1mL of BD Perm/Wash buffer and resuspended in 100 μ L of the same buffer. The desired antibody was added, and cells were incubated at 4°C for 30 min in the dark. Following intracellular marker staining, the samples were washed once with BD Perm/Wash buffer and once with PBS, to be resuspended in 200 μ L PBS and assayed by FACS.

3.2.9.3 Proliferation dye staining

Cells were counted, and desired cell number was harvested in FACS tubes. Cells were washed with PBS, and the pellet was resuspended in PBS-based staining solution (1 mL for up to 7×10^6 cells) and incubated at the required conditions (Table 16), with occasional vortexing. The cell suspension was topped with 10 mL PBS/FCS buffer to remove the dye in excess. Stained cells were washed with PBS and resuspended in the appropriate cell culture medium.

Table 17. Proliferation dyes staining conditions

Dye	Laser	Stock	Final concentration	Incubation	Temp (°C)
CFSE	488 nm	5 mM in PBS	2 μ M	4 min	RT
VPD	405 nm	1 mM in DMSO	1 μ M	10 min	37°C

3.2.9.4 Cell viability staining

AnnexinV staining was performed using the BD PE AnnexinV Apoptosis Detection Kit to assess viability by flow-cytometry. AnnexinV binds to phosphatidylserine, which apoptotic cells expose on the outer bilipidic layer of the plasma membrane. To distinguish between necrotic and apoptotic cells, DAPI staining was performed. DAPI penetrates through the cell membrane of necrotic cells since necrotic cells lose their integrity.

Before performing the experiment, the Annexin Binding buffer was diluted 1:10 with sterile water. Cells were harvested in FACS tubes and washed with PBS. Next, they were resuspended in 200

μL Annexin binding buffer containing 3.5 μL AnnexinV PE and incubated in the dark at RT for 10 min. Last, DAPI (1:100) was added, and cell death was assayed by FACS. From the forward and sideward scatter gate, all events were selected. Duplets were excluded from the analysis using FSC W and FSC H. AnnexinV was plotted versus DAPI. Live cells were identified as the double negative population (AnnexinV-DAPI-), early apoptotic cells were AnnexinV+DAPI-, while late apoptotic cells were double positive (AnnexinV+DAPI+).

3.2.9.5 Conjugation assay

Following co-culture (see above), the conjugation-forming potential of the target/effector cells was analyzed and quantified by FACS. Cells were harvested from the U-bottom plate, co-cultured and transferred to a FACS tube. The cells were washed with PBS and resuspended in 200 μL PBS. From the forward scatter (FSC A) and sideward scatter (SSC A) gate, the lymphocytes were selected, and the two populations of interest (target and effector cells) were plotted one versus the other (see the gating strategy in **Figure 7**). Typically, the effector cells were stained with VPD and detected with the BV421 laser. In contrast, the target cells were stained with CFSE dye and detected with the GFP laser, or were endogenously RFP, detected with the PE laser. The conjugation-forming potential is calculated as the percentage of double-positive cells (VPD+ CFSE+ or VPD+ PE+), normalized to the percentage of effector cells (VPD+).

$$\% \text{ conjugation - forming potential} = \left(\frac{\text{double positive cells}}{\text{effector cells}} \right) * 100$$

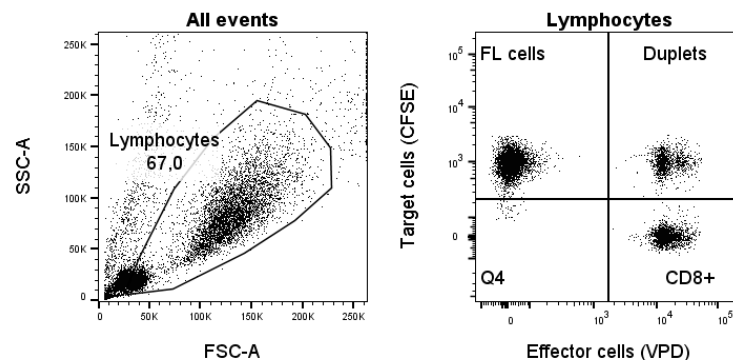


Figure 7. Representative gating strategy for conjugation assay. Lymphocytes were identified by the forward scatter (FSC A), and the sideward scatter (SSC A). Conjugation-forming potential is calculated as the percentage of double-positive cells.

3.2.9.6 Cytotoxic assay

After co-culturing the effector and target cells for 90 min to 3 hrs, the cells were harvested in FACS tubes. Here, cells were washed with PBS and stained with AnnexinV APC, according to the manufacturer's instructions. The lymphocytes were selected from the forward scatter (FSC A) and sideward scatter (SSC A) gate. Next, to distinguish between effector (VPD+) and target (CFSE+) cells, the gating of CFSE-positive cells was performed. The increase of Annexin V APC positive population in the target cells was used to calculate the percentage of specific Annexin V positive cells (**Figure 8**). Here, target cells cultured without effector cells were used as control samples per each condition.

% specific *annV* positive cells

$$= \frac{(\text{annV positive cells sample} - \text{annV positive cells control})}{(\text{total events sample} - \text{annV positive cells control})} * 100$$

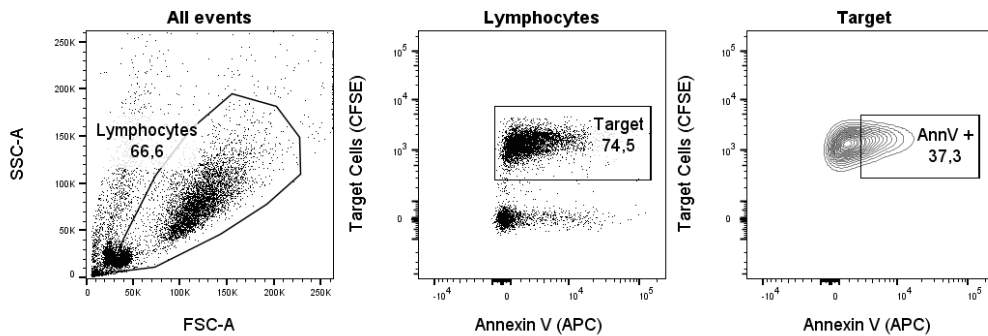


Figure 8. Representative gating strategy for cytotoxic assay. Lymphocytes were identified by the forward scatter (FSC A), and the sideward scatter (SSC A). Target cells were gated by the selection of CFSE-positive cells. The population of specific dying cells (AnnexinV+) was selected.

3.2.9.7 Real-time deformability assay (RT-DC)

Real-time deformability cytometry (RT-DC) was performed in collaboration with Fabian Müller and Richard Pelzl (Innere Medizin 5, Abt. für Hämatologie & Onkologie - Universitätsklinik Erlangen). The assay was performed according to the published protocol (Otto, Rosendahl et al. 2015).

3.2.10 Protein methods

3.2.10.1 Cell lysis and protein quantification

Cell number was quantified with Vi-CELL™ XR. Cells were harvested and washed with ice-cold PBS. The cell pellet was vortexed, and the desired lysis buffer was added. For western blotting, 10 µL radioimmunoassay (RIPA) buffer, supplemented with phosphatase and protease inhibitors, was used per 10⁶ cells. For more sensitive applications, like co-IP, Pierce™ IP Lysis buffer was used. Cells were incubated in the lysis buffer for 20 min on ice and spun down at 4°C with maximum speed for 30 min. The supernatant was then transferred to a fresh tube and stored at -80°C.

Protein quantification of cell lysates was quantified by bicinchoninic acid (BCA) assay, using the Pierce™ BCA Protein Assay Kit following to manufacturer's instructions. Briefly, 25 µL of cell lysates, diluted 1:10 with ultra-pure water, sample were assayed in a 96-well plate. As a reference, 25 µL of eight pre-diluted BSA samples were analyzed in the same plate of the test conditions. The working reagent (200 µL) was added to every sample, and the plate was incubated for 30 min at 37 °C in the dark. Protein concentration was quantified by measuring the absorption at 560 nm with a GloMax® Discover microplate reader.

3.2.10.2 SDS-PAGE

For protein analysis, sodium dodecyl sulfate (SDS)-polyacrylamide gel electrophoresis (PAGE) was performed using Mini-PROTEAN® Precast Gels and the Mini-PROTEAN Tetra Vertical Electrophoresis Cell. Briefly, 30 µg of protein was analyzed by western blotting. Protein samples were diluted to a final volume of 22 µL with Laemmli buffer (4x), DTT, and ultra-pure water. The samples

were then incubated for 7 min at 90 °C and loaded in a 12-well, 4-10% Mini-PROTEAN Tris-Tricine Precast Gels. The gel was placed in a gel chamber filled with homemade electrophoresis buffer. The run time was 3 hrs with increasing mA: 8 mA → 12 mA. As markers, 5 µL MagicMark™ XP Western Standard and 7 µL of SeeBlue® Plus 2 Prestained Standard were used.

3.2.10.3 Western blot analysis

The protein blotting was performed using the Mini Trans-Blot Module. The proteins were transferred to a polyvinylidene difluoride (PVDF) membrane (0.45 µm), previously activated in methanol. After activation, the PVDF membrane was incubated in transfer buffer, as well as the filter paper and the foam pads. The blotting sandwich was assembled with the PVDF membrane facing the anode and the gel facing the cathode and on both sides, one filter paper sheet and one foam pad. The transfer module core was filled with transfer buffer and placed on ice. The transfer time was 110 min at 36 V.

3.2.10.4 Chemiluminescent detection

After the transfer, the PVDF membrane was washed in deionized water for 10 min while shaking. Then it was blocked in 5% (m/V) milk powder in TBS-T for 2 hrs, followed by overnight incubation at 4°C while rolling the primary antibody at the appropriate concentration ([Table 8](#)). The membrane was washed with TBS-T three times for 10 min, and the secondary antibody was incubated for 1 hr at RT at a 1:5.000 concentration. Before analysis, the membrane was again washed with TBS-T for 10 min, and afterward, 1 mL of enhanced chemiluminescent (ECL) substrate was added. The signal was visualized using the Fusion SL4 imaging system.

3.2.10.5 Immunoprecipitation

For immunoprecipitation (IP) of ETS1, 3 mg of cell lysate was used. 8×10^7 cells were lysed using 4 mL of Pierce™ IP Lysis Buffer (ThermoFisher Scientific) supplemented with protease and phosphatase inhibitors, according to the manufacturer's instructions. Protein concentration was determined by Pierce BCA Assay (ThermoFisher Scientific). The same buffer was used as IP buffer. 100 µL SureBeads™ Protein A Magnetic Beads (BIO-RAD) were coupled with 10 µL anti-ETS1 antibody (rabbit clone D8O8A Cell Signaling; 1:10), for 3 hrs at 4°C with constant rotation. Lysates were incubated with the bead-bound antibody overnight at 4°C with continuous rotation. Bead-bound immunoprecipitates were washed three times with IP buffer and eluted twice with a total volume of 40 µL Laemmli Buffer 2x (BIO-RAD) and sample-reducing agent buffer (ThermoFisher Scientific). Input samples (30 µg) and co-IP samples were assayed for RUNX3 by immunoblotting.

3.2.10.6 Isolation of plasma membrane proteins

For the isolation of plasma membrane proteins, the Pierce™ Cell Surface Protein Isolation Kit was used, and the manufacturer's instructions were followed. Plasma membrane proteins were labeled with Thermo Scientific™ EZ-Link™ Sulfo-NHS-SS-Biotin, lysed with a mild reagent and isolated with Thermo Scientific™ NeutrAvidin™ Agarose. Briefly, 2×10^7 cells per clone were serum-starved, as described above. After release, the cells were washed with ice-cold PBS and incubated at 4°C for 30 min while shaking with 20 mL sulfo-NHS-SS-biotin solution. A quenching solution was added, cells were harvested and washed several times. Lysis was performed on ice, alternating vortexing with pulse-sonication every 5 min. The clarified supernatant was incubated with NeutrAvidin Agarose solution for 1 hr at RT, with end-over-end rotation. Labeled proteins

were isolated, washed and eluted in LDS buffer additioned with 1M DTT. The elution mix was placed in a heat block at 95°C for 5 min, and the samples were stored at -20°C.

3.2.11 Statistical analysis

At least three independent replicates were analyzed per every experiment. Data were shown as the mean value \pm SD. Ordinary one-way ANOVA followed by Sidak's multiple comparisons test using GraphPad Prism 6 software was performed when comparing more than two test conditions. Student t-test using GraphPad Prism 6 software was performed when comparing only two groups. As a control, the native single cell-derived clone belonging to the same cell line was used. In case of treatment with different compounds, as a control, the corresponding untreated clone was used. Statistical significance was defined as $P < 0.05$.

4. Results

4.1 *ARID1A* mutations in the GLSG2000 cohort

We re-analyzed available targeted DNA sequencing data from the GLSG2000 cohort (Pastore, Jurinovic et al. 2015). The customized target-capture bait set (targeted NGS) included full-length *ARID1A*. Here, we re-analyzed the data using a variant allele frequency (VAF) greater than 0.05 to define mutant cases. A total of 27 out of 151 fully evaluable cases harbored an *ARID1A* mutation, corresponding to a mutation frequency of 18%. *ARID1A* mutations did not cluster in a hotspot but were spread along the entire length of the gene (Figure 9). *ARID1A* mutations were classified into two groups, truncating mutations (including nonsense mutations, frameshift and splice site mutations) ($n = 24$) and missense mutations ($n = 3$), both predicted to lead to protein haplodeficiency. Notably, only one patient harbored multiple *ARID1A* mutations, one being subclonal and missense mutation, the other clonal and disruptive. Thus, we confirm that mutations are recurrent, predominantly heterozygous, disruptive and are predicted to result in protein haplodeficiency in FL.

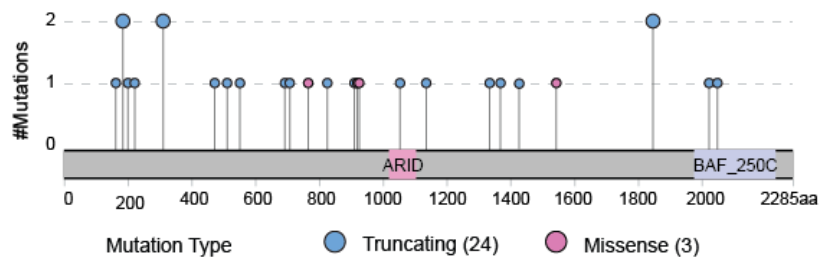


Figure 9. *ARID1A* mutations in the GLSG2000 cohort. Lollipop plot depicting 26 *ARID1A* mutations found in FL cases belonging to the GLSG2000 cohort. The frequency and distribution of the mutations along a schematic structure of the *ARID1A* protein are shown. The mutation type is color-coded.

Next, we checked whether *ARID1A* mutations co-occurred with other mutations in the SWI/SNF complex that were captured by our bait set. Overall, the SWI/SNF subunits had a mutation rate of 27.15% ($n = 41/151$). Three analyzed samples showed more than one mutated SWI/SNF complex subunit (Figure 10). Two of them had *ARID1A* and *SMARCA4* mutations, while the other had mutations in *ARID1A* and *ACTB* subunits. Moreover, our data showed that *ARID1A* is the most frequent mutated SWI/SNF component in FL (Figure 10). Thus, we conclude that in FL, the SWI/SNF complex is mainly affected by the mutation of single subunits and that *ARID1A* has the highest mutation rate.

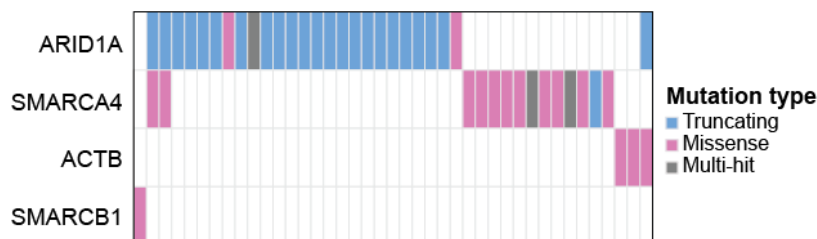


Figure 10. Oncoplot of SWI/SNF subunits mutated in the GLSG2000 cohort. Mutated subunits are sorted and ordered by decreasing frequency. The mutation type is color-coded.

4.2 Generation of FL-like model systems

4.2.1 FL-like cell lines

To investigate the biological role of *ARID1A* mutations in FL, we stably knocked-down *ARID1A* in three selected B-NHL cell lines. For this purpose we used OCI-Ly8, OCI-Ly1 and DB, which are characterized by the t(14;18)(q32;q21)[*BCL2/IGH*] translocation, and are *ARID1A* wild-type.

By CRISPR/Cas9 technology, we generated clones with heterozygous (het) and homozygous (KO) *ARID1A* mutations, as described in chapter 3.2.1. Furthermore, functional downregulation of *ARID1A* protein level was tested by immunoblot analysis (Figure 11). To assess the specificity of *ARID1A* phenotype, we stably re-expressed by lentiviral transduction *ARID1A* wild-type (WT) or empty vector (EV) on the *ARID1A* heterozygous clone (#A9) in OCI-Ly8.

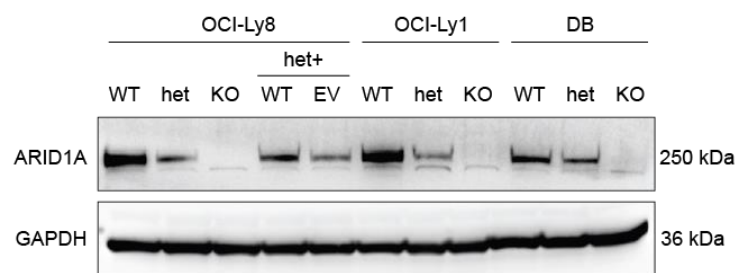


Figure 11. *ARID1A* levels in CRISPR/Cas9-engineered clones. Western blot of OCI-Ly8, OCI-Ly1 and DB cells with *ARID1A* wild-type (WT) or CRISPR-Cas9-engineered single-cell-derived clones with *ARID1A* heterozygous (het) or homozygous (KO) mutation. Re-expression of *ARID1A* WT on heterozygous background in OCI-Ly8. Representative blot.

4.2.2 B cell lymphoma-like (BCL) cells

Utilization of cell lines for studying the specific role of a mutation has limitations, including the broad mutation spectrum of the cell lines themselves and their adaptations to extensive *in vitro* culture. To partially circumvent these limitations, we implemented the innovative system published by the Hodson Laboratory (Caeser, Di Re et al. 2019, Caeser, Gao et al. 2021) and lentivirally knocked-down *ARID1A* by shRNA (listed in Table 12) in primary human B cell lymphoma-like (BCL) cells. We immortalized GC B cells by overexpressing *BCL2* and *BCL6*. However, they still require FDC-derived feeder cells support, providing them with the necessary TME signals (specifically CD40L and IL21). After transduction, expression of the shRNA construct was induced by doxycycline treatment. *ARID1A* knockdown was confirmed by immunoblot analysis (Figure 12). In total, GC B cells from three donors were tested.

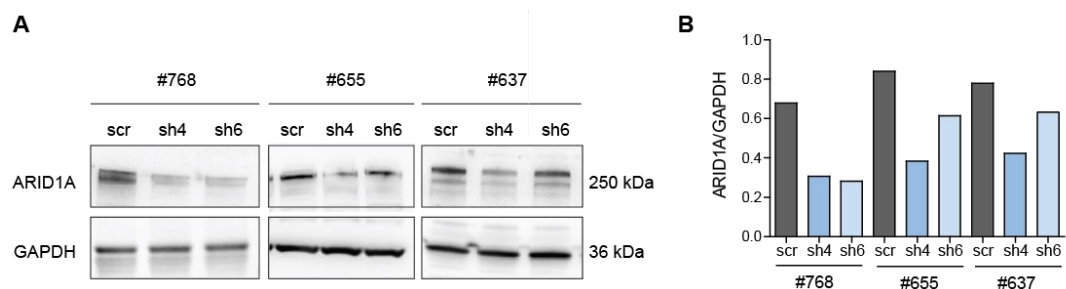


Figure 12. *ARID1A* knockdown in BCL cells. A) Western blot of BCL cells from donors #768, #655, and #637, transduced with shRNA scramble (negative control) or shRNA #4, #6 *ARID1A*. Representative blot. B) Quantification of *ARID1A* protein levels normalized to GAPDH.

4.3 Transcriptome analysis of CRISPR/Cas9-engineered cell lines with and without *ARID1A* mutation

To uncover the transcriptional changes deriving from *ARID1A* mutations in FL, we performed whole-transcriptome analysis as described above ([chapter 3.2.5](#)). OCI-Ly8, OCI-Ly1, and DB CRISPR-Cas9-engineered clones were analyzed. We assayed 22 single cell-derived clones with and without *ARID1A* mutation ([Table 15](#)), comprising biological replicates and technical duplicates.

4.3.1 Data analysis

Data processing and filtering were performed as described in chapter 3.2.5. Samples clustering was examined by principal component analysis (PCA). PCA showed that technical replicates did not affect the clustering of the samples. PCA indicated that samples clustered primarily by cell lines (**Figure 13 A**). Therefore, for further analysis, we processed the three cell lines individually. Due to the clustering of *ARID1A* het and KO samples (**Figure 13 B**), these were pooled and constituted the mutant (MUT) group. The following bioinformatics analysis compared mutant clones to *wild-type* ones (MUT versus WT).

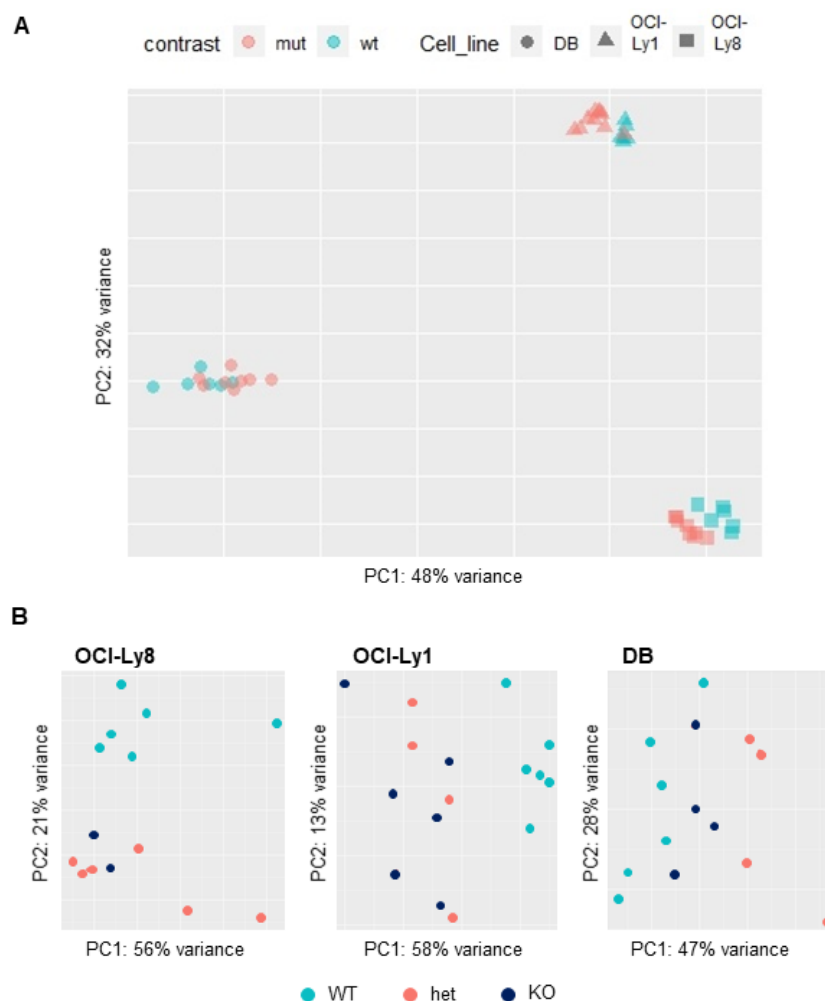


Figure 13. Principal component analysis (PCA) of *ARID1A* mutant and control samples from the RNA-Seq experiment. A) PCA of 44 samples. B) PCAs of samples grouped by cell line.

4.3.2 Differential expression of genes (DEGs)

In OCI-Ly8, OCI-Ly1 and DB, respectively, 469, 758, and 410 genes were significantly differentially expressed (DE) in the mutant groups compared to the *wild-type* (Figure 14).

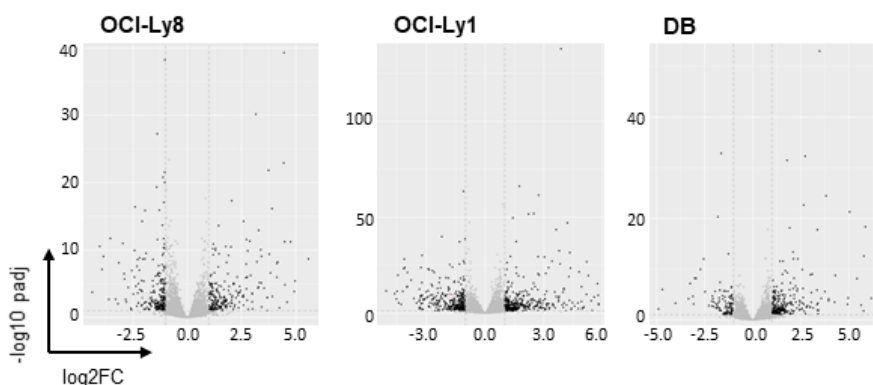


Figure 14. Volcano plot showing differentially expressed genes (DEGs). Set comparison MUT vs WT. Significant genes (black dots) have \log_2 fold change ± 1 , and the p-adjusted value < 0.1 .

4.3.3 Gene ontology (GO) analysis

We performed Gene Ontology (GO) analysis to interpret gene expression data. The study identified groups of genes that have similar biological functions or characteristics. Even though the PCA revealed the three cell lines to be very distinct, the GO analysis identified common GO terms in the presence of *ARID1A* mutation.

By performing exploratory analysis on the significantly down-regulated genes (MUT vs WT) with the GOrilla tool (<http://cbl-gorilla.cs.technion.ac.il/>), we identified GO terms associated with the regulation of cell cycle and cell death. Moreover, we found several immune response-related GOs, like T cell activation and differentiation, and cell-cell cross-talk via synapse formation to be enriched in the mutant groups. In Figure 15, the top 10 down-regulated GO terms in OCI-Ly1 (MUT vs WT) are shown, as an example. In the other analyzed cell lines, similar terms are identified among the top 25 down-regulated GO terms (data not shown). An exception is the DB cell line, where no “Cell death” GO terms are identified as down-regulated (MUT vs WT).

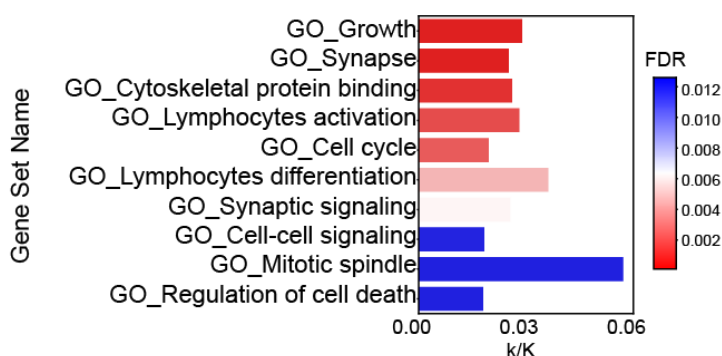


Figure 15. Top 10 down-regulated GO terms in OCI-Ly1 (MUT vs WT). Gene ratio (k/K) is defined as the number of DE genes (k) over the total number of genes comprised in a given GO (K).

In summary, we identified several immune response-associated GOs by analyzing the down-regulated genes in the MUT groups. “Cell death”, previously described to be associated with *ARID1A*

mutations (Luo, Cheung et al. 2008), “Growth” and “Cell cycle” terms were also identified, and they matched basic phenotyping experiments performed in the CRISPR/Cas9 engineered cell lines. Therefore, we then decided to study them functionally.

4.4 ARID1A loss affects cell growth and division in FL

Among the common enriched GO terms across *ARID1A* mutant clones, “Cell cycle” and “Growth” were identified (Figure 15). Therefore, we investigated the role of *ARID1A* mutations in regulating cell cycle progression by characterizing the CRISPR/Cas9-engineered clones phenotypically.

4.4.1 Growth phenotype deriving from *ARID1A* mutations

We first performed growth curve experiments to test whether defects in cell cycle progression were observed *in vitro* cell culture. Over seven days, *ARID1A* heterozygous (het) and homozygous (KO) mutant clones showed a significantly slower growth rate compared to the corresponding WT control ($n = 3$, het vs WT and KO vs WT $p < 0.0001$ at day 7). This result was consistent across the three FL-like cell lines (Figure 16).

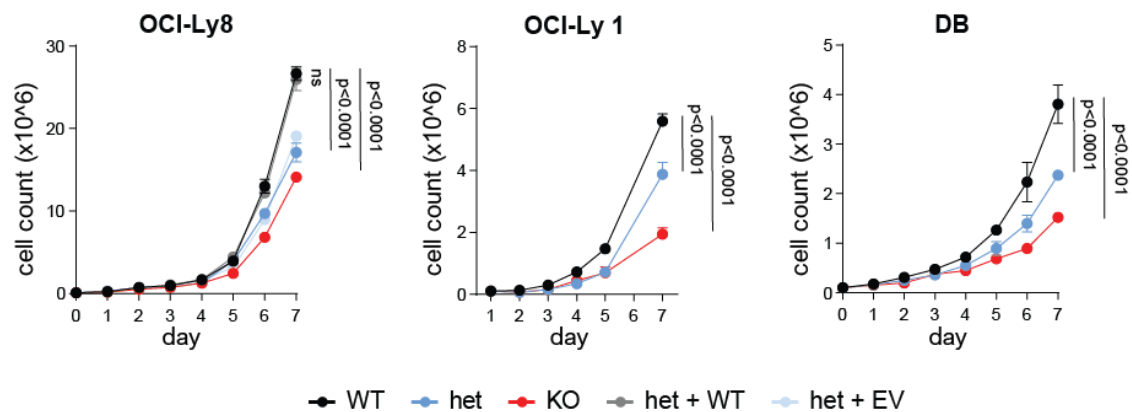


Figure 16. Growth curve of *ARID1A* mutant and WT CRISPR/Cas9-engineered clones. The total cell count (y-axis) was plotted over time (x-axis). Every sample was assayed twice. The experiment was performed in biological replicates ($n = 3$ / cell line). Mean count of technical and biological replicates \pm SD; p values are calculated on day 7 with regular two-way ANOVA analysis, Sidak’s multiple comparison test.

Here, we showed that *ARID1A* loss is consistently associated with slower cell growth.

4.4.2 GSEA suggests that *ARID1A* loss is associated with cell cycle progression and impaired mitosis

We further examined RNA-Seq data to identify possible factors determining the *ARID1A* mutant-derived growth phenotype. Using the Reactome Pathway Database, gene set enrichment analysis (GSEA) was performed on significantly down-regulated genes (MUT vs WT). The mutant groups were enriched for mitosis-associated pathway (Figure 17). More specifically, G2/M checkpoints and mitotic anaphase terms comprised genes significantly downregulated. Separation of sister chromatids was also among the top 10 terms in OCI-Ly8 and DB cell lines.

In conclusion, Reactome GSEA showed consistent results among the three cell lines and suggested that *ARID1A* loss impairs mitosis.

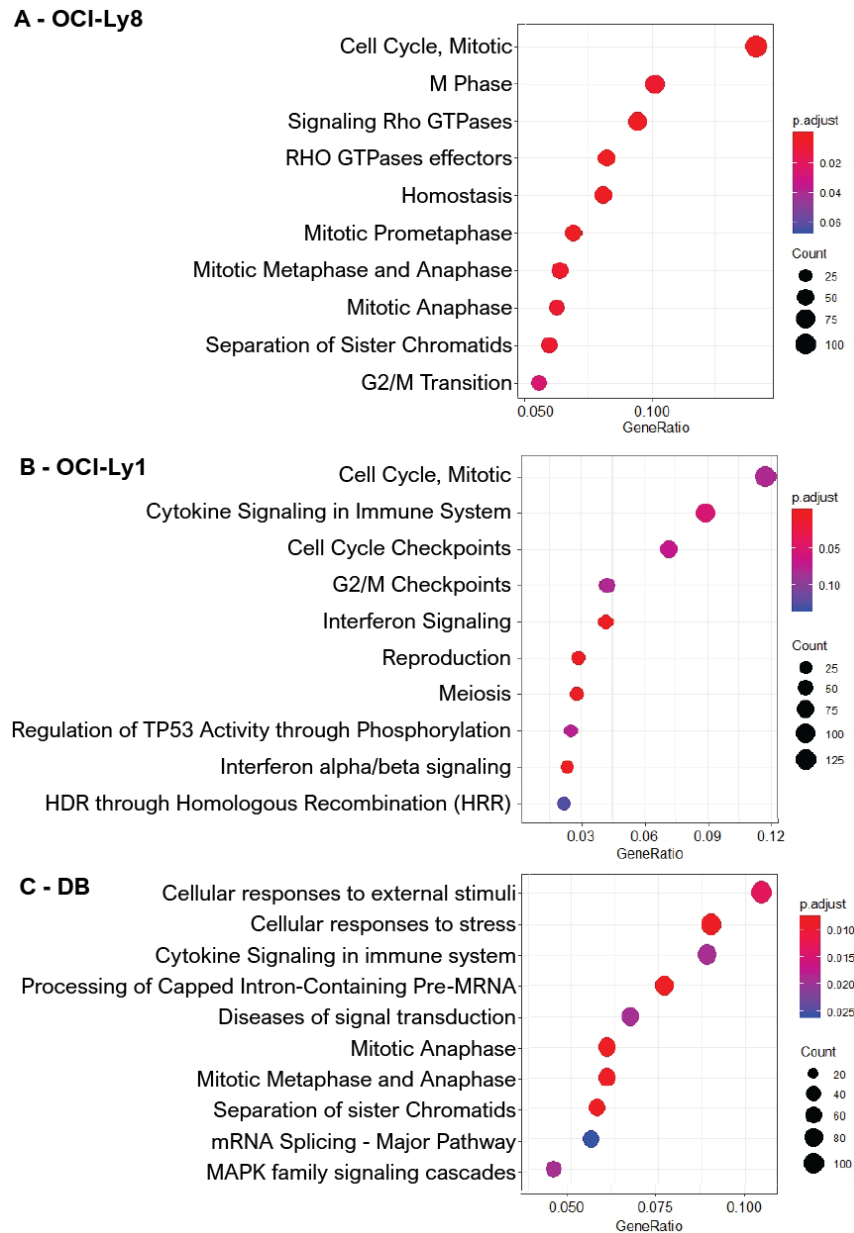


Figure 17. Gene set enrichment analysis using the Reactome Pathway Database. A-C) Analysis performed on downregulated genes (MUT vs control). The dot size represents the DEGs count belonging to each pathway. The dot color explains the significance of the pathway.

4.4.3 Slower cell cycle progression in *ARID1A* mutant clones correlates with anaphase chromatin bridge formation

We treated cells with nocodazole to test the effects on the cell cycle progression of *ARID1A* mutations *in vitro* cell culture. This antineoplastic agent, which impairs microtubule polymerization, was used to synchronize the cells in G2/M phase. After its removal, the cells progressed through the cell cycle and entered mitosis. To follow the cell cycle progression, we stained our clones with ActinGreen™ 488 ReadyProbes™ Reagent and DAPI. A high number of anaphase cells was observed between 60 min and 75 min after nocodazole removal. At this time point, cells were fixed with formalin, and 200 single cells in anaphase (50 cells/experiment, n = 4) were analyzed by microscopy (**Figure 18 A**). Here, we observed the extensive formation of chromatin bridges, strings of chromatin connecting the two daughter cells during mitosis (**Figure 18 B**). The number

of anaphase bridges was significantly higher in *ARID1A* mutant clones than in WT or het+*ARID1A*.

In conclusion, our experimental data showed that *ARID1A* loss correlates with increased anaphase bridges formation and slower cell growth.

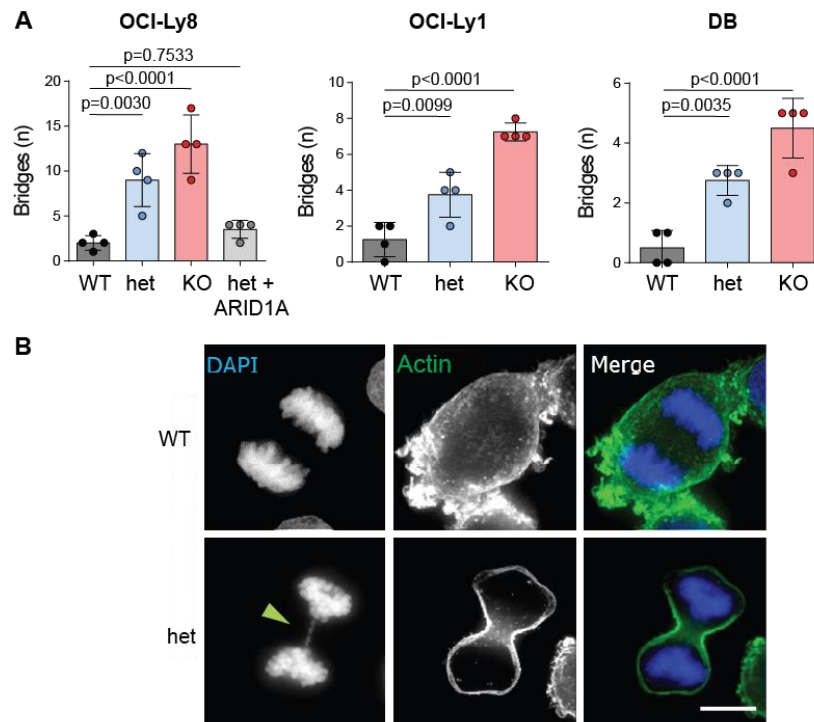


Figure 18. Anaphase chromatin bridges formation. A) Chromatin bridges analysis. Mean counts \pm SD. p values are calculated with regular one-way ANOVA analysis, Sidak's multiple comparison test. **B)** Representative image of anaphase chromatin bridges formation by fluorescence microscopy. DAPI is depicted in blue, and actin filaments in green. The scale bar is 20 μ m.

4.4.4 Summary

Here, we showed that *ARID1A* mutant clones were characterized by a slower growth rate compared to the control. RNA-Seq data identified *ARID1A* mutations to significantly influence mitosis. *In vitro* experiments showed that *ARID1A* loss correlates with increased anaphase bridge formation. Overall, we could not identify the molecular mechanism behind the increase in anaphase bridges formation. We hypothesized that reduced growth is not the primary effect of *ARID1A* loss but the consequence of defective sister chromatid separation and genomic instability. We decided not to follow up on the reduced growth phenotype since it does not explain the selective advantage of *ARID1A* mutations during lymphomagenesis.

4.5 *ARID1A* mutation impacts FASLG-induced apoptosis

A previous study (Luo, Cheung et al. 2008) linked *ARID1A* loss to FASLG-induced apoptosis resistance in several cancer cell lines. Interestingly, our RNA-Seq data ([chapter 4.3.3](#)) highlighted apoptosis among the downregulated GO terms in *ARID1A* mutant clones in both OCI-Ly8 and OCI-Ly1. Therefore, I focused on unraveling the link between *ARID1A* mutations and FASLG-induced apoptosis in FL.

4.5.1 *ARID1A* mutation status and FAS levels in primary FL samples

First, we investigated whether there may be a correlation between *ARID1A* mutation status and FAS levels in primary FL. Here, we analyzed primary FL biopsies belonging to the GLSG2000 cohort (Pastore, Jurinovic et al. 2015) with known *ARID1A* mutation status. Gene expression profiling (GEP), from FL samples with *ARID1A* mutation ($n = 12$) and *ARID1A* WT ($n = 39$) (GSE 147125, Tobin, Keane et al. 2019) showed downregulation of *FAS* expression levels (**Figure 19 A**, $p = 0.0872$), but it did not reach statistical significance. GEP analyzes bulk gene expression in the samples and *FAS* is known to be expressed by non-FL cell subsets (e.g. T cells and macrophages) in the TME. Therefore, we performed quantitative multispectral imaging (QMI) analysis, which allows spatial resolution, and compared cases with *ARID1A* mutation ($n = 7$) to *ARID1A* WT ($n = 35$). The data showed that FAS protein levels were significantly reduced (**Figure 19 B-C**, $p < 0.0001$), in samples with *ARID1A* mutation. Overall, the data linked *ARID1A* loss to reduced FAS expression in primary FL.

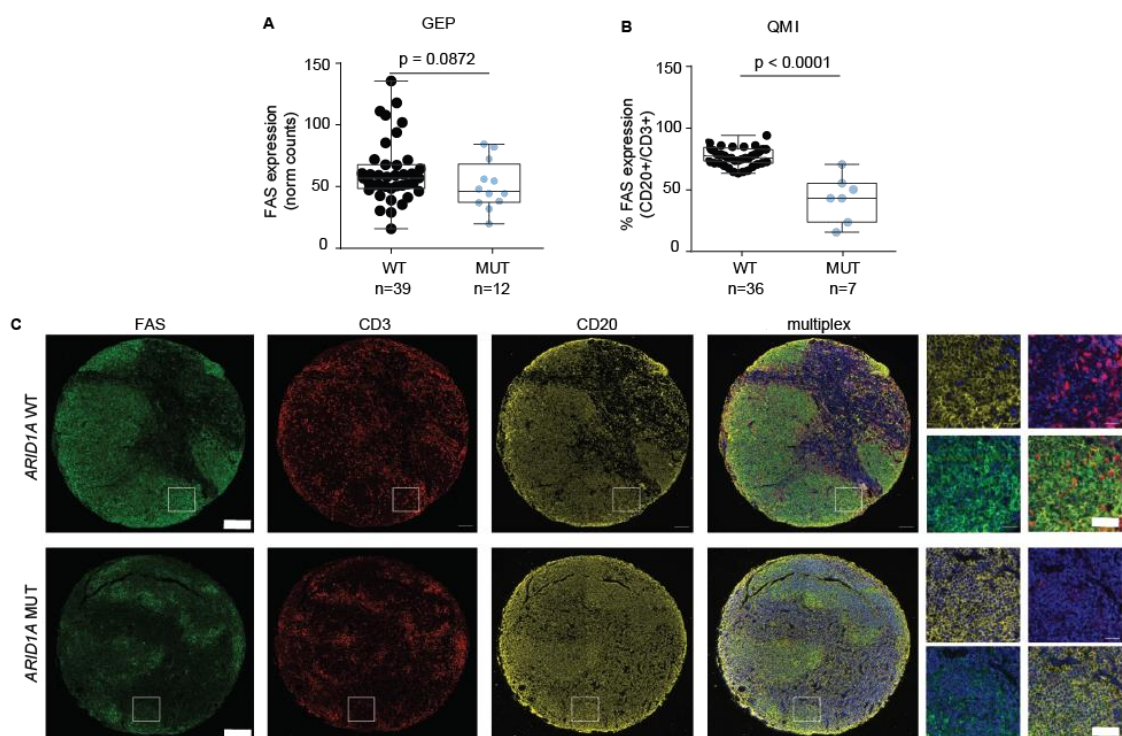


Figure 19. FAS quantification in primary FL biopsies. A) FAS RNA expression in the *ARID1A* wild-type vs *ARID1A* mutant FL cases. **B)** FAS protein abundance in the CD20+ cells normalized to CD3+ cells of *ARID1A* wild-type vs *ARID1A* mutant cases. **C)** Multispectral imaging of 2 representative FL biopsies; scale bars are 400 μm (low magnification) or 50 μm (high magnification). P values are from one-tailed unpaired Student's t-test (Mann-Whitney).

4.5.2 FAS levels upon *ARID1A* mutations in FL-like cell lines

We observed lower FAS levels in primary FL samples with *ARID1A* mutations. Next, we investigated the association between *ARID1A* mutation status and reduced FAS levels in FL-like cell lines. To quantify FAS surface levels, I assayed OCI-Ly8 and OCI-Ly1 (*ARID1A* WT), WSU, and Karpas422 (*ARID1A* MUT) cell lines by flow-cytometry. We detected reduced FAS surface protein in *ARID1A* mutant cell lines (**Figure 20**).

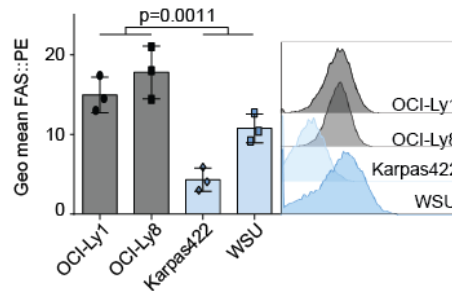


Figure 20. FAS quantification in native FL-like cell lines. FAS cell-surface levels of *ARID1A* WT (OCI-Ly1 and OCI-Ly8) vs *ARID1A* MUT (Karpas422 and WSU) cell lines. The left panel displays geometric means of independent biological replicates ($n = 3$). The right panel shows the FACS signal intensity distribution for one representative experiment.

Similarly, I assayed the CRISPR/Cas9 single cell-derived clones from OCI-Ly8 and OCI-Ly1. DB clones were excluded because by whole-transcriptome analysis, we observed that *FAS* expression was already very low in *ARID1A* WT clones. Besides, the GO_Cell Death, nor any daughter term (see 4.3.3), was not identified as down regulated upon *ARID1A* loss – this point is further discussed (see 5.1.3.2). CRISPR/Cas9 clones with *ARID1A* het and KO mutations (**Figure 11**) showed reduced FAS levels in both cell lines (**Figure 21 A-B**, $n = 3$, OCI-Ly8 het $p = 0.0006$, KO $p = 0.0003$; OCI-Ly1 $p = 0.0003$). Re-expression of *ARID1A* WT (het+*ARID1A*) rescued the phenotype (**Figure 21 A**).

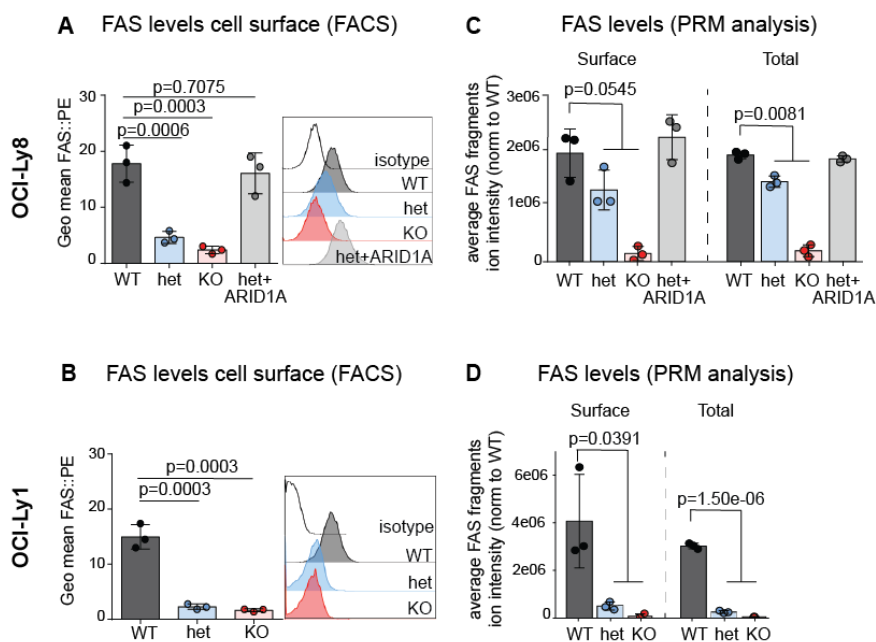


Figure 21. FAS protein levels in CRISPR/Cas9 clones with and without *ARID1A* mutation. A-B) FAS cell-surface levels of OCI-Ly8 (**A**) and OCI-Ly1 (**B**) clones *ARID1A* WT, het, KO and het+*ARID1A*. The left

panel displays geometric means of independent biological replicates ($n = 3$). The right panel shows the FACS signal intensity distribution for one representative experiment. **C-D**) FAS protein levels measured by LC-MS/MS parallel reaction monitoring assay (PRM) in the surface proteome or total proteome lysates of OCI-Ly8 (**C**) and OCI-Ly1 (**D**) *ARID1A* WT, mutant and het+*ARID1A* ($n = 3$). Pooled data from biological replicates (n) are represented as mean \pm SD; p values are from ANOVA analysis or one-sided T-test.

In addition, we performed parallel reaction monitoring assay (PRM) with liquid chromatography-coupled mass spectrometry (LC-MS/MS). PRM analysis allows the detection of peptides belonging to FAS protein, increasing the detection power of standard LC-MS/MS. I isolated plasma membrane proteins and total proteins to quantify FAS levels. Again, *ARID1A* mutant clones showed significant downregulation of surface FAS (**Figure 21 C-D**, $n = 3$, MUT vs WT OCI-Ly8 $p = 0.0545$, and OCI-Ly1 $p = 0.0391$) in both cell lines and of total FAS levels ($n = 3$, MUT vs WT OCI-Ly8 $p = 0.0081$, and OCI-Ly1 $p = 1.50e-06$). We showed that *ARID1A* loss results in reduced FAS protein levels on the cell surface and intracellular.

4.5.3 FASLG-induced apoptosis phenotype in *ARID1A* mutant FL-like cell lines

To test if reduced FAS surface levels had functional consequences, we performed *in vitro* FASLG-induced apoptosis assay using a human, soluble, recombinant FASLG oligomer (**Figure 22 A**). OCI-Ly8, OCI-Ly1, WSU, and Karpas422 cell lines were treated with increasing dose of soluble FASLG for 24 hrs. Here, we observed that the cell lines harboring *ARID1A* mutations (Karpas422 and WSU) were significantly less sensitive to FASLG-induced apoptosis compared to cell lines with *ARID1A* WT (OCI-Ly8 and OCI-Ly1) (**Figure 22 B**).

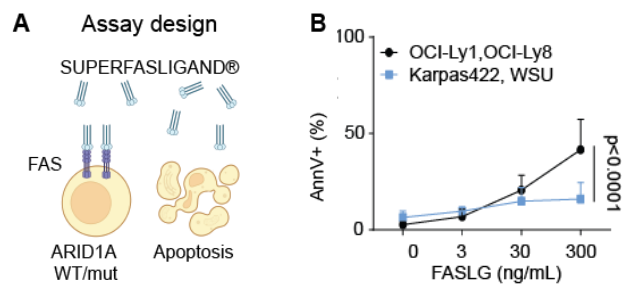


Figure 22. FASLG-induced apoptosis assay. **A**) Schematic representation of the FASLG-induced apoptosis assay. **B**) Percent of dying (AnnexinV+DAPI- and AnnexinV+DAPI+) cells upon treatment with soluble FASLG ($n = 3$). Pooled data from biological replicates (n) are represented as mean \pm SEM; p values are from ANOVA analysis.

We treated OCI-Ly8, and OCI-Ly1 CRISPR-Cas9 engineered clones with and without *ARID1A* mutations, using an increased dose of soluble FASLG for 24 hrs. Consistent with the previous assay, we observed resistance to FASLG-induced apoptosis in *ARID1A* het and KO clones in both cell lines (**Figure 23 A-B**, $n = 3$, OCI-Ly8 het $p = 0.0026$ and KO $p < 0.0001$; OCI-Ly1, het and KO $p < 0.0001$). Moreover, we showed that overexpression of *ARID1A* (het+*ARID1A*) was functional and could rescue apoptosis sensitivity (**Figure 23 A**). In conclusion, we demonstrated that *ARID1A* loss leads to FASLG-induced apoptosis resistance in FL.

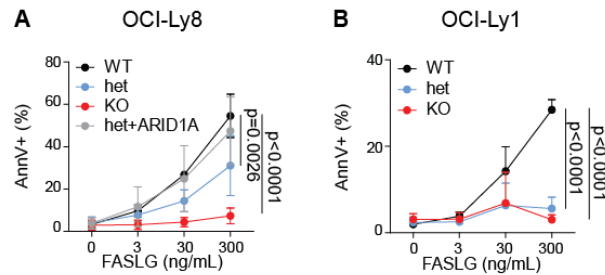


Figure 23. FASLG-induced apoptosis assay. Percent of dying (AnnexinV+DAPI- and AnnexinV+DAPI+) cells upon treatment with soluble FASLG (n = 3), OCI-Ly8 (**A**), and OCI-Ly1 (**B**). Pooled data from biological replicates (n) are represented as mean \pm SEM; p values are from ANOVA analysis.

4.5.4 CD8+ T lymphocytes-mediated killing upon ARID1A loss

CD8+ T lymphocytes, critical players in immune surveillance, are known to induce the killing of cancer cells by FAS / FASLG pathway activation. To test the impact of ARID1A loss on FAS / FASLG-mediated apoptosis experimentally, we established an *ex vivo* co-culture system (**Figure 24 A**). We cultured OCI-Ly8 clones, either *ARID1A* WT or MUT (CFSE+), together with CD8+ T lymphocytes from healthy donors (VPD+). After co-culturing the cells for 3 hrs in the presence of CytoStim™ to force the cell interaction, we measured apoptosis as the percentage of CFSE+ AnnexinV+ cells. The data showed that the CFSE+ AnnexinV+ population in *ARID1A* het and KO clones was significantly reduced compared to WT (**Figure 24 B**, n = 5, p = 0.0115, and p = 0.0055, respectively). Crucial in determining CD8+ T cells killing ability is the cell-cell cross-talk via BCR-TCR interaction. Next, we estimated the percentage of B-T conjugates formed (CFSE+VPD+) and MHC1 levels. Relevant differences between clones were not observed (**Figure 24 C-D**). Here, we showed that the killing potential of CD8+ T cells is impaired in *ARID1A* mutant clones.

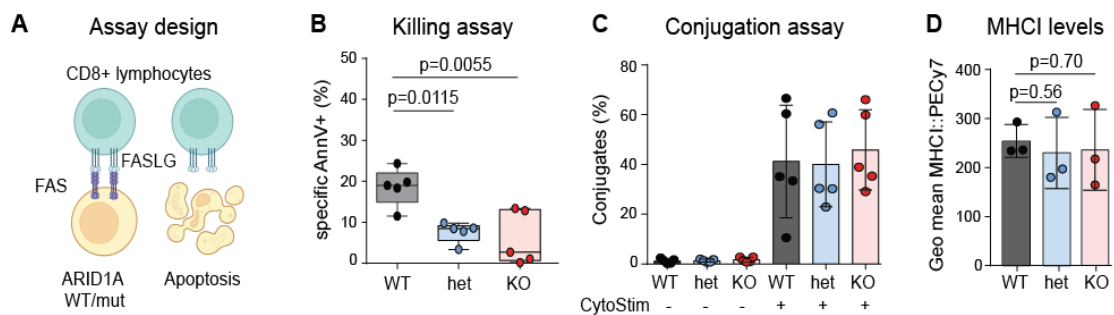


Figure 24. T-cell mediated killing assay. **A**) Scheme of the T cell-mediated killing assay. **B**) Percent of specific AnnexinV+ OCI-Ly8 cells ($[\text{AnnV+cells}_{\text{sample}} - \text{AnnV+cells}_{\text{control}}] / [\text{total events}_{\text{sample}} - \text{AnnV+cells}_{\text{control}}] * 100$) upon co-culture with the CD8+ T cells (n = 5, biological replicates). **C**) Percent of conjugates formation of OCI-Ly8 cells upon 3 hrs co-culture with CD8+ T-cells. **D**) MHC1 surface levels. Pooled data from biological replicates (n) are represented as mean \pm SD; p values are from ANOVA analysis.

4.5.5 ARID1A loss correlates with reduced FAS expression

Given the functional impact of the described phenotype, we aimed to understand at which level ARID1A controls FAS and if the decrease in, protein is a consequence of *FAS* transcription reduction. We tested whether *ARID1A* mutations affect *FAS* gene expression. RNA-Seq data revealed decreased *FAS* levels in *ARID1A* mutant clones compared to controls (**Figure 25 A-B**, n = 14, OCI-

Ly8 $p < 0.0001$, and OCI-Ly1 $p < 0.0001$). I validated this result by quantitative real-time PCR (RT-qPCR) (Figure 25 C). Here, we showed that ARID1A loss correlates with reduced *FAS* gene expression.

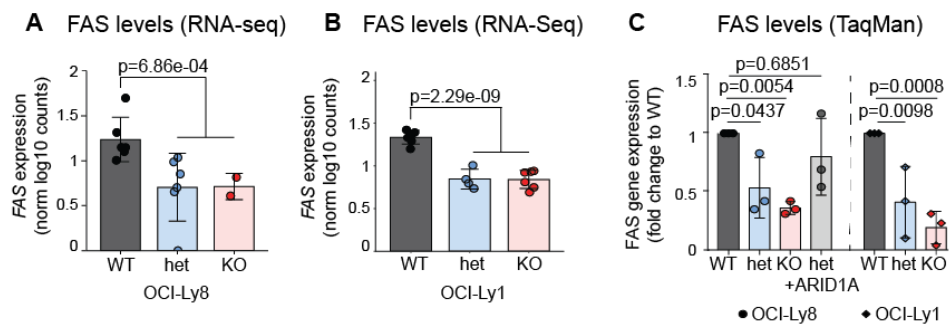


Figure 25. *FAS* gene expression levels upon ARID1A loss. A-B) *FAS* gene expression measured by RNA-Seq in OCI-Ly8 (A, $n = 14$) and OCI-Ly1 (B, $n = 16$) single-cell-derived clones. C) *FAS* RNA expression validated by RT-qPCR (TaqMan assay) in OCI-Ly8 and OCI-Ly1 ($n = 3$). Pooled data from biological replicates (n) are represented as mean \pm SD; p values are from ANOVA analysis or one-sided T-test.

4.5.6 Assay for Transposase-Accessible Chromatin using sequencing (ATAC-Seq) shows that chromatin openness at *FAS* TSS is not affected by ARID1A loss

To unravel the described *FAS* phenotype, we studied the chromatin changes induced by *ARID1A* mutation using Assay for Transposase-Accessible Chromatin using sequencing (ATAC-Seq).

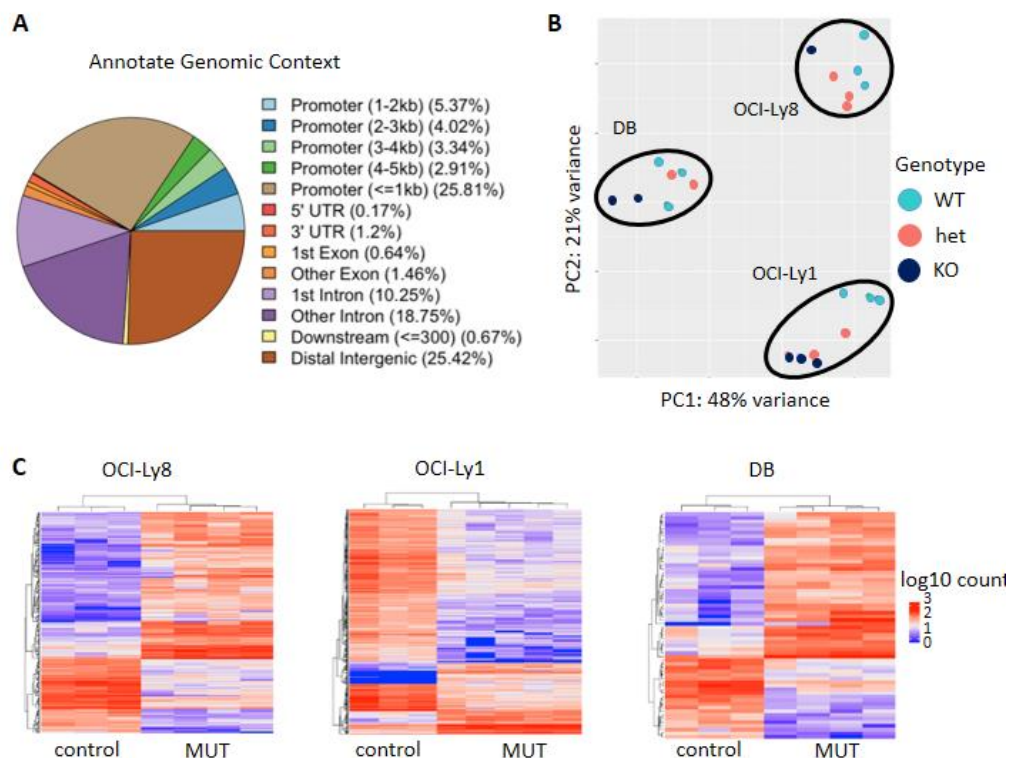


Figure 26. Overview ATAC-Seq analysis. A) Average annotated genomic context. B) PCA of 22 CRISPR/Cas9 single cell-derived clones with and without *ARID1A* mutation. Samples clustered by cell line (OCI-Ly8, OCI-Ly1, and DB). C) Heatmap of differentially accessible peaks in *ARID1A* MUT vs control clones per cell line.

Data processing was performed as described in chapter 3.2.6. Among all detected peaks, circa 40% were annotated at the promoter regions (**Figure 26 A**), matching the published quality matrix (Thurman, Rynes et al. 2012). Similar to RNA-Seq data, PCA showed that the three cell lines clustered separately. Again, het and KO *ARID1A* clones were pooled in the MUT group for further analysis (**Figure 26 B**). After filtering, 119,461 peaks were mapped to the reference genome.

In OCI-Ly8, OCI-Ly1 and DB, respectively, 292, 786, and 70 peaks were significantly differentially open (DO) in the mutant groups compared to the wild-type (**Figure 26 C**).

4.5.7 FAS promoter accessibility upon ARID1A loss

Given the chromatin remodeling function of ARID1A, we first hypothesized that it directly controls the accessibility of the *FAS* transcription starting site (TSS). We detected four open chromatin regions (peak) at the *FAS* promoter for OCI-Ly8 and OCI-Ly1. Nevertheless, we found no significant differences in accessibility upon ARID1A loss (**Figure 27**).

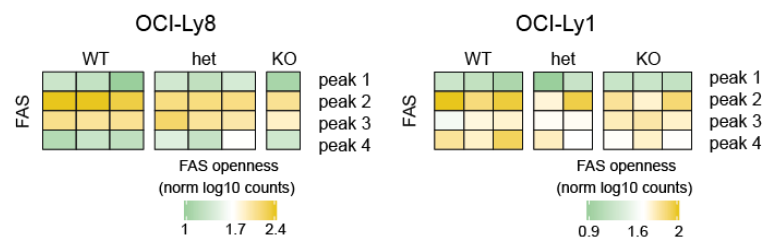


Figure 27. FAS promoter accessibility. Four peaks were mapped to the *FAS* promoter region. None of them is differentially accessible upon ARID1A loss.

4.5.8 Expression of FAS-regulating transcription factors upon ARID1A loss

We next hypothesized an indirect effect of *ARID1A* mutations on *FAS* transcription. Gene expression is regulated at several levels, and expression of transcription factors (TFs) is critical. Therefore, we identified a set of FAS-regulating TFs (FAS-reg-TFs) using the DoRoThEA database. By RNA-Seq, we checked which FAS-reg-TFs were differentially expressed and common to both cell lines. Our analysis did not show any mutual differentially expressed FAS-reg-TFs, leading to the conclusion that the direct FAS-reg-TF were unaffected by the *ARID1A* mutation (**Figure 28**).

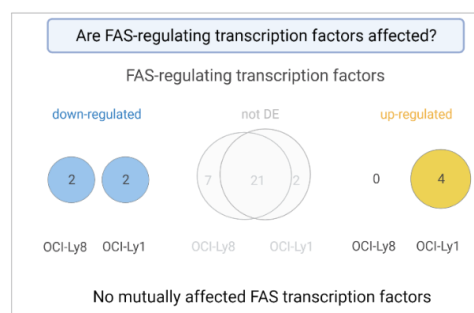


Figure 28. FAS-regulating TFs are not DE. None of the identified FAS-reg-TFs is DE and common to OCI-Ly8 and OCI-Ly1.

4.5.9 Identification of the FAS-regulating ARID1A-dependent transcriptional network

Another layer of transcription regulation consists of the co-transcription factors (co-TFs). To test if ARID1A loss influences their expression, we defined a network of FAS-reg co-TFs. First, we selected the FAS-reg-TFs, which were not differentially expressed in our data and were common to both cell lines. Here, we excluded the DE FAS-reg-TFs, since we have already tested their dependency on *ARID1A* mutations (**Figure 28**). The published FAS-reg-TFs constitute the group of potential co-TFs since they are reported to control FAS regulation. Next, using the DoRotheA database, we selected all genes classified as TFs in our data that were differentially expressed in both cell lines upon ARID1A loss. Last, we built a network of potential FAS-reg co-TFs, by testing with the STRING database if any of the published FAS-reg-TFs and the other DE potential FAS-reg co-TFs were known or predicted to interact. Here, we identified a gene network containing ETS1 as a direct FAS-reg-TF (Hollenhorst, Shah et al. 2007, Hollenhorst, Chandler et al. 2009) and RUNX3 as differentially expressed potential co-TF (**Figure 29**) (Kasahara, Shiina et al. 2017).

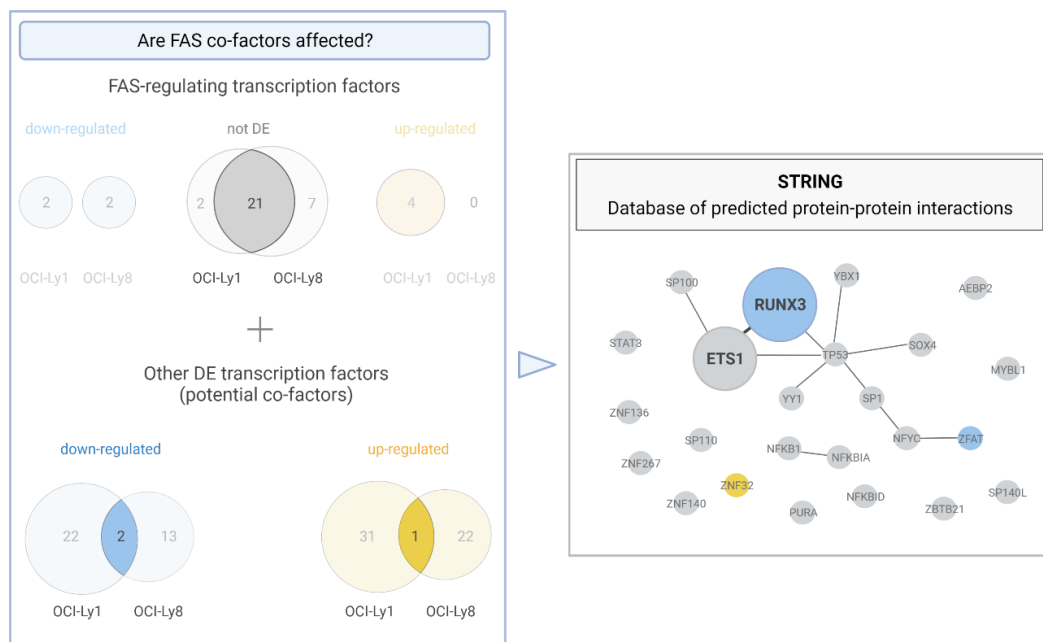


Figure 29. FAS-regulating co-TFs and ARID1A-dependent transcriptional network. Network of known and predicted interaction partners. FAS-reg-TFs, which are not DE, and other TFs, expressed in our cell lines, DE upon ARID1A loss, identify RUNX3 as a potential regulator of FAS dependent on ARID1A mutation status.

4.5.10 RUNX3 chromatin accessibility and expression are reduced upon ARID1A loss

We identified RUNX3 as a potential FAS-regulating co-TF from the previous analysis. Therefore, we checked whether *ARID1A* mutations had a direct regulatory effect on *RUNX3* by testing it for differential chromatin openness in MUT versus WT *ARID1A* clones. Interestingly, we found that the *RUNX3* promoter region was partially closed (**Figure 30 A-B**) and RNA expression (**Figure 30 C-D**) reduced in the presence of *ARID1A* mutation. Downregulation of *RUNX3* at gene level was confirmed by RT-qPCR (**Figure 30 E**). Contrary, *ETS1* was not differentially open (**Figure 30 A-B**) nor expressed (**Figure 30 C-D**).

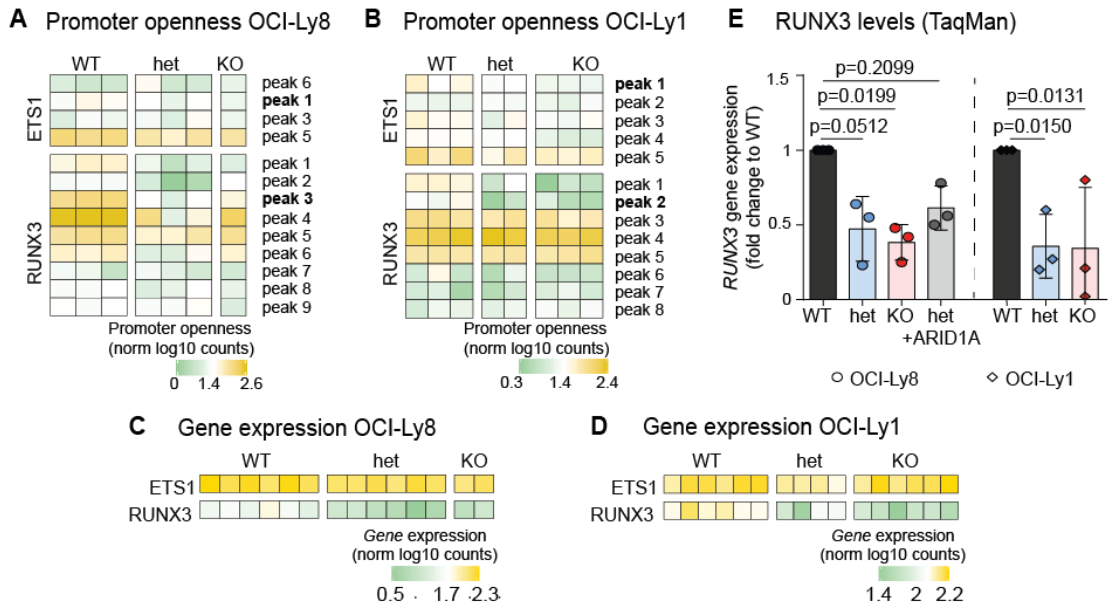


Figure 30. ETS1 and RUNX3 accessibility and expression levels. **A-B)** *ETS1* and *RUNX3* promoter openness in OCI-Ly8 (A) and OCI-Ly1 (B). *ETS1* openness does not change upon *ARID1A* loss. Contrary *RUNX3* openness is reduced. **C-D)** *ETS1* and *RUNX3* gene expression levels in OCI-Ly8 (C) and OCI-Ly1 (D). *ETS1* expression does not change upon *ARID1A* loss; contrary *RUNX3* levels decrease. **E)** *RUNX3* gene expression levels. Downregulation in *ARID1A* mutant clones is confirmed by RT-qPCR (n = 3). Pooled data from biological replicates (n) are represented as mean \pm SD; p values are from ANOVA analysis.

RUNX3 decrease at gene level was translated into reduced protein abundance, as showed by immunoblot analysis (Figure 33). In addition, I tested the predicted physical interaction between *RUNX3* and *ETS1* experimentally. OCI-Ly1 WT *ARID1A* had high *RUNX3* levels; therefore, I selected OCI-Ly1 for performing a co-IP experiment. *ETS1* was immunoprecipitated, and *RUNX3* immunoblotting was performed. *ARID1A* WT single cell-derived clone showed higher levels of *RUNX3* compared to *ARID1A* KO, while *ETS1* levels were not affected by the presence of *ARID1A* mutation (Figure 31).

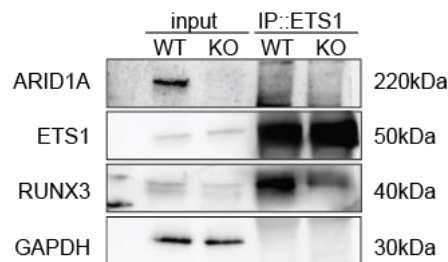


Figure 31. Western blot of ETS1 immunoprecipitates (IP) from OCI-Ly1 native (#A3) and KO (#G1) single-cell-derived clones, showing co-immunoprecipitates of RUNX3.

Overall, our data indicate that *ARID1A* mutations are associated with reduced chromatin accessibility at the *RUNX3* promoter resulting in reduced *RUNX3* expression, while *ETS1* levels are unaffected. Besides, we showed that *RUNX3* and *ETS1* interact at protein level in a FL-like system.

4.5.11 ETS1 but not RUNX3 alone, regulates *FAS* transcription

Our bioinformatics analysis identified several ETS1 TF binding motifs on the *FAS* promoter (**Figure 32 A-B**), which were enriched in the accessible chromatin regions (**Figure 32 A**). To experimentally assess whether ETS1 directly regulates *FAS* transcription through physical binding to its promoter, we performed a luciferase reporter assay in HEK293T cells. This model system was selected since it is characterized by low endogenous levels of our targets (*FAS*, *ETS1*, and *RUNX3*). First, we cloned into a pGL3-Basic vector two regions of *FAS* promoter (pGL3-*FAS* 332 bp and 537 bp) containing six potential ETS1 binding sites (**Figure 32 A**). Next, we co-transfected the pGL3-*FAS* constructs with the luciferase reporter and increasing doses of *ETS1* or *RUNX3* expression vectors. Different concentrations of the vectors (0 ng, 50 ng, 200 ng, and 500 ng) were tested (**Figure 32 C-D**). One day after transfection, we detected dose-dependent transactivation activity for *ETS1*, showing that *ETS1* is a direct *FAS*-reg-TF (**Figure 32 C**). Contrary, we did not detect transactivation activity with *RUNX3* only (**Figure 32 D**).

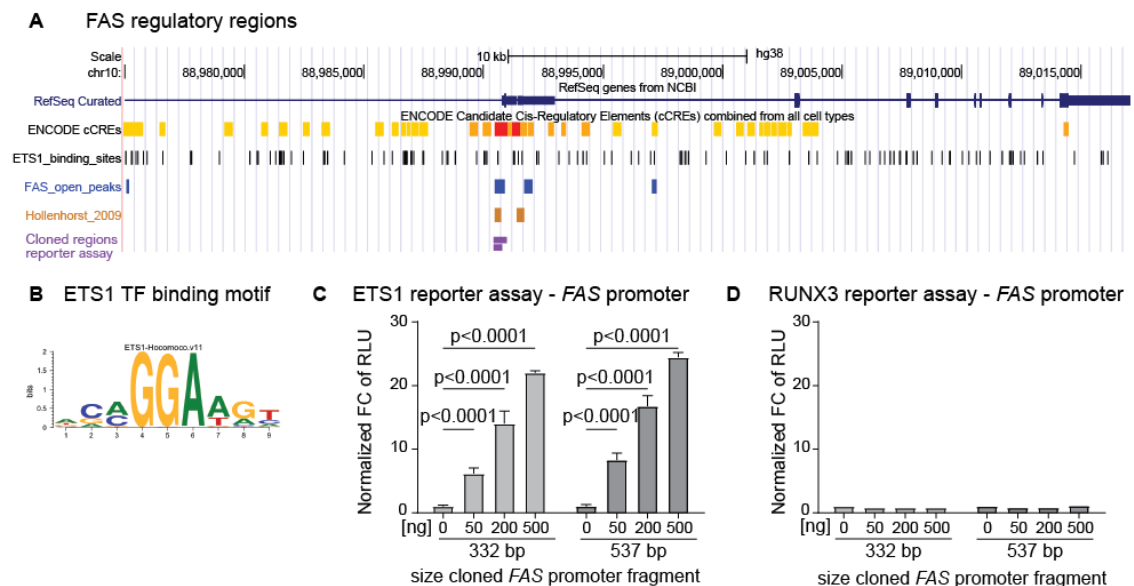


Figure 32. ETS1 but not RUNX3 alone regulates *FAS* transcription. **A)** *FAS* gene with annotated enhancer regions (yellow) and promoter (red). ETS1 binding site (black), accessible chromatin regions from our ATAC-Seq data (blue), ETS1 binding to *FAS* promoter from published (Hollenhorst, Chandler et al. 2009) ChIP-Seq data (brown), and *FAS* promoter regions cloned for the reporter assay (purple). **B)** ETS1 TF binding motif in *FAS* accessible promoter regions. **C)** Luciferase reporter assay, co-transfection of the *ETS1* expression vector, and pGL3-*FAS* constructs (n = 3). **D)** Luciferase reporter assay, co-transfection of the *RUNX3* expression vector, and pGL3-*FAS* constructs (n = 3). Pooled data from biological replicates (n) are represented as mean \pm SD; p values are from ANOVA analysis.

These results support the crucial role of *ETS1* as a transcriptional regulator of *FAS* while showing that the expression of *RUNX3* alone is not sufficient to induce changes in *FAS* expression. Further experiments need to be performed to show the cooperative action of *RUNX3* and *ETS1* in controlling *FAS* transcription in FL-like systems.

4.5.12 FAS phenotype upon RUNX3 overexpression in *ARID1A* mutant clones

To confirm the role of RUNX3 in FAS regulation, I overexpressed RUNX3 in *ARID1A* het and KO clones using a tetracycline-inducible viral vector. As a control for further experiments, I used *ARID1A* het and KO untransduced clones treated with doxycycline. Successful vector expression was validated by immunoblot analysis, which showed increased RUNX3 levels (**Figure 33**).

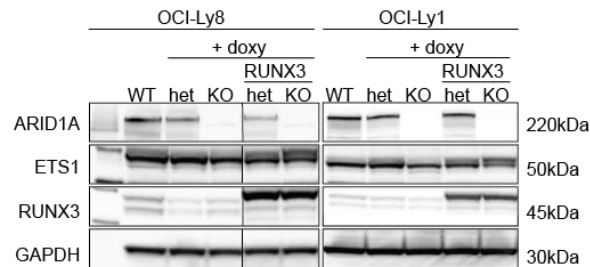


Figure 33. Western blot of RUNX3 over-expressing clones. OCI-Ly8 and OCI-Ly1 with *ARID1A* WT and *ARID1A* het or KO clones, with or without stable over-expression of RUNX3, treated with doxycycline.

Next, I used the clones with RUNX3 overexpression to test if FAS levels were rescued. RT-qPCR data showed upregulation of *FAS* at gene levels in both cell lines (**Figure 34 A**). *FAS* increase was translated into significantly higher FAS surface levels (**Figure 34 B**). In OCI-Ly8 *ARID1A* het clone, over-expression of RUNX3 was able to ultimately rescue FAS to the level of the control clone, while in the *ARID1A* KO clone, the rescue was only partial. Contrary, in OCI-Ly1 *ARID1A* het and KO clones, the rescue of FAS was only partial upon RUNX3 over-expression. FAS rescue phenotypes (**Figure 34**) correlate with the over-expression levels of RUNX3, which are higher in OCI-Ly8 compared to OCI-Ly1, as shown by western blotting (**Figure 33**).

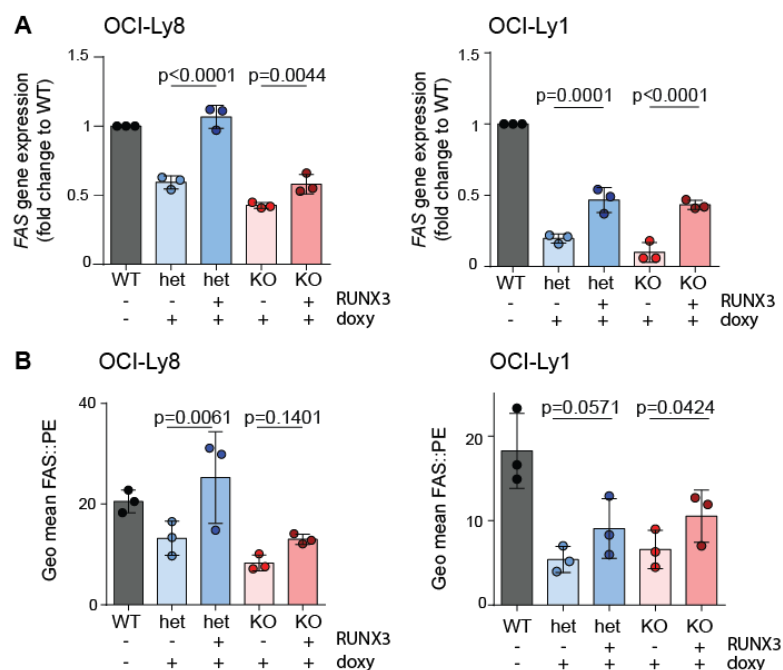


Figure 34. RUNX3 over-expression rescues FAS gene and protein levels. **A)** FAS gene expression fold change in OCI-Ly8 (left) and OCI-Ly1 (right) assayed by RT-qPCR ($n = 3$). **B)** FAS protein levels in OCI-Ly8

(left) and OCI-Ly1 (right) assayed by flow-cytometry ($n = 3$). Pooled data from biological replicates (n) are represented as mean \pm SD; p values are from ANOVA analysis.

The data suggest RUNX3 overexpression on *ARID1A* mutant background can partially rescue FAS levels, in FL-like cell lines.

4.5.13 FAS rescue upon RUNX3 overexpression is functionally relevant

Finally, we aimed to validate the functional relevance of FAS rescue upon RUNX3 upregulation. First, I performed FASLG-induced apoptosis experiments in OCI-Ly8 and OCI-Ly1. The results showed that over-expression of RUNX3 specifically re-sensitized *ARID1A* mutant clones to FASLG-induced apoptosis (**Figure 35 A-B**, $n = 3$). Next, I co-cultured OCI-Ly8 clones overexpressing RUNX3 and CD8+ T lymphocytes. Similar to the previous experiments (**Figure 24**), the killing rate was measured as the percentage of AnnexinV+ cells. Again, the data showed that RUNX3 over-expression resulted in the rescued killing ability of the CD8+ T cells (**Figure 35 C**, $n = 5$, $p = 0.0144$ het+RUNX3 vs het, $p = 0.0203$ KO+RUNX3 vs KO).

In conclusion, we showed that overexpression of RUNX3 in an *ARID1A* mutant FL-like cell line is functional and rescues FASLG-induced apoptosis resistance, in *ex vivo* co-culture systems and by treatment with a recombinant FASLG protein.

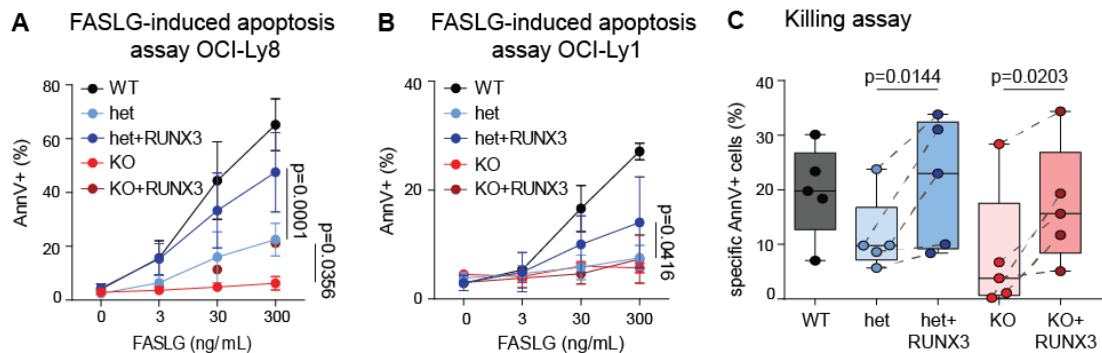


Figure 35. FAS rescue upon RUNX3-overexpression is functionally relevant. **A-B**) Percent of dying (AnnexinV+DAPI- and AnnexinV+DAPI+) OCI-Ly8 (A) and OCI-Ly1 (B) cells upon treatment with soluble FASLG ($n = 3$). Cells were incubated for 24 h with an increasing dose of soluble FASLG. Pooled data from biological replicates (n) are represented as mean \pm SD; p values are from ANOVA analysis. **C**) Percent of dying (AnnexinV+DAPI- and AnnexinV+DAPI+) OCI-Ly8 cells upon treatment with soluble FASLG ($n = 3$). Cells were incubated for 24 h with an increasing dose of soluble FASLG.

4.5.14 Summary

In summary, our results suggest that in *ARID1A* mutant FL-like systems, the *RUNX3* promoter is less accessible, leading to reduced RUNX3 levels. Furthermore, the decrease in RUNX3 impairs the interaction with ETS1, which is a direct *FAS*-regulating TF. This leads to reduced FAS levels resulting in lower sensitivity to FASLG- and T cell-mediated killing of FL cells (**Figure 36**). Here, we uncovered a novel molecular mechanism by which *ARID1A* indirectly regulates FAS expression in FL.

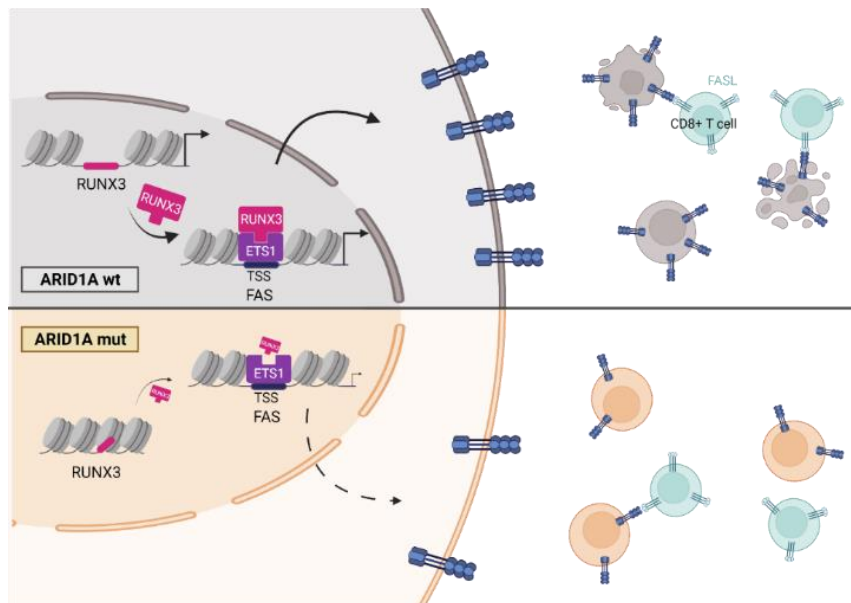


Figure 36. Novel *FAS*-regulatory network dependent on *ARID1A* mutation in FL. *ARID1A* mutations in FL reduce the accessibility of the *RUNX3* promoter, which results in lower RUNX3-ETS1 cooperativity. Thus, lower *FAS* transcription and response to FASLG-induced apoptosis.

4.6 *ARID1A* mutations impact T cells functions in FL

Whole transcriptome analysis of our CRISPR/Cas9 clones showed downregulation of several immune response-related GOs. Among the enriched terms in the *ARID1A* mutant clones, T cell activation, differentiation and cell-cell cross-talk via synapse formation were highlighted. Therefore, we investigated the role of *ARID1A* mutations on the cross-talk with T cells.

4.6.1 TME-derived gene expression signatures

First, we focused on re-analyzing the digital quantitative gene expression profiling (GEP; Nanostring) from all available primary patients samples belonging to the GLSG2000 cohort with known mutational profile (Pastore, Jurinovic et al. 2015) and with existing Nanostring data (Tobin, Keane et al. 2019). FL biopsies with *ARID1A* mutations (n = 12) generally showed downregulation of gene sets associated with cell-cell communication and cell-cell interaction compared to *ARID1A* WT (n = 39) (Figure 37). Notably, we observed reduced chemokines and cytokines secretion in the *ARID1A* mutant group, biological adhesion, and cytotoxicity. In conclusion, data analysis suggested that *ARID1A* loss influences several TME-derived gene expression signatures in primary FL.

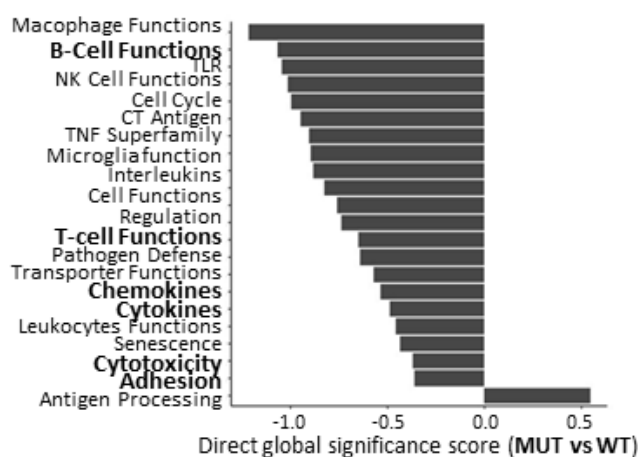


Figure 37. TME-derived gene expression profile in primary FL. Digital quantitative gene expression profiling (GEP).

4.6.2 Whole-transcriptome of FL-like cell lines shows deregulation of cytoskeleton and plasma membrane functions upon *ARID1A* loss

Next, we aimed to characterize the underlying molecular biology in FL-relevant model systems. We further analyzed the transcriptome data obtained from OCI-Ly1, OCI-Ly8, and DB CRISPR/Cas9 single cell-derived clones with and without *ARID1A* mutation (Table 15) to precisely assess the biological and molecular functions of significant DE genes (MUT vs WT). Here, we were able to describe, with a non-directional analysis, the DE genes in terms of their cellular component, biological process, and molecular functions. We performed word cloud analysis, where we attributed a weight (size of the word in the cloud) to every word appearing in the GO terms derived from DE genes analysis. Many DE genes clustered to the cellular components of the plasma membrane region, cell surface and cytoskeleton (Figure 38 A). Analyzing the biological process, we observed that DE genes regulated cell-cell interaction, cell activation and differentiation, cell adhesion and cell migration (Figure 38 B). Significant DE genes encompassed mainly

cell membrane receptors and transmembrane molecules (**Figure 38 C**). Our data revealed the crucial role of *ARID1A* mutation in regulating cell membrane functions, which affect cell-cell interaction and cross-talk via the deregulation of receptors and transmembrane molecules.

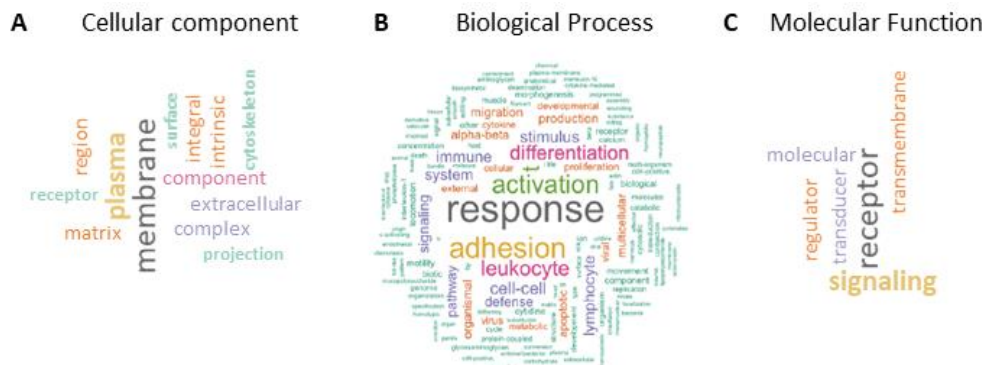


Figure 38. Plasma membrane functions are altered upon *ARID1A* loss. Analysis of non-directional DE genes (RNA-Seq) in *ARID1A* mutant clones **A**) GOrilla – cellular component analysis. **B**) GOrilla – biological process analysis. **C**) GOrilla – molecular function, exemplary plots of OCI-Ly8 (MUT vs WT).

4.6.3 *ARID1A* loss impacts cellular stiffness

By performing a non-directional analysis, accounting for all DE genes in our RNA-Seq data set (MUT vs WT), we identified the plasma membrane among the cellular components affected by *ARID1A* loss (**Figure 38**). Recent publications (Moriarty, Mili et al. 2022, Wang, Jiang et al. 2022) pointed out how intrinsic physical properties of the cells are involved in regulating the behavior in the TME.

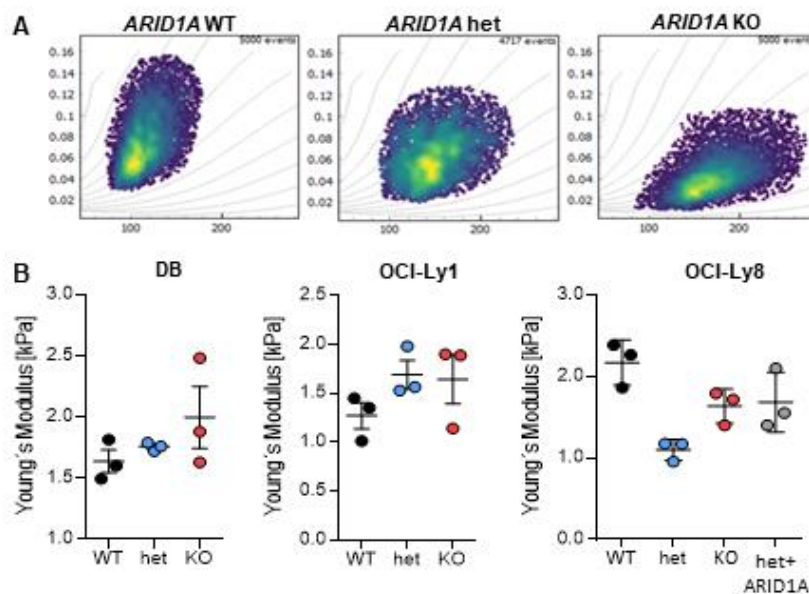


Figure 39. *ARID1A* loss impacts cellular stiffness and cell membrane plasticity. **A**) Deformability Cytometry (RT-DC) assay was performed to determine the effect of *ARID1A* loss on the morpho-rheological phenotype. **(A)** Representative density blots of cell size vs deformation of OCI-Ly8 cell line (*ARID1A* WT, het, KO) (n = 3). **(B)** Young's Modulus indicative of cellular stiffness was derived from the RT-DC results by established analytical and numerical models (n = 3). Pooled data from biological replicates (n) are represented as mean \pm SD;

Here, we performed real-time deformability cytometry (RT-DC) experiments to test if *ARID1A* mutations have a functional impact on cellular stiffness and plasma membrane plasticity. Overall, the data showed an effect of *ARID1A* loss on the analyzed parameter (**Figure 39 A, B**). However, the results obtained in the three analyzed cell lines are not consistent. DB and OCI-Ly1 *ARID1A* mutant clones are characterized by increased stiffness, while OCI-Ly8 *ARID1A* mutant clones are characterized by reduced stiffness, which augments upon *ARID1A* over-expression.

4.6.4 *ARID1A* mutations impair conjugates formation with CD4+ T cells in FL-like models

To functionally validate these results, we used *ex vivo* co-culture systems, which enabled us to test if the altered cell membrane functions had a biological impact on T cells. Previously, our experiments (**Figure 24 C**) showed that *ARID1A* mutations did not change the ability of FL-like cell lines to interact with healthy CD8+ T lymphocytes.

Next, we co-cultured OCI-Ly8 *ARID1A* WT, het and KO mutant clones with CD4+ T lymphocytes from healthy donors ($n = 3$) in the presence or absence of CytostimTM. We assayed immune synapse formation potential by flow-cytometry by staining OCI-Ly8 clones with CFSE dye and CD4+ cells with VPD dye. As read-out, we used the percent of double positive events (CFSE+VPD+), B-T cells interacting with each other. The data showed a significant decrease in cell-cell conjugate formation in *ARID1A* het ($p = 0.0332$) and *ARID1A* KO ($p = 0.0270$) clones (**Figure 40 A**). Decreased conjugates formation upon *ARID1A* loss was associated with reduced MHCII levels on the cell surface (**Figure 40 C**).

In addition, we analyzed the co-cultured cells by fluorescence microscopy, having OCI-Ly8 clones labeled with CFSE dye and unlabeled CD4+ cells. We stained the cellular membrane with ActinRed 555 ReadyProbes Reagent to visualize the immune synapse. Interestingly we observed that the cytoskeleton (actin) polymerization at the point of cell-cell contact is impaired upon *ARID1A* loss (**Figure 40 B**).

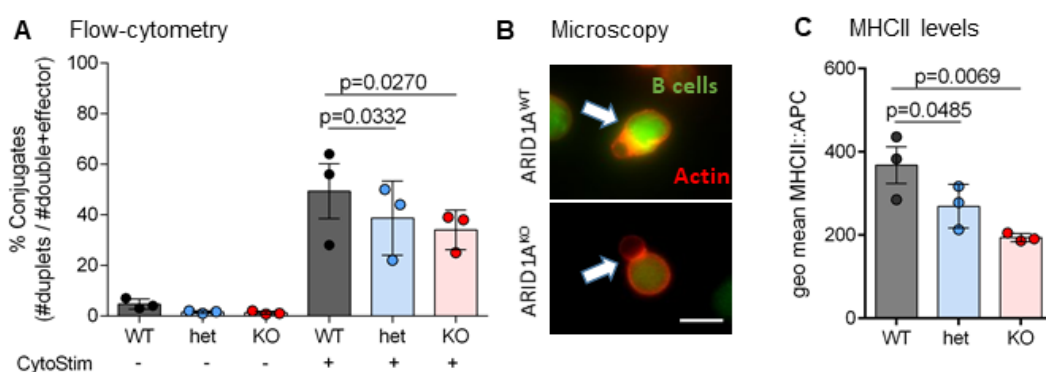


Figure 40. Immune synapse formation in OCI-Ly8 clones. A) Percent of conjugates formation of OCI-Ly8 cells upon 15 minutes co-culture with CD4+ T-cells ($n = 3$, biological replicates performed with different healthy T cell donors). Pooled data from biological replicates (n) are represented as mean \pm SD; p values are from ANOVA analysis. **B)** Representative fluorescent microscopy images of co-cultured OCI-Ly8 (green) and CD4+ T cells (unlabeled). The white arrow indicates the immune synapse formation. The scale bar is 20 μ m. **C)** MHCII surface levels measured by flow-cytometry. Pooled data from biological replicates (n) are represented as mean \pm SD; p values are from ANOVA analysis.

To analyze more physiological settings, we established *ex vivo* autologous co-cultures. Here, we used BCL cells with and without *ARID1A* knockdown (RFP+), co-cultured with CD4+ T cells isolated from the tonsil tissue of matched donors ($n = 3$, donor #768, #655, #637). Flow-cytometry analysis confirmed the results of the allogeneic co-cultures, showing reduced BCL – T cell doublets in *ARID1A* knockdown clones (sh4 vs scr $p = 0.01$, sh6 vs scr $p = 0.01$) (**Figure 41**).

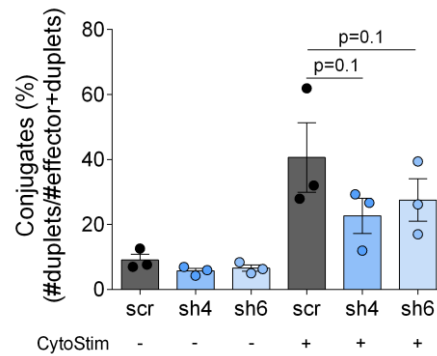


Figure 41. Immune synapse formation in BCL cells. Percent of conjugates formation of BCL cells with and without *ARID1A* knockdown upon 15 minutes of co-culture with autologous CD4+ T-cells ($n = 3$). Pooled data from biological replicates (n) are represented as mean \pm SD; p values are from ANOVA analysis.

Our data demonstrate that the immune synapse formation with CD4+ T lymphocytes in FL models highly depends on *ARID1A* mutation status.

4.6.5 Summary

In conclusion, sequencing data suggest that *ARID1A* mutations affect the cytoskeleton and plasma membrane functions of FL-like cells. Experimental *ex vivo* data show that *ARID1A* loss alters the complex cross-talk with CD4+ T cells and correlates with reduced immune synapse formation.

5. Discussion

ARID1A mutations are recurrent in FL and several other cancer types. Mostly they are inactivating mutations and lead to protein haploinsufficiency (Wu, Wang et al. 2014, Pastore, Jurinovic et al. 2015). In this thesis, I focused on the functional characterization of *ARID1A* mutations in FL, particularly deciphering the molecular mechanism underlying reduced FAS levels upon *ARID1A* loss in FL-like models.

The significant findings of my work are that in FL-like cell lines, 1) *ARID1A* mutations result in slower cell growth and increased formation of anaphase chromatin bridges; 2) *ARID1A* deficiency renders cells less sensitive to FAS / FASLG-induced apoptosis. The mechanism by which *ARID1A* controls *FAS* expression is indirect, contrary to what is hypothesized in literature (Luo, Cheung et al. 2008), and requires the cooperation of multiple proteins; 3) *ARID1A* loss affects plasma membrane functions and immune-synapse formation with CD4+ T cells.

In conclusion, this thesis highlights several functional aspects of FL deriving from *ARID1A* mutation, which could contribute to lymphomagenesis, disease progression and relapse.

5.1 Functional characterization of *ARID1A* mutations in FL

5.1.1 *ARID1A* loss alters gene expression

Our RNA-Seq data show that *ARID1A* mutations result in the differential expression of several genes in FL-like cell lines (**Figure 14**). Deregulating gene expression leads to the enrichment of GO terms associated with cancer development and progression (**Figure 15**).

The changes in gene profile that we identified upon *ARID1A* loss are only sometimes shared among the analyzed models. Furthermore, *ARID1A* functions depend highly on partners recruited to the site of action (Wilson and Roberts 2011). Therefore, *ARID1A* mutations, together with the cellular-, mutational- and functional-context in which they are detected, could affect the clustering by cell line observed in the multi-omics experiments (**Figure 13**) and the high heterogeneity of primary FL cases.

Even though the overlap between DE genes is not prominent in our dataset, pathway analysis reveals enrichment of GOs that is consistent across cell lines and with literature. *ARID1A* silencing is reported to have a determinant role in apoptosis regulation (Luo, Cheung et al. 2008), to be associated with proliferation phenotypes (Tomihara, Carbone et al. 2021), motility and invasion potential (Sun, Wang et al. 2017, Tomihara, Carbone et al. 2021), which could be due to altered cytoskeleton functions. Together these and our data suggest a highly context-dependent role of *ARID1A* mutations in transcriptional programming.

Given the high frequency of *ARID1A* mutations in FL, it is of primary interest to understand the downstream molecular consequences of *ARID1A* loss for the potential discovery of therapeutic targets.

5.1.2 *ARID1A* mutation causes cell growth defects and chromatin bridges formation

In the context of FL, we describe how *ARID1A* mutations play a crucial role in regulating cell growth, leading to reduced proliferation (**Figure 16**). Besides, we report *ARID1A* loss to correlate with increased formation of chromatin bridges at anaphase (**Figure 18**).

5.1.2.1 *ARID1A* mutation determines cell growth phenotype

A widespread feature of cancer cells is the de-regulation of cell growth, suggesting that alteration of proliferative rate is pivotal in oncogenesis. Yet, a still unresolved paradox is how the growth disadvantage, dependent on *ARID1A* mutation (**Figure 16**), could prompt lymphomagenesis, which is characterized by uncontrolled cell proliferation. Supporting the idea that slow-proliferating cells have a selective advantage during disease development, there is the “Poor competition model” described by Bilousova *et al.* (2005) (Bilousova, Marusyk *et al.* 2005). Here, the authors showed how acquiring disadvantageous genetic mutations that impair DNA replication and cell cycle progression could result in a proliferative advantage when combined with specific oncogenic mutations. Even though there is no evidence that *ARID1A* mutations are an early event during lymphomagenesis, the “Poor competition model” suggests a fascinating concept and enforces the idea of mutations having a context-specific role.

Despite the hypothesis postulated in the “Poor competition model”, the *ARID1A* mutation-dependent growth phenotype is unlikely to contribute to lymphomagenesis. On the other hand, a slower growth rate could represent a selective advantage in relapsed-refractory FL cases, where our laboratory has observed an increase in *ARID1A* mutation frequency compared to diagnosis (**Figure 42**). Standard immunochemotherapy regimens applied in FL management, i.e. R-CHOP and R-bendamustine, are, among other functions, anti-mitotic drugs and target fast-cycling cells. Therefore, loss of *ARID1A* could represent an adaptive mechanism of FL cells that renders them intrinsically refractory to drug treatment and able to survive chemotherapy. Slow-cycling cells can persist in the body and potentially give origin to cancer relapse due to clonal expansion. Consistent with this hypothesis, other *ARID1A*-deficient cancers (e.g. endometrioid cancer) are reported to be less sensitive to cisplatin therapy regimen and consequently result in shorter PFS and early metastasis development (Katagiri, Nakayama *et al.* 2012, Werner, Berg *et al.* 2013, Mullen, Kato *et al.* 2021).

5.1.2.2 *ARID1A* mutations are associated with hallmarks of chromatin instability

In addition to a slower growth rate upon *ARID1A* loss, we describe increased chromatin bridge formation (**Figure 18**). Chromatin bridges result from impaired DNA damage repair process and are linked to genomic instability (Burrell, McClelland *et al.* 2013), a well-known player in carcinogenesis. *ARID1A* and the SWI/SNF complex have been described as involved in protecting cells from genetic instability and DNA damage repair, including homologous recombination and non-homologous end-joining repair (Shen, Peng *et al.* 2015). Consistent with these data, our laboratory has previously shown an increase in DNA damage and double-strand break markers in *ARID1A* mutant FL-cell lines (Bararia, Heide *et al.* 2014). Therefore, if DNA damage cannot be efficiently repaired, the genetic alteration could accumulate, suggesting a contribution of *ARID1A* mutations to malignant transformation.

In future, it would be interesting to test the “Poor competition model” in FL settings. First, we could analyze primary FL cases with limited-stage disease and check if there is a subset of genetic

alterations frequently co-occurring with *ARID1A* mutations. This would potentially allow the identification of genetic events that alone seem not to provide a selective advantage to cancer cells but, in combination, could promote lymphomagenesis. Next, we could introduce stable *ARID1A* loss in our *ex vivo* BCL culture model and monitor the acquisition of mutations over time. The experiment will help identify *ARID1A* mutation-dependent genetic events, which would be useful for getting new insights into FL ontogeny.

5.1.3 *ARID1A* mutation results in reduced FAS levels and FASLG-induced apoptosis

5.1.3.1 RUNX3 and ETS1 cooperate to regulate *FAS* expression in *ARID1A*-mutant FL-like model system

Here, we unravel the molecular mechanism underlying reduced *FAS* levels in FL and show that *ARID1A* regulation is indirect, disproving the earlier model that hypothesized direct control at the *FAS* promoter by *ARID1A* (Figure 27) (Luo, Cheung et al. 2008). In FL, *ARID1A* mutation influences RUNX3-ETS1-*FAS* transcriptional network by regulating the chromatin openness of the *RUNX3* promoter (Figure 30). To what extent this mechanism applies to other cancers remains unclear.

Inactivation of RUNX3 is extensively observed in solid cancers, yet dependence on *ARID1A* mutation was not previously reported. In cancer, *RUNX3* genetic mutations have been rarely observed; on the other hand, epigenetic regulation through aberrant DNA methylation or histone modifications is frequent (Fujii, Ito et al. 2008, Chuang and Ito 2010, Lee 2011). Here, we describe another epigenetic mechanism controlling *RUNX3*, the regulation of chromatin accessibility. Interestingly, *RUNX3* and *ARID1A* are located on chromosome 1p36, a region commonly deleted in cancer (Godfried, Veenstra et al. 2002, Poetsch, Dittberner et al. 2003). In addition, RUNX3 function, as well as *ARID1A*, is highly context-specific. RUNX3 presents multiple protein interaction domains, indicating that it is involved in several processes. Among other functions, RUNX proteins are shown to cooperate with the SWI/SNF complex in transcription regulation (Chuang, Ito et al. 2013), as in the regulation of TME (Chuang, Ito et al. 2013, Manandhar and Lee 2018).

Members of the RUNX family and ETS1 have been previously identified as DNA binding partners in Jurkat T cells and mice models (Hollenhorst, Shah et al. 2007). Moreover, ETS1 and RUNX recognition motifs are often juxtaposed at enhancer regions of several genes crucial for T cell differentiation and activation (Hollenhorst, Chandler et al. 2009), suggesting a cooperative activity of the two.

Our data, showing that RUNX3-ETS1 network is involved in promoting *FAS* expression in FL-like cells (Figure 31-34), add evidence to literature already showing how TFs act cooperatively (Morgunova and Taipale 2017, Ibarra, Hollmann et al. 2020).

5.1.3.2 Impaired FAS / FASLG-induced apoptosis is a common immune evasion mechanism adopted by FL-cell

Here, I show that *ARID1A* mutations lead to reduced *FAS* levels (Figure 20, Figure 21), rendering cells less sensitive to FAS / FASLG-induced apoptosis (Figure 22, Figure 23). Reduced sensitivity to the FAS / FASLG-induced apoptosis pathway is a crucial adaptive mechanism that favors disease onset, progression, and relapse.

In this work, we observed another case supporting the idea that impaired FAS / FASLG-induced apoptosis is a common immune evasion mechanism adopted by FL-cells. As mentioned above, DB cell line was not used to perform apoptosis assays. Whole-transcriptome analysis showed that *FAS* levels were already very low in *ARID1A* WT controls. *FAS* gene was filtered out in the beginning of the workflow since the mean raw count, across all analyzed clones, was less or equal to 5. In DB, low *FAS* levels are not associated with *ARID1A* mutations. Yet, considering the crucial advantage conferred by *FAS* down-regulation to FL cells, other genetic or epigenetic alterations could phenocopy *ARID1A* loss.

During lymphomagenesis, pre-malignant clones undergo several rounds of somatic hypermutation and clonally expand. Mutant cells with low BCR affinity should be negatively selected during the germinal center reaction (Takahashi, Ohta et al. 2001, Hao, Duncan et al. 2008) by the interaction with CTLs acting mainly via FAS / FASLG-induced apoptosis pathway (Butt, Chan et al. 2015). Germinal center negative selection is a crucial mechanism of immune surveillance, and evasion of this step could result in cancer formation. Therefore, acquiring *ARID1A* mutations during the early stage of lymphomagenesis represents a selective advantage for cancer cells. *ARID1A*-mutant FL cells, characterized by low *FAS* levels, are more likely to evade CTLs immune surveillance in the germinal center and favor cancer onset.

Active CTLs and functional FAS / FASLG-induced apoptosis are crucial during lymphomagenesis and disease progression. During disease development in the GC, CTLs are involved in negative B cell selection (Butt, Chan et al. 2015), while later in cancer cell clearance (Golstein and Griffiths 2018). CTLs, recruited to the site of action by TME partners, should be able to actively recognize and kill the target cells. Cancer cell clearance is a multistep mechanism beginning when CTLs physically interact with the target cells via immune synapse formation and kill them via activation of FAS pathway and release of cytotoxic molecules (Golstein and Griffiths 2018). Here, we show that the interaction potential of FL-like cells and CTLs is not altered by *ARID1A* mutation (**Figure 24 C**). Yet, reduced *FAS* levels significantly affect cancer cell clearance (**Figure 24 B**). The *ARID1A* mutation-dependent immune evasion mechanism we describe is one of many adopted by FL cells. In literature, there are other examples of how FL cells shape the TME and evade CTLs control. FL cases involving bone marrow showed that FL cells promoted the recruitment of supportive TME and consequent exclusion of CTLs (Mulder, Wahlin et al. 2019).

In addition to the pivotal role in lymphomagenesis and disease progression that we just discussed, *ARID1A* mutations might also have a functional impact on relapse formation. With the development of novel immunotherapies, the aim is to exploit the immune system (e.g. T cells) to specifically target and eliminate cancer cells. If the cancer cells adopt intrinsic immune evasion mechanisms, i.e. low *FAS* levels on the surface, they will likely be less sensitive to immunotherapies. This will facilitate relapse formation since a subset of FL cells cannot be efficiently cleared.

The role of *ARID1A* mutations, and *FAS* loss, in preventing cancer cell clearance and thus having a positive role in relapse onset is supported by unpublished data from an in-house study, based on the CoEvoL cohort (**Figure 42**). Here, we analyzed FL biopsies (n = 70) and compared the frequency of *ARID1A* and *FAS* mutations in patients with advanced-stage disease (n = 40), before the initiation of frontline therapy, or with relapsed/refractory (r/r) disease (n = 30). Matching our hypothesis that reduced sensitivity to FASLG-induced apoptosis confers a selective advantage to FL, we identified accumulation of *ARID1A* mutations in the r/r group (n = 6/30, 20%) compared to the advanced-stage disease group (n = 6/40, 15%). In addition, we analyzed the frequency of *FAS* mutation, an alternative mechanism to evade FASLG-induced apoptosis (Totten, Gaucher

et al. 2014, Razzaghi, Agarwal et al 2020), in the two groups and found them to be enriched in the r/r group.

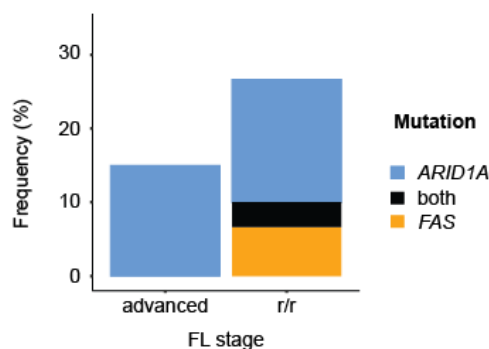


Figure 42. *ARID1A* and *FAS* mutation frequency at advanced-stage or r/r disease.

Overall, the data strongly suggest that the acquisition of *ARID1A* mutations represents a clinically relevant immune evasion mechanism in FL. Indeed, decreased *FAS* levels and consequent resistance to FASLG-induced apoptosis, confer a selective advantage to FL cells during several steps of disease development.

5.1.4 *ARID1A* mutations affect the complex cross-talk with T cells

Analysis of digital quantitative gene expression profiling data shows that human primary FL samples bearing *ARID1A* mutations are characterized by reduced T cell functions (**Figure 37**). Moreover, the same samples present lower cytokines and chemokine levels than *ARID1A* wild-type cases (**Figure 37**). These data support the tumor suppressive role of *ARID1A*.

In line with the reduced T cell functions and levels of secreted molecules observed in primary FL cases with *ARID1A* loss (**Figure 37**), we described the crucial role of *ARID1A* mutation in impairing immune-synapse formation with CD4⁺ T lymphocytes, using *ex vivo* co-culture models (**Figure 41**). Our laboratory has previously shown that a subset of CD4⁺ T cells, named T follicular helper cells (Tfh), has tumor-supportive functions in FL (Bararia, Hildebrand et al. 2020). It is interesting to observe how *ARID1A* mutations, which we have discussed being beneficial for cancer formation and progression, disrupt the interaction with CD4⁺ T cells (**Figure 40****Figure 41**). The cell-cell cross-talk, and the role of single TME components is not fully elucidated (Dobaño-López, Araujo-Ayala et al. 2021, Kumar, Pickard et al. 2021). Tfh cells represent only a small part of peripheral blood total CD4⁺ T cell population. CD4⁺ T lymphocytes specific function is to coordinate the immune response by secretion of cytokines and stimulate other immune cells, like CD8⁺ CTLs and antibody-producing cells (Tay, Richardson et al. 2021). Therefore, impairing immune synapse formation could be beneficial for cancer cells, to reduce CTL activation and consequent immune response.

Previous studies from Ramsay *et al.* (2009) have shown that FL cells can alter the T lymphocytes ability to form functional immune synapses, resulting in defective actin polymerization (Ramsay, Clear et al. 2009). However, the results were variable, and the molecular driver mechanism of the phenotype remains to be entirely elucidated. Since FL is a highly heterogeneous disease, it is of great interest to analyze the mutational profile of samples to find molecular drivers of immune evasion. By exploiting our fully human primary *ex vivo* FL co-culture model, I identify *ARID1A*

mutations as one determinant of immune escape. However, validating our findings by performing co-cultures of FL cells and the autologous immune components derived from primary FL samples with known mutational status would be interesting and potentially predictive of immunotherapy response.

The impaired immune-synapse formation could also explain the challenge in using tumor-vaccination therapies, inducing a tumor-specific immune response (Kwak, Campbell et al. 1992, Bendandi, Gocke et al. 1999, Redfern, Guthrie et al. 2006, Ai, Tibshirani et al. 2009). At first, studies conducted for implementing idiotypic cancer vaccines seemed very promising since they showed improved patients outcome (Bendandi, Gocke et al. 1999, Redfern, Guthrie et al. 2006). Unfortunately, in a later stage of experimentation, the results were not reproducible, and FL patients treated with the vaccines did not show increased immune response (Ai, Tibshirani et al. 2009). One of the possible explanations for the challenges faced by tumor-vaccination therapies could be the inability of specific FL cell subsets to form immune conjugates. Educating immune cells in the recognition of their targets and the ability of target cells to form functional synapses are essential to induce killing and cancer clearance.

There are multiple determinants for impaired synapse formation. Among these, we find the expression and localization of cytoskeletal components. Moreover, synapse formations and their functionality are not only determined by molecular characteristics of the plasma membrane but also by the biophysical properties of the cancer cells and immune cells. Investigating the ability, and functional consequences, of primary FL cells to deform and their stiffness could help in gaining insight into tumors' immune evasion mechanisms (Moriarty, Mili et al. 2022, Wang, Jiang et al. 2022) and be predictive of immunotherapies efficacy (e.g. T-cell engaging therapies, checkpoint inhibitors, CAR-T cell therapies).

5.2 Clinical vulnerabilities of *ARID1A*-mutant FL cases

T cell-based immunotherapies are currently of high clinical interest and some (e.g. CD19-CAR-T cells and CD20xCD3 BiTE) have already been approved for the treatment of r/r FL. We show that *ARID1A* loss results in reduced FAS levels and FAS / FASLG-induced apoptosis. This could have a profound effect on immunotherapies efficacy, and particularly on CAR-T cell-based therapy.

CD19-directed CAR-T cells have shown initial high response rates in patients with r/r FL (Jacobson, Chavez et al. 2022, Fowler, Dickinson et al. 2022). Yet, the majority of patients will relapse after treatment termination. The molecular mechanisms underlying treatment failure is currently under investigation. Upadhyay et al. (2021) (Upadhyay, Boiarsky et al. 2021) analyzed a cohort of patients with aggressive non-Hodgkin lymphoma and positively correlated FAS levels on cancer cells with patients survival after CAR-T therapy. Here, it was first described the crucial role of the FAS / FASLG pathway in mediating T cell killing of antigen-specific cells and neighbor antigen-negative tumor cells. Moreover, another study showed that focal deletion of 10q23.3, leading to FAS loss, correlated with significantly shorter progression-free survival (PFS) and overall survival (OS) in a cohort of patients who received CD19-directed CAR-T cells for r/r large B cell lymphoma (Chern, Sun et al. 2022). Thus, loss of *ARID1A*, leading to FAS / FASLG-induced apoptosis resistance, could represent another mechanism of reduced sensitivity to CAR-T cell-based immunotherapies and ultimately promote disease relapse.

A strategy to overcome the immune evasion mechanism adopted by *ARID1A*-deficient FL could involve bispecific T cell engager (BiTE) therapies. Gruen and colleagues (Gruen, Bommert et al.

2004) showed that BiTEs induce lysis of target cells via the perforin-dependent granule-exocytosis pathway with little dependence on death ligand receptors, like FAS. The ability of BiTEs to induce the killing of target cells by a death-receptors-independent mechanism is also shown in MT110-redirected T cells, which up-regulate granzyme B secretion post treatment (Haas, Krinner et al. 2009). The efficacy of bispecific antibodies, particularly of CD20xCD3 BiTEs, is also supported by clinical data. Mosunetuzumab is approved for treatment of patients with r/r FL. It was shown to have remarkable activity, low toxicity and long-lasting effects in patients who previously received CD19-directed CAR-T cell therapy and ultimately relapsed (Budde, Assouline et al. 2022). In addition, Glofitamab was recently approved in Canada, and it showed favorable and sustained activity in patients with r/r B-NHL (Hutchings, Morschhauser et al. 2021). The functional data (Gruen, Bommert et al. 2004, Haas, Krinner et al. 2009), together with the clinical evidence (Budde, Assouline et al. 2022, Hutchings, Morschhauser et al. 2021), and our mechanistic data support the hypothesis that CD20xCD3 bispecific antibodies would be a solid and efficacious line of treatment for patients with FL harboring *ARID1A* mutation.

Overall, our analyses provide novel insights into the functional consequences of *ARID1A* mutations in FL, most notably promoting immune evasion. A better understanding of mutation-specific biology, including its impact on the tumor microenvironment, holds promise for improved patient stratification and the development of personalized treatment approaches.

6. Future Perspectives

This work has shown how *ARID1A* mutations in FL alter the plasma membrane with functional consequences. On the one hand, *ARID1A* loss resulted in reduced levels of FAS and sensitivity to FAS / FASLG-induced apoptosis. On the other hand, it altered cell surface molecular and mechanical characteristics resulting in the impaired immune synapse with CD4+ T lymphocytes.

6.1 Broadening the knowledge of *ARID1A* loss systemic impact on CD4+ and CD8+ T lymphocytes

Our RNA-Seq analysis highlighted the differential expression of ligands and receptors upon *ARID1A* loss in FL-like model systems. It is of functional interest to test if the changes at gene level were translated at protein level. Therefore, we collaborated with Julia Mergner and Christina Ludwig to perform LC/MS-MS analysis of proteins isolated from the plasma membrane (**Figure 43**). This experiment can provide valuable information for deciphering the molecular determinants of the observed phenotypes, e.g. impaired immune synapse formation.

Consistently with our previous RNA-Seq data, PCA analysis showed that the cell lines cluster separately (**Figure 43 A**). Unsupervised clustering of significantly differentially expressed surface proteins (FDR 0.05) revealed technical replicates clustering by genotype (**Figure 43 B**). In all cell lines, over 500 protein groups were detected (**Figure 43 B**). Contrary to previous sequencing results, we did not detect a strong overlap among the protein groups being significantly up- or down-regulated, in heterozygous and homozygous *ARID1A* mutant clones (**Figure 43 B**). LC/MS-MS is able to detect only the most abundant proteins expressed in a cell, which correspond to only a small fraction of the proteome. This technical limitation could explain, the poor overlap between heterozygous and homozygous *ARID1A* mutant clones, observed in the differentially expressed protein groups, of the single cell lines.

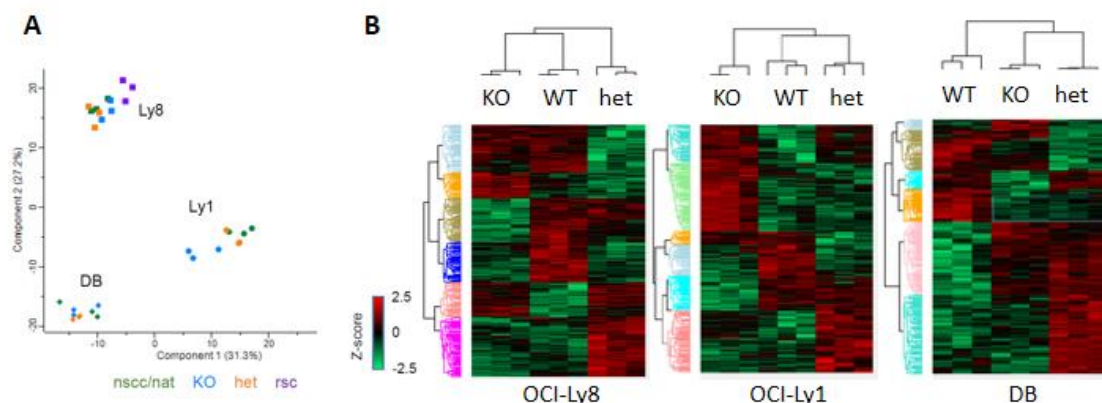


Figure 43. LC/MS-MS of plasma membrane proteins in OCI-Ly8, OCI-Ly1, and DB cell lines with and without *ARID1A* mutation. A) PCA of 9 CRISPR/Cas9 single cell-derived clones with and without *ARID1A* mutation in technical triplicates (total $n = 27$). Samples clustered by cell line (OCI-Ly8, OCI-Ly1, and DB). **B)** Heatmap of significantly differentially expressed protein groups per cell line.

With LC/MS-MS experiment, we aimed to identify molecular candidates that might affect immune synapse formation. Differential expression of proteins involved in engaging or inhibiting cell-cell interaction could be further validated using an Imaging Flow Cytometer. Following *ex vivo* co-

culture of target and effector cells, this technique allows the detection of abundance and distribution of proteins directly on the immune synapse. Gaining a better understanding of the molecular determinants involved in immune synapse formation is crucial for the development of efficacious drugs.

So far, we have used FL-like cell lines with and without *ARID1A* mutations to specifically investigate the conjugation potential with T cells subpopulations (i.e. CD4+ T cells or CD8+ T cells). In the future, we should broaden our analysis, focusing on not only single immune cell types but also performing co-cultures that include several TME-resident subpopulations. Besides, focusing on the down-stream effects of impaired synapse formation by assaying cytokines release, cell proliferation, and activation will provide new insights into disease biology.

Finally, it would be of great clinical interest and impact to test the efficacy of bispecific T cell engager antibodies (BiTEs), molecules designed to force the interaction between two cells. Among BiTEs, Mosunetuzumab is clinically approved for managing r/r FL cases that have been previously treated (Budde, Assouline et al. 2022).

I performed preliminary *ex vivo* co-cultures to test whether *ARID1A* loss affects Mosunetuzumab activity. I co-cultured CD8+ T cells from healthy donors (n = 3) with the CRISPR/Cas9 engineered OCI-Ly8 cell lines with and without *ARID1A* mutation for 4 days. CD8+ T cells cultured with *ARID1A* mutant clones in the presence of Mosunetuzumab (1 µg/mL) showed increased proliferation and activation (Figure 44 B-E) compared to *ARID1A* WT or rescue controls. In addition, the secretion of Granzyme B (Figure 44 F, G) significantly increased, and it positively correlated with FL-like cell clearance (Figure 44 A).

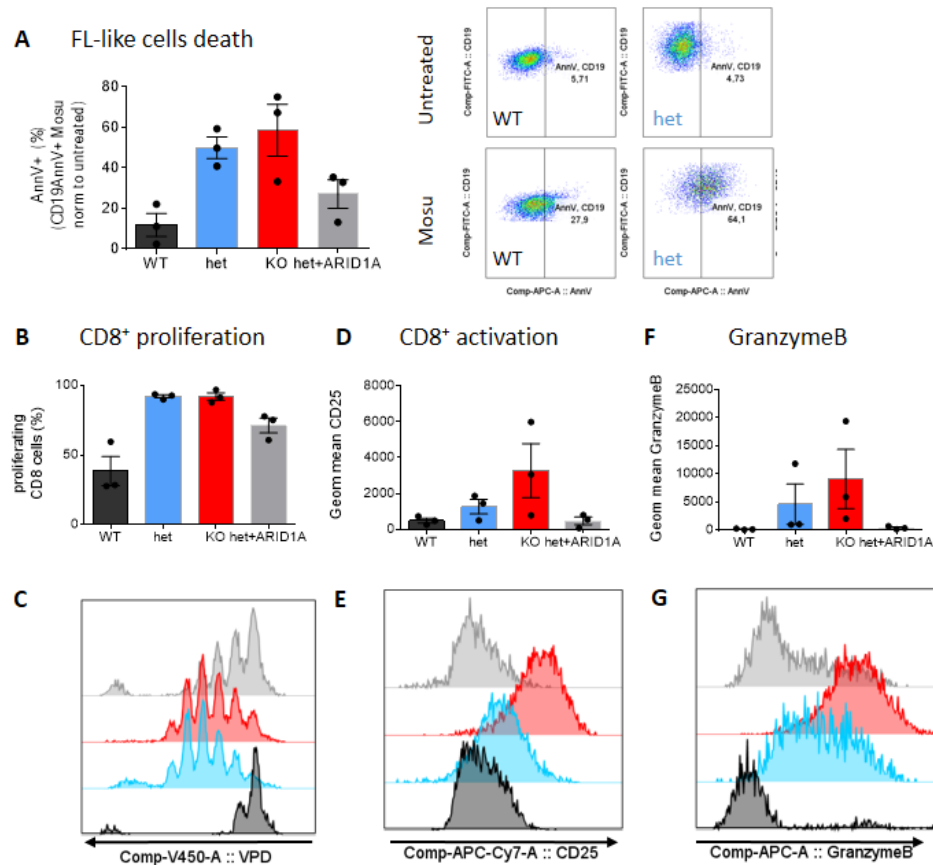


Figure 44. *In vitro* co-culture assay of CD8+ T cells with OCI-Ly8 cell lines, Mosunetuzumab effect. A) Percent of FL-Like cells (FITC+) and AnnexinV+ (APC+) normalized to untreated control at day 2. B, C)

Proliferation of CD8+ T cells (VPD+), (B) percent of proliferating cells, (C) representative FACS plot. **D, E** Activation of CD8+ T cells (VPD+), (D) geometric mean of CD25 surface expression on CD8+ T cells, (E) representative FACS plot. **F, G** Granzyme B positive CD8+ T cells, (F) geometric mean of Granzyme B intracellular expression in CD8+ T cells, (G) representative FACS plot. Pooled data from biological replicates (n) are represented as mean \pm SD.

These exciting findings need further investigation to uncover the biological mechanism underlying increased T cell activation/proliferation, and killing of *ARID1A* mutant FL cells upon treatment with Mosunetuzumab. First, other molecules could be tested to check that the observed effect is not due to specific properties of Mosunetuzumab or the CD20 receptor. Second, we need to analyze different FL-like model systems.

6.2 Gaining a comprehensive understanding of *ARID1A* loss impact on the TME

The TME is rich, and it comprises several cell types whose role is not fully elucidated (Dobaño-López, Araujo-Ayala et al. 2021, Kumar, Pickard et al. 2021). Therefore, we should focus on gaining a more comprehensive understanding of the impact of *ARID1A* loss on the different components of the TME. Performing co-cultures with only two elements (FL-like cells and CD4+ or CD8+ T cells) simplifies the reality and does not provide a realistic representation of FL complexity.

We used BCL-engineered cells obtained by human tonsil and their autologous microenvironment components to perform *ex vivo* co-cultures (preliminary data). As previously described, we obtained BCL cells by isolating GC B cells from the tonsil tissue and immortalizing them via BCL2 and BCL6 over-expression. Afterwards, we lentivirally knocked-down *ARID1A*, using two different shRNA inducible-constructs, RFP-tagged (**Figure 45 A**). From the same donor, we isolated autologous MNCs that we used in the co-culture experiment (**Figure 45 A**). This experimental set-up better represents the high physiologic complexity of FL microenvironment. We aimed to investigate whether *ARID1A* mutant cells reduced ability to form conjugates with CD4+ T cells (**Figure 41**) is cancer-supportive and results in CTL functions inhibition, as we hypothesized. In addition, our goal was to study the interplay between several cellular subsets in the context of FL.

Here, we co-cultured BCL cells with (sh4, sh6) and without (scr) *ARID1A* knockdown with autologous MNCs (1:1). MNCs population was previously depleted of CD19+ cells, in order to maintain a physiologic proportion of B cells compared to the other cell populations. On the one hand, we analyzed the conjugate formation potential of BCL cells with CD4+ T cells, CD8+ T cells, and CD56+ natural killer (NK) cells (**Figure 45 B**). As in previous experiments, conjugate formation was determined by flow-cytometry (n = 2 technical replicates). We observed that in presence of several cellular subtypes, *ARID1A* knock-down cells form less conjugates with CD4+ T cells, confirming our previous results. *ARID1A* knock-down clones showed also reduced conjugates formation with CD8+ T cells and NK cells. On the other hand, we analyzed cytokine concentration in supernatants (**Figure 45 C**), via cytokine bead array (LEGENDplex CD8/NK Panel), and detected lower levels of TNF and IL2, and increased IFN γ in the knock-down conditions. The data confirmed the immune evasive phenotype conferred by *ARID1A* loss to FL cells.

In future, we plan to use the set-up described in combination with BiTE treatment. The aim is to test whether it is possible to revert the observed phenotype and induce conjugate formation.

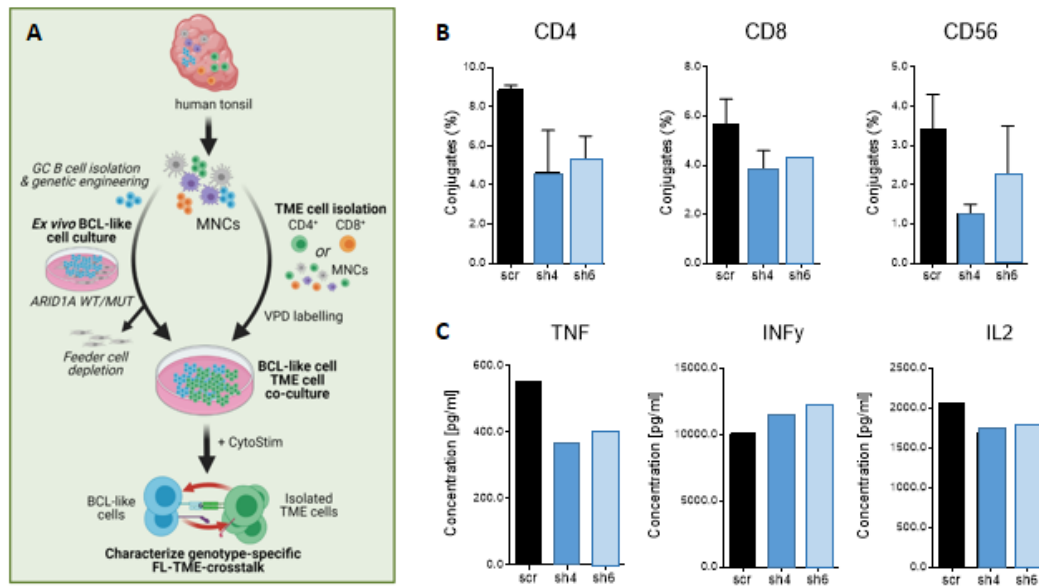


Figure 45. BCL cells co-culture with autologous TME cells. A) Schematic representation of BCL cells co-culture with autologous MNC (CD19+ cells depleted) **B)** Conjugate formation of BCL cells with CD4+ T cells, CD8+ T cells, CD56+ natural killer (NK), (n = 2, different donors). **C)** Cytokine concentrations in supernatants of BCL-Tonsil MNC co-cultures after 24 h. Cytokine bead array (LEGENDplex CD8/NK Panel).

Besides, we want to perform multi-omics analysis (ATAC-seq and RNA-seq) using the 10x Genomics technology to investigate *ARID1A* mutation-associated molecular changes occurring upon co-culture in both BCL cells and in the other cell subtypes. Here, we can test how chromatin openness and gene expression vary following co-culture in the presence or absence of *ARID1A* mutation, with single-cell resolution. Single-cell analysis is particularly valuable given the high heterogeneity of FL. In addition, the dataset could be submitted for analysis to the COMUNET algorithm (Solovey and Scialdone 2020), that will help examine specific cell-cell communication patterns and how they are altered upon *ARID1A* loss.

These experiments aim to better characterize *ARID1A* mutations and their role in regulating the described immune evasion phenotype. In addition, the goal is to investigate whether *ARID1A* loss could be predictive of treatment outcome.

References

- Abe, H., D. Maeda, R. Hino, Y. Otake, M. Isogai, A. S. Ushiku, K. Matsusaka, A. Kunita, T. Ushiku and H. Uozaki (2012). "ARID1A expression loss in gastric cancer: pathway-dependent roles with and without Epstein–Barr virus infection and microsatellite instability." *Virchows Archiv* **461**(4): 367-377.
- Adolph, L. and O. Weigert (2020). "Follikuläres Lymphom – Pathogenese, Diagnostik und Therapie." *Trillium Krebsmedizin*.
- Ai, W. Z., R. Tibshirani, B. Taidi, D. Czerwinski and R. Levy (2009). "Anti-idiotypic antibody response after vaccination correlates with better overall survival in follicular lymphoma." *Blood* **113**(23): 5743-5746.
- Alfert, A., N. Moreno and K. Kerl (2019). "The BAF complex in development and disease." *Epigenetics & Chromatin* **12**(1): 19.
- Bararia, D., M. Heide, T. Romashova, P. Alessandro, B. G. Wilson, C. W. M. Roberts, W. Hiddemann, D. M. Weinstock and O. Weigert (2014). "ARID1A Is Recurrently and Significantly Mutated in Follicular Lymphoma (FL) and Impairs DNA Repair Efficiency." *Blood* **124**(21): 73.
- Bararia, D., J. A. Hildebrand, S. Stolz, S. Haebe, S. Alig, C. P. Trevisani, F. Osorio-Barrios, M. D. Bartoschek, M. Mentz, A. Pastore, E. Gaitzsch, M. Heide, V. Jurinovic, K. Rautter, J. Gunawardana, M. B. Sabdia, M. Szczepanowski, J. Richter, W. Klapper, A. Louissaint, Jr., C. Ludwig, S. Bultmann, H. Leonhardt, S. Eustermann, K. P. Hopfner, W. Hiddemann, M. von Bergwelt-Baildon, C. Steidl, R. Kridel, J. W. D. Tobin, M. K. Gandhi, D. M. Weinstock, M. Schmidt-Suprian, M. B. Sárosi, M. Rudelius, V. Passerini, J. Mautner and O. Weigert (2020). "Cathepsin S Alterations Induce a Tumor-Promoting Immune Microenvironment in Follicular Lymphoma." *Cell Rep* **31**(5): 107522.
- Basso, K. and R. Dalla-Favera (2015). "Germinal centres and B cell lymphomagenesis." *Nat Rev Immunol* **15**(3): 172-184.
- Bendandi, M., C. D. Gocke, C. B. Kobrin, F. A. Benko, L. A. Sternas, R. Pennington, T. M. Watson, C. W. Reynolds, B. L. Gause, P. L. Duffey, E. S. Jaffe, S. P. Creekmore, D. L. Longo and L. W. Kwak (1999). "Complete molecular remissions induced by patient-specific vaccination plus granulocyte-monocyte colony-stimulating factor against lymphoma." *Nat Med* **5**(10): 1171-1177.
- Bilousova, G., A. Marusyk, C. C. Porter, R. D. Cardiff and J. DeGregori (2005). "Impaired DNA Replication within Progenitor Cell Pools Promotes Leukemogenesis." *PLOS Biology* **3**(12): e401.
- Birnbaum, D. J., J. Adélaïde, E. Mamessier, P. Finetti, A. Lagarde, G. Monges, F. Viret, A. Gonçalves, O. Turrini and J. R. Delpero (2011). "Genome profiling of pancreatic adenocarcinoma." *Genes, Chromosomes and Cancer* **50**(6): 456-465.
- Blümli, S., N. Wiechens, M. Y. Wu, V. Singh, M. Gierlinski, G. Schweikert, N. Gilbert, C. Naughton, R. Sundaramoorthy, J. Varghese, R. Gourlay, R. Soares, D. Clark and T. Owen-Hughes (2021). "Acute depletion of the ARID1A subunit of SWI/SNF complexes reveals distinct pathways for activation and repression of transcription." *Cell Rep* **37**(5): 109943.
- Budde, L. E., S. Assouline, L. H. Sehn, S. J. Schuster, S.-S. Yoon, D. H. Yoon, M. J. Matasar, F. Bosch, W. S. Kim, L. J. Nastoupil, I. W. Flinn, M. Shadman, C. Diefenbach, C. O'Hear, H. Huang, A. Kwan, C.-C. Li, E. C. Piccione, M. C. Wei, S. Yin and N. L. Bartlett (2022). "Single-Agent Mosunetuzumab Shows Durable Complete Responses in Patients With Relapsed or Refractory B-Cell Lymphomas: Phase I Dose-Escalation Study." *Journal of Clinical Oncology* **40**(5): 481-491.
- Burrell, R. A., S. E. McClelland, D. Endesfelder, P. Groth, M.-C. Weller, N. Shaikh, E. Domingo, N. Kanu, S. M. Dewhurst, E. Gronroos, S. K. Chew, A. J. Rowan, A. Schenk, M. Sheffer, M. Howell, M. Kschischo, A. Behrens, T. Helleday, J. Bartek, I. P. Tomlinson and C. Swanton (2013). "Replication stress links structural and numerical cancer chromosomal instability." *Nature* **494**(7438): 492-496.
- Butt, D., T. D. Chan, K. Bourne, J. R. Hermes, A. Nguyen, A. Statham, L. A. O'Reilly, A. Strasser, S. Price, P. Schofield, D. Christ, A. Basten, C. S. Ma, S. G. Tangye, T. G. Phan, V. K. Rao and R. Brink (2015). "FAS Inactivation Releases Unconventional Germinal Center B Cells that Escape Antigen Control and Drive IgE and Autoantibody Production." *Immunity* **42**(5): 890-902.

- Caeser, R., M. Di Re, J. A. Krupka, J. Gao, M. Lara-Chica, J. M. L. Dias, S. L. Cooke, R. Fenner, Z. Usheva, H. F. P. Runge, P. A. Beer, H. Eldaly, H. K. Pak, C. S. Park, G. S. Vassiliou, B. J. P. Huntly, A. Mupo, R. J. M. Bashford-Rogers and D. J. Hodson (2019). "Genetic modification of primary human B cells to model high-grade lymphoma." *Nat Commun* **10**(1): 4543.
- Caeser, R., J. Gao, M. Di Re, C. Gong and D. J. Hodson (2021). "Genetic manipulation and immortalized culture of ex vivo primary human germinal center B cells." *Nat Protoc* **16**(5): 2499-2519.
- Carbone, A., S. Roulland, A. Gloghini, A. Younes, G. von Keudell, A. López-Guillermo and J. Fitzgibbon (2019). "Follicular lymphoma." *Nat Rev Dis Primers* **5**(1): 83.
- Cherng, H.-J. J., R. Sun, B. Sugg, R. Irwin, H. Yang, C. C. Le, Q. Deng, L. Fayad, N. H. Fowler, S. Parmar, R. Steiner, F. Hagemester, R. Nair, H. J. Lee, M. Rodriguez, F. Samaniego, S. P. Iyer, C. R. Flowers, L. Wang, L. J. Nastoupil, S. S. Neelapu, S. Ahmed, P. Strati, M. R. Green and J. Westin (2022). "Risk assessment with low-pass whole-genome sequencing of cell-free DNA before CD19 CAR T-cell therapy for large B-cell lymphoma." *Blood* **140**(5): 504-515.
- Chuang, L. S., K. Ito and Y. Ito (2013). "RUNX family: Regulation and diversification of roles through interacting proteins." *Int J Cancer* **132**(6): 1260-1271.
- Chuang, L. S. and Y. Ito (2010). "RUNX3 is multifunctional in carcinogenesis of multiple solid tumors." *Oncogene* **29**(18): 2605-2615.
- Clapier, C. R., J. Iwasa, B. R. Cairns and C. L. Peterson (2017). "Mechanisms of action and regulation of ATP-dependent chromatin-remodelling complexes." *Nature Reviews Molecular Cell Biology* **18**(7): 407-422.
- Corces, M. R., A. E. Trevino, E. G. Hamilton, P. G. Greenside, N. A. Sinnott-Armstrong, S. Vesuna, A. T. Satpathy, A. J. Rubin, K. S. Montine, B. Wu, A. Kathiria, S. W. Cho, M. R. Mumbach, A. C. Carter, M. Kasowski, L. A. Orloff, V. I. Risca, A. Kundaje, P. A. Khavari, T. J. Montine, W. J. Greenleaf and H. Y. Chang (2017). "An improved ATAC-seq protocol reduces background and enables interrogation of frozen tissues." *Nat Methods* **14**(10): 959-962.
- Cox, J. and M. Mann (2008). "MaxQuant enables high peptide identification rates, individualized p.p.b.-range mass accuracies and proteome-wide protein quantification." *Nat Biotechnol* **26**(12): 1367-1372.
- Crouch, S., D. Painter, S. L. Barrans, E. Roman, P. A. Beer, S. L. Cooke, P. Glover, S. J. van Hoppe, N. Webster, S. E. Lacy, C. Ruiz, P. J. Campbell, D. J. Hodson, R. Patmore, C. Burton, A. Smith and R. M. Tooze (2022). "Molecular subclusters of follicular lymphoma: a report from the UK's Haematological Malignancy Research Network." *Blood Advances*.
- de Leval, L., A. A. Alizadeh, P. L. Bergsagel, E. Campo, A. Davies, A. Dogan, J. Fitzgibbon, S. M. Horwitz, A. M. Melnick, W. G. Morice, R. D. Morin, B. Nadel, S. A. Pileri, R. Rosenquist, D. Rossi, I. Salaverria, C. Steidl, S. P. Treon, A. D. Zelenetz, R. H. Advani, C. E. Allen, S. M. Ansell, W. C. Chan, J. R. Cook, L. B. Coe, F. d'Amore, S. Dirnhofer, M. Dreyling, K. Dunleavy, A. L. Feldman, F. Fend, P. Gaulard, P. Ghia, J. G. Gribben, O. Hermine, D. J. Hodson, E. D. Hsi, G. Inghirami, E. S. Jaffe, K. Karube, K. Kataoka, W. Klapper, W. S. Kim, R. L. King, Y. H. Ko, A. S. LaCasce, G. Lenz, J. I. Martin-Subero, M. A. Piris, S. Pittaluga, L. Pasqualucci, L. Quintanilla-Martinez, S. J. Rodig, A. Rosenwald, G. A. Salles, J. San-Miguel, K. J. Savage, L. H. Sehn, G. Semenzato, L. M. Staudt, S. H. Swerdlow, C. S. Tam, J. Trotman, J. M. Vose, O. Weigert, W. H. Wilson, J. N. Winter, C. J. Wu, P. L. Zinzani, E. Zucca, A. Bagg, D. W. Scott (2022). "Genomic profiling for clinical decision making in lymphoid neoplasms." *Blood*. **140**(21):2193-2227.
- Dobaño-López, C., F. Araujo-Ayala, N. Serrat, J. G. Valero and P. Pérez-Galán (2021). "Follicular Lymphoma Microenvironment: An Intricate Network Ready for Therapeutic Intervention." *Cancers* **13**(4): 641.
- Dobin, A., C. A. Davis, F. Schlesinger, J. Drenkow, C. Zaleski, S. Jha, P. Batut, M. Chaisson and T. R. Gingeras (2012). "STAR: ultrafast universal RNA-seq aligner." *Bioinformatics* **29**(1): 15-21.
- Dreyling, M., M. Ghielmini, S. Rule, G. Salles, M. Ladetto, S. H. Tonino, K. Herfarth, J. F. Seymour and M. Jerkeman (2021). "Newly diagnosed and relapsed follicular lymphoma: ESMO Clinical Practice Guidelines for diagnosis, treatment and follow-up." *Ann Oncol* **32**(3): 298-308.

- Dreyling, M., M. Ghielmini, S. Rule, G. Salles, U. Vitolo and M. Ladetto (2016). "Newly diagnosed and relapsed follicular lymphoma: ESMO Clinical Practice Guidelines for diagnosis, treatment and follow-up." *Ann Oncol* **27**(suppl 5): v83-v90.
- Fowler, N. H., M. Dickinson, M. Dreyling, J. Martinez-Lopez, A. Kolstad, J. Butler, M. Ghosh, L. Popplewell, J. C. Chavez, E. Bachy, K. Kato, H. Harigae, M. J. Kersten, C. Andreadis, P. A. Riedell, P. J. Ho, J. A. Pérez-Simón, A. I. Chen, L. J. Nastoupil, B. von Tresckow, A. J. M. Ferreri, T. Teshima, P. E. M. Patten, J. P. McGuirk, A. L. Petzer, F. Offner, A. Viardot, P. L. Zinzani, R. Malladi, A. Zia, R. Awasthi, A. Masood, O. Anak, S. J. Schuster and C. Thieblemont (2022). "Tisagenlecleucel in adult relapsed or refractory follicular lymphoma: the phase 2 ELARA trial." *Nat Med* **28**(2): 325-332.
- Fujii, S., K. Ito, Y. Ito and A. Ochiai (2008). "Enhancer of zeste homologue 2 (EZH2) down-regulates RUNX3 by increasing histone H3 methylation." *J Biol Chem* **283**(25): 17324-17332.
- Fujimoto, A., Y. Totoki, T. Abe, K. A. Boroevich, F. Hosoda, H. H. Nguyen, M. Aoki, N. Hosono, M. Kubo and F. Miya (2012). "Whole-genome sequencing of liver cancers identifies etiological influences on mutation patterns and recurrent mutations in chromatin regulators." *Nature genetics* **44**(7): 760-764.
- Gascoyne, R. D., B. Nadel, L. Pasqualucci, J. Fitzgibbon, J. E. Payton, A. Melnick, O. Weigert, K. Tarte, J. G. Gribben and J. W. Friedberg (2017). "Follicular lymphoma: State-of-the-art ICML workshop in Lugano 2015." *Hematological Oncology* **35**(4): 397-407.
- Gessulat, S., T. Schmidt, D. P. Zolg, P. Samaras, K. Schnatbaum, J. Zerweck, T. Knaute, J. Rechenberger, B. Delanghe, A. Huhmer, U. Reimer, H. C. Ehrlich, S. Aiche, B. Kuster and M. Wilhelm (2019). "Prosit: proteome-wide prediction of peptide tandem mass spectra by deep learning." *Nat Methods* **16**(6): 509-518.
- Godfried, M. B., M. Veenstra, A. Valent, P. v. Sluis, P. A. Voûte, R. Versteeg and H. N. Caron (2002). "Lack of interstitial chromosome 1p deletions in clinically-detected neuroblastoma." *European Journal of Cancer* **38**(11): 1513-1519.
- Golstein, P. and G. M. Griffiths (2018). "An early history of T cell-mediated cytotoxicity." *Nat Rev Immunol* **18**(8): 527-535.
- Green, M. R., A. J. Gentles, R. V. Nair, J. M. Irish, S. Kihira, C. L. Liu, I. Kela, E. S. Hopmans, J. H. Myklebust, H. Ji, S. K. Plevritis, R. Levy and A. A. Alizadeh (2013). "Hierarchy in somatic mutations arising during genomic evolution and progression of follicular lymphoma." *Blood* **121**(9): 1604-1611.
- Gruen, M., K. Bommert and R. C. Bargou (2004). "T-cell-mediated lysis of B cells induced by a CD19xCD3 bispecific single-chain antibody is perforin dependent and death receptor independent." *Cancer Immunol Immunother* **53**(7): 625-632.
- Guichard, C., G. Amaddeo, S. Imbeaud, Y. Ladeiro, L. Pelletier, I. B. Maad, J. Calderaro, P. Bioulac-Sage, M. Letexier and F. Degos (2012). "Integrated analysis of somatic mutations and focal copy-number changes identifies key genes and pathways in hepatocellular carcinoma." *Nature genetics* **44**(6): 694-698.
- Haas, C., E. Krinner, K. Brischwein, P. Hoffmann, R. Lutterbüse, B. Schlereth, P. Kufer and P. A. Baeuerle (2009). "Mode of cytotoxic action of T cell-engaging BiTE antibody MT110." *Immunobiology* **214**(6): 441-453.
- Haebe, S., W. Keay, S. Alig, A. W. Mohr, L. K. Martin, M. Heide, R. Secci, S. Krebs, H. Blum, A. Moosmann, A. Louissaint, Jr., D. M. Weinstock, S. Thoene, M. von Bergwelt-Baildon, J. Ruland, D. Bararia and O. Weigert (2022). "The molecular ontogeny of follicular lymphoma: gene mutations succeeding the BCL2 translocation define common precursor cells." *Br J Haematol* **196**(6): 1381-1387.
- Hao, Z., G. S. Duncan, J. Seagal, Y. W. Su, C. Hong, J. Haight, N. J. Chen, A. Elia, A. Wakeham, W. Y. Li, J. Liepa, G. A. Wood, S. Casola, K. Rajewsky and T. W. Mak (2008). "Fas receptor expression in germinal-center B cells is essential for T and B lymphocyte homeostasis." *Immunity* **29**(4): 615-627.
- Hollenhorst, P. C., K. J. Chandler, R. L. Poulsen, W. E. Johnson, N. A. Speck and B. J. Graves (2009). "DNA Specificity Determinants Associate with Distinct Transcription Factor Functions." *PLOS Genetics* **5**(12): e1000778.

- Hollenhorst, P. C., A. A. Shah, C. Hopkins and B. J. Graves (2007). "Genome-wide analyses reveal properties of redundant and specific promoter occupancy within the ETS gene family." *Genes & development* **21**(15): 1882-1894.
- Huang, J., Q. Deng, Q. Wang, K.-Y. Li, J.-H. Dai, N. Li, Z.-D. Zhu, B. Zhou, X.-Y. Liu and R.-F. Liu (2012). "Exome sequencing of hepatitis B virus-associated hepatocellular carcinoma." *Nature genetics* **44**(10): 1117-1121.
- Hughes, C. S., S. Moggridge, T. Müller, P. H. Sorensen, G. B. Morin and J. Krijgsveld (2019). "Single-pot, solid-phase-enhanced sample preparation for proteomics experiments." *Nat Protoc* **14**(1): 68-85.
- Hutchings, M., F. Morschhauser, G. Iacoboni, C. Carlo-Stella, F. C. Offner, A. Sureda, G. Salles, J. Martínez-Lopez, M. Crump, D. N. Thomas, P. N. Morcos, C. Ferlini, A.-M. E. Bröske, A. Belousov, M. Bacac, N. Dimier, D. J. Carlile, L. Lundberg, D. Perez-Callejo, P. Umaña, T. Moore, M. Weisser and M. J. Dickinson (2021). "Glofitamab, a Novel, Bivalent CD20-Targeting T-Cell-Engaging Bispecific Antibody, Induces Durable Complete Remissions in Relapsed or Refractory B-Cell Lymphoma: A Phase I Trial." *Journal of Clinical Oncology* **39**(18): 1959-1970.
- Ibarra, I. L., N. M. Hollmann, B. Klaus, S. Augsten, B. Velten, J. Hennig and J. B. Zaugg (2020). "Mechanistic insights into transcription factor cooperativity and its impact on protein-phenotype interactions." *Nature Communications* **11**(1): 124.
- Jacobson, C. A., J. C. Chavez, A. R. Sehgal, B. M. William, J. Munoz, G. Salles, P. N. Munshi, C. Casulo, D. G. Maloney, S. de Vos, R. Reshef, L. A. Leslie, I. Yakoub-Agha, O. O. Oluwole, H. C. H. Fung, J. Rosenblatt, J. M. Rossi, L. Goyal, V. Plaks, Y. Yang, R. Vezan, M. P. Avanzi and S. S. Neelapu (2022). "Axicabtagene ciloleucel in relapsed or refractory indolent non-Hodgkin lymphoma (ZUMA-5): a single-arm, multicentre, phase 2 trial." *Lancet Oncol* **23**(1): 91-103.
- Janjic, A., L. E. Wange, J. W. Bagnoli, J. Geuder, P. Nguyen, D. Richter, B. Vieth, B. Vick, I. Jeremias, C. Ziegenhain, I. Hellmann and W. Enard (2021). "Prime-seq, efficient and powerful bulk RNA-sequencing." *bioRxiv*: 2021.2009.2027.459575.
- Jiang, T., X. Chen, C. Su, S. Ren and C. Zhou (2020). "Pan-cancer analysis of ARID1A Alterations as Biomarkers for Immunotherapy Outcomes." *J Cancer* **11**(4): 776-780.
- Jones, S., M. Li, D. W. Parsons, X. Zhang, J. Wesseling, P. Kristel, M. K. Schmidt, S. Markowitz, H. Yan and D. Bigner (2012). "Somatic mutations in the chromatin remodeling gene ARID1A occur in several tumor types." *Human mutation* **33**(1): 100-103.
- Jones, S., T. L. Wang, M. Shih Ie, T. L. Mao, K. Nakayama, R. Roden, R. Glas, D. Slamon, L. A. Diaz, Jr., B. Vogelstein, K. W. Kinzler, V. E. Velculescu and N. Papadopoulos (2010). "Frequent mutations of chromatin remodeling gene ARID1A in ovarian clear cell carcinoma." *Science* **330**(6001): 228-231.
- Kadoch, C. and G. R. Crabtree (2015). "Mammalian SWI/SNF chromatin remodeling complexes and cancer: Mechanistic insights gained from human genomics." *Sci Adv* **1**(5): e1500447.
- Kadoch, C., D. C. Hargreaves, C. Hodges, L. Elias, L. Ho, J. Ranish and G. R. Crabtree (2013). "Proteomic and bioinformatic analysis of mammalian SWI/SNF complexes identifies extensive roles in human malignancy." *Nat Genet* **45**(6): 592-601.
- Kasahara, K., M. Shiina, I. Fukuda, K. Ogata and H. Nakamura (2017). "Molecular mechanisms of cooperative binding of transcription factors Runx1-CBF β -Ets1 on the TCR α gene enhancer." *PLoS one* **12**(2): e0172654.
- Katagiri, A., K. Nakayama, M. T. Rahman, M. Rahman, H. Katagiri, N. Nakayama, M. Ishikawa, T. Ishibashi, K. Iida, H. Kobayashi, Y. Otsuki, S. Nakayama and K. Miyazaki (2012). "Loss of ARID1A expression is related to shorter progression-free survival and chemoresistance in ovarian clear cell carcinoma." *Mod Pathol* **25**(2): 282-288.
- Kennison, J. A. and J. W. Tamkun (1988). "Dosage-dependent modifiers of polycomb and antennapedia mutations in *Drosophila*." *Proc Natl Acad Sci U S A* **85**(21): 8136-8140.
- Korfi, K., S. Ali, J. A. Heward and J. Fitzgibbon (2017). "Follicular lymphoma, a B cell malignancy addicted to epigenetic mutations." *Epigenetics* **12**(5): 370-377.
- Kridel, R., L. H. Sehn and R. D. Gascoyne (2012). "Pathogenesis of follicular lymphoma." *J Clin Invest* **122**(10): 3424-3431.

- Kumar, E., L. Pickard and J. Okosun (2021). "Pathogenesis of follicular lymphoma: genetics to the microenvironment to clinical translation." *British Journal of Haematology* **194**(5): 810-821.
- Kwak, L. W., M. J. Campbell, D. K. Czerwinski, S. Hart, R. A. Miller and R. Levy (1992). "Induction of immune responses in patients with B-cell lymphoma against the surface-immunoglobulin idiotype expressed by their tumors." *N Engl J Med* **327**(17): 1209-1215.
- Lee, Y. M. (2011). "Control of RUNX3 by histone methyltransferases." *J Cell Biochem* **112**(2): 394-400.
- Luger, K., & Richmond, T.J. (1998). "DNA binding within the nucleosome core." *Current opinion in structural biology* **8**(1): 33-40.
- Luo, B., H. W. Cheung, A. Subramanian, T. Sharifnia, M. Okamoto, X. Yang, G. Hinkle, J. S. Boehm, R. Beroukhi, B. A. Weir, C. Mermel, D. A. Barbie, T. Awad, X. Zhou, T. Nguyen, B. Piquani, C. Li, T. R. Golub, M. Meyerson, N. Hacohen, W. C. Hahn, E. S. Lander, D. M. Sabatini and D. E. Root (2008). "Highly parallel identification of essential genes in cancer cells." *Proc Natl Acad Sci U S A* **105**(51): 20380-20385.
- MacLean, B., D. M. Tomazela, N. Shulman, M. Chambers, G. L. Finney, B. Frewen, R. Kern, D. L. Tabb, D. C. Liebler and M. J. MacCoss (2010). "Skyline: an open source document editor for creating and analyzing targeted proteomics experiments." *Bioinformatics* **26**(7): 966-968.
- Makaryan, S. Z. and S. D. Finley (2020). "An optimal control approach for enhancing natural killer cells' secretion of cytolytic molecules." *APL Bioeng* **4**(4): 046107.
- Mamo, A., L. Cavallone, S. Tuzmen, C. Chabot, C. Ferrario, S. Hassan, H. Edgren, O. Kallioniemi, O. Aleynikova and E. Przybytkowski (2012). "An integrated genomic approach identifies ARID1A as a candidate tumor-suppressor gene in breast cancer." *Oncogene* **31**(16): 2090-2100.
- Manandhar, S. and Y. M. Lee (2018). "Emerging role of RUNX3 in the regulation of tumor microenvironment." *BMB Rep* **51**(4): 174-181.
- Mathur, R. (2018). "ARID1A loss in cancer: Towards a mechanistic understanding." *Pharmacol Ther* **190**: 15-23.
- Morgunova, E. and J. Taipale (2017). "Structural perspective of cooperative transcription factor binding." *Curr Opin Struct Biol* **47**: 1-8.
- Moriarty, R. A., S. Mili and K. M. Stroka (2022). "RNA localization in confined cells depends on cellular mechanical activity and contributes to confined migration." *iScience* **25**(2).
- Morin, R. D., M. Mendez-Lago, A. J. Mungall, R. Goya, K. L. Mungall, R. D. Corbett, N. A. Johnson, T. M. Severson, R. Chiu, M. Field, S. Jackman, M. Krzywinski, D. W. Scott, D. L. Trinh, J. Tamura-Wells, S. Li, M. R. Firme, S. Rogic, M. Griffith, S. Chan, O. Yakovenko, I. M. Meyer, E. Y. Zhao, D. Smailus, M. Moks, S. Chittaranjan, L. Rimsza, A. Brooks-Wilson, J. J. Spinelli, S. Ben-Neriah, B. Meissner, B. Woolcock, M. Boyle, H. McDonald, A. Tam, Y. Zhao, A. Delaney, T. Zeng, K. Tse, Y. Butterfield, I. Birol, R. Holt, J. Schein, D. E. Horsman, R. Moore, S. J. M. Jones, J. M. Connors, M. Hirst, R. D. Gascoyne and M. A. Marra (2011). "Frequent mutation of histone-modifying genes in non-Hodgkin lymphoma." *Nature* **476**(7360): 298-303.
- Mounier, M., N. Bossard, L. Remontet, A. Belot, P. Minicozzi, R. De Angelis, R. Capocaccia, J. Iwaz, A. Monnereau, X. Troussard, M. Sant, M. Maynadié and R. Giorgi (2015). "Changes in dynamics of excess mortality rates and net survival after diagnosis of follicular lymphoma or diffuse large B-cell lymphoma: comparison between European population-based data (EUROCare-5)." *Lancet Haematol* **2**(11): e481-491.
- Mulder, T. A., B. E. Wahlin, A. Österborg and M. Palma (2019). "Targeting the Immune Microenvironment in Lymphomas of B-Cell Origin: From Biology to Clinical Application." *Cancers* **11**(7): 915.
- Mullen, J., S. Kato, J. K. Sicklick and R. Kurzrock (2021). "Targeting *ARID1A* mutations in cancer." *Cancer Treatment Reviews* **100**.
- Nastoupil, L., R. Sinha, A. Hirschey and C. R. Flowers (2012). "Considerations in the initial management of follicular lymphoma." *Community Oncol* **9**(11): S53-s60.
- Neigeborn, L. and M. Carlson (1984). "Genes affecting the regulation of SUC2 gene expression by glucose repression in *Saccharomyces cerevisiae*." *Genetics* **108**(4): 845-858.

- Okosun, J., C. Bödör, J. Wang, S. Araf, C. Y. Yang, C. Pan, S. Boller, D. Cittaro, M. Bozek, S. Iqbal, J. Matthews, D. Wrench, J. Marzec, K. Tawana, N. Popov, C. O'Riain, D. O'Shea, E. Carlotti, A. Davies, C. H. Lawrie, A. Matolcsy, M. Calaminici, A. Norton, R. J. Byers, C. Mein, E. Stupka, T. A. Lister, G. Lenz, S. Montoto, J. G. Gribben, Y. Fan, R. Grosschedl, C. Chelala and J. Fitzgibbon (2014). "Integrated genomic analysis identifies recurrent mutations and evolution patterns driving the initiation and progression of follicular lymphoma." *Nat Genet* **46**(2): 176-181.
- Otto, O., P. Rosendahl, A. Mietke, S. Golfier, C. Herold, D. Klaue, S. Girardo, S. Pagliara, A. Ekpenyong, A. Jacobi, M. Wobus, N. Töpfner, U. F. Keyser, J. Mansfeld, E. Fischer-Friedrich and J. Guck (2015). "Real-time deformability cytometry: on-the-fly cell mechanical phenotyping." *Nat Methods* **12**(3): 199-202, 194 p following 202.
- Parekh, S., C. Ziegenhain, B. Vieth, W. Enard and I. Hellmann (2018). "zUMIs - A fast and flexible pipeline to process RNA sequencing data with UMIs." *GigaScience* **7**(6).
- Pastore, A., V. Jurinovic, R. Kridel, E. Hoster, A. M. Staiger, M. Szczepanowski, C. Pott, N. Kopp, M. Murakami, H. Horn, E. Leich, A. A. Moccia, A. Mottok, A. Sunkavalli, P. Van Hummelen, M. Ducar, D. Ennishi, H. P. Shulha, C. Hother, J. M. Connors, L. H. Sehn, M. Dreyling, D. Neuberg, P. Möller, A. C. Feller, M. L. Hansmann, H. Stein, A. Rosenwald, G. Ott, W. Klapper, M. Unterhalt, W. Hiddemann, R. D. Gascoyne, D. M. Weinstock and O. Weigert (2015). "Integration of gene mutations in risk prognostication for patients receiving first-line immunochemotherapy for follicular lymphoma: a retrospective analysis of a prospective clinical trial and validation in a population-based registry." *Lancet Oncol* **16**(9): 1111-1122.
- Pavlidou, E. N. and V. Balis (2020). "Diagnostic significance and prognostic role of the ARID1A gene in cancer outcomes (Review)." *World Acad Sci J* **2**(2): 49-64.
- Perrett, M. and J. Okosun (2021). "Genetic heterogeneity in follicular lymphoma." *Annals of Lymphoma* **5**.
- Peter, M. E., A. Hadji, A. E. Murmann, S. Brockway, W. Putzbach, A. Pattanayak and P. Ceppi (2015). "The role of CD95 and CD95 ligand in cancer." *Cell Death & Differentiation* **22**(4): 549-559.
- Poetsch, M., T. Dittberner and C. Woenckhaus (2003). "Microsatellite analysis at 1p36.3 in malignant melanoma of the skin: fine mapping in search of a possible tumour suppressor gene region." *Melanoma Res* **13**(1): 29-33.
- Ramsay, A. G., A. J. Clear, G. Kelly, R. Fatah, J. Matthews, F. Macdougall, T. A. Lister, A. M. Lee, M. Calaminici and J. G. Gribben (2009). "Follicular lymphoma cells induce T-cell immunologic synapse dysfunction that can be repaired with lenalidomide: implications for the tumor microenvironment and immunotherapy." *Blood* **114**(21): 4713-4720.
- Ran, F. A., P. D. Hsu, J. Wright, V. Agarwala, D. A. Scott and F. Zhang (2013). "Genome engineering using the CRISPR-Cas9 system." *Nat Protoc* **8**(11): 2281-2308.
- Razzaghi, R., S. Agarwal, N. Kotlov, O. Plotnikova, K. Nomie, D. W. Huang, G. W. Wright, G. A. Smith, M. Li, K. Takata, M. Yamada, C. Yao, J. J. O'Shea, J. D. Phelan, S. Pittaluga, D. W. Scott and J. R. Muppidi (2020). "Compromised counterselection by FAS creates an aggressive subtype of germinal center lymphoma." *Journal of Experimental Medicine* **218**(3).
- Redfern, C. H., T. H. Guthrie, A. Bessudo, J. J. Densmore, P. R. Holman, N. Janakiraman, J. P. Leonard, R. L. Levy, R. G. Just, M. R. Smith, F. P. Rosenfelt, P. H. Wiernik, W. D. Carter, D. P. Gold, T. J. Melink, J. C. Gutheil and J. F. Bender (2006). "Phase II trial of idiotype vaccination in previously treated patients with indolent non-Hodgkin's lymphoma resulting in durable clinical responses." *J Clin Oncol* **24**(19): 3107-3112.
- Roulland, S., M. Faroudi, E. Mamessier, S. Sungalee, G. Salles and B. Nadel (2011). "Early steps of follicular lymphoma pathogenesis." *Adv Immunol* **111**: 1-46.
- Shain, A. H., C. P. Giacomini, K. Matsukuma, C. A. Karikari, M. D. Bashyam, M. Hidalgo, A. Maitra and J. R. Pollack (2012). "Convergent structural alterations define SWI/SNF/Sucrose NonFermentable (SWI/SNF) chromatin remodeler as a central tumor suppressive complex in pancreatic cancer." *Proceedings of the National Academy of Sciences* **109**(5): E252-E259.
- Shen, J., Y. Peng, L. Wei, W. Zhang, L. Yang, L. Lan, P. Kapoor, Z. Ju, Q. Mo, M. Shih le, I. P. Uray, X. Wu, P. H. Brown, X. Shen, G. B. Mills and G. Peng (2015). "ARID1A Deficiency Impairs

- the DNA Damage Checkpoint and Sensitizes Cells to PARP Inhibitors." *Cancer Discov* **5**(7): 752-767.
- Shevchenko, A., H. Tomas, J. Havlis, J. V. Olsen and M. Mann (2006). "In-gel digestion for mass spectrometric characterization of proteins and proteomes." *Nat Protoc* **1**(6): 2856-2860.
- Solovey, M. and A. Scialdone (2020). "COMUNET: a tool to explore and visualize intercellular communication." *Bioinformatics* **36**(15): 4296-4300.
- Stern, M., Jensen, R., Herskowitz, I. (1984). "Five SWI genes are required for expression of the HO gene in yeast." *Journal of Molecular Biology* **178**(4): 853-868.
- Strobl, C. D. (2022). "Inhibition of human CD8+ T cells by the tumor metabolite methylthioadenosine: Mechanisms of action and putative strategies to improve antitumor activity" [Doctoral Dissertation, Friedrich-Alexander-Universität Erlangen-Nürnberg (FAU)].
urn:nbn:de:bvb:29-opus4-182550
- Sun, X., S. C. Wang, Y. Wei, X. Luo, Y. Jia, L. Li, P. Gopal, M. Zhu, I. Nassour and J.-C. Chuang (2017). "Arid1a has context-dependent oncogenic and tumor suppressor functions in liver cancer." *Cancer cell* **32**(5): 574-589. e576.
- Takahashi, Y., H. Ohta and T. Takemori (2001). "Fas is required for clonal selection in germinal centers and the subsequent establishment of the memory B cell repertoire." *Immunity* **14**(2): 181-192.
- Tay, R. E., E. K. Richardson and H. C. Toh (2021). "Revisiting the role of CD4+ T cells in cancer immunotherapy—new insights into old paradigms." *Cancer Gene Therapy* **28**(1): 5-17.
- Thurman, R. E., Rynes, E., Humbert, R., Vierstra, J., Maurano, M. T., Haugen, E., Sheffield, N. C., Stergachis, A. B., Wang, H., Vernot, B., Garg, K., John, S., Sandstrom, R., Bates, D., Boatman, L., Canfield, T. K., Diegel, M., Dunn, D., Ebersol, A. K., Frum, T., ... Stamatoyannopoulos, J. A. (2012). "The accessible chromatin landscape of the human genome." *Nature*, **489**(7414), 75–82.
- Tobin, J. W. D., C. Keane, J. Gunawardana, P. Mollee, S. Birch, T. Hoang, J. Lee, L. Li, L. Huang, V. Murigneux, J. L. Fink, N. Matigian, F. Vari, S. Francis, R. Kridel, O. Weigert, S. Haebe, V. Jurinovic, W. Klapper, C. Steidl, L. H. Sehn, S.-C. Law, M. N. Wykes and M. K. Gandhi (2019). "Progression of Disease Within 24 Months in Follicular Lymphoma Is Associated With Reduced Intratumoral Immune Infiltration." *Journal of Clinical Oncology* **37**(34): 3300-3309.
- Tomihara, H., F. Carbone, L. Perelli, J. K. Huang, M. Soeung, J. L. Rose, F. S. Robinson, Y. Lissanu Deribe, N. Feng, M. Takeda, A. Inoue, E. D. Poggetto, A. K. Deem, A. Maitra, P. Msaouel, N. M. Tannir, G. F. Draetta, A. Viale, T. P. Heffernan, C. A. Bristow, A. Carugo and G. Genovese (2021). "Loss of ARID1A Promotes Epithelial-Mesenchymal Transition and Sensitizes Pancreatic Tumors to Proteotoxic Stress." *Cancer Res* **81**(2): 332-343.
- Totten, S., D. Gaucher, R. D. Morin, S. Assouline, J. M. Connors, M. A. Marra, D. W. Scott, R. D. Gascoyne, J. Pelletier, K. K. Mann and N. Johnson (2014). "FAS Mutations Accelerate Lymphoma Growth and Induce Therapeutic Resistance." *Blood* **124**(21): 3018-3018.
- Tsujimoto, Y., J. Cossman, E. Jaffe and C. M. Croce (1985). "Involvement of the bcl-2 gene in human follicular lymphoma." *Science* **228**(4706): 1440-1443.
- Upadhyay, R., J. A. Boiarsky, G. Pantsulaia, J. Svensson-Arelund, M. J. Lin, A. Wroblewska, S. Bhalla, N. Scholler, A. Bot, J. M. Rossi, N. Sadek, S. Parekh, A. Lagana, A. Baccarini, M. Merad, B. D. Brown and J. D. Brody (2021). "A Critical Role for Fas-Mediated Off-Target Tumor Killing in T-cell Immunotherapy." *Cancer Discov* **11**(3): 599-613.
- Victoria, G. D., D. Dominguez-Sola, A. B. Holmes, S. Deroubaix, R. Dalla-Favera and M. C. Nussenzweig (2012). "Identification of human germinal center light and dark zone cells and their relationship to human B-cell lymphomas." *Blood* **120**(11): 2240-2248.
- Wang, K., J. Kan, S. T. Yuen, S. T. Shi, K. M. Chu, S. Law, T. L. Chan, Z. Kan, A. S. Chan and W. Y. Tsui (2011). "Exome sequencing identifies frequent mutation of ARID1A in molecular subtypes of gastric cancer." *Nature genetics* **43**(12): 1219-1223.
- Wang, M., H. Jiang, X. Liu and X. Wang (2022). "Biophysics involved in the process of tumor immune escape." *iScience* **25**(4).

- Weigert, O., N. Kopp, A. A. Lane, A. Yoda, S. E. Dahlberg, D. Neuberg, A. Y. Bahar, B. Chapuy, J. L. Kutok, J. A. Longtine, F. C. Kuo, T. Haley, M. Salois, T. J. Sullivan, D. C. Fisher, E. A. Fox, S. J. Rodig, J. H. Antin and D. M. Weinstock (2012). "Molecular ontogeny of donor-derived follicular lymphomas occurring after hematopoietic cell transplantation." *Cancer Discov* **2**(1): 47-55.
- Weigert, O. and D. M. Weinstock (2017). "The promises and challenges of using gene mutations for patient stratification in follicular lymphoma." *Blood* **130**(13): 1491-1498.
- Werner, H. M., A. Berg, E. Wik, E. Birkeland, C. Krakstad, K. Kusonmano, K. Petersen, K. H. Kalland, A. M. Oyan, L. A. Akhlen, J. Trovik and H. B. Salvesen (2013). "ARID1A loss is prevalent in endometrial hyperplasia with atypia and low-grade endometrioid carcinomas." *Mod Pathol* **26**(3): 428-434.
- Wiegand, K. C., A. F. Lee, O. M. Al-Agha, C. Chow, S. E. Kalloger, D. W. Scott, C. Steidl, S. M. Wiseman, R. D. Gascoyne, B. Gilks and D. G. Huntsman (2011). "Loss of BAF250a (ARID1A) is frequent in high-grade endometrial carcinomas." *The Journal of Pathology* **224**(3): 328-333.
- Wilson, B. G. and C. W. Roberts (2011). "SWI/SNF nucleosome remodellers and cancer." *Nat Rev Cancer* **11**(7): 481-492.
- Wu, J. N. and C. W. Roberts (2013). "ARID1A mutations in cancer: another epigenetic tumor suppressor?" *Cancer Discov* **3**(1): 35-43.
- Wu, R. C., T. L. Wang and M. Shih le (2014). "The emerging roles of ARID1A in tumor suppression." *Cancer Biol Ther* **15**(6): 655-664.
- Yunis, J. J., M. M. Oken, M. E. Kaplan, K. M. Ensrud, R. R. Howe and A. Theologides (1982). "Distinctive chromosomal abnormalities in histologic subtypes of non-Hodgkin's lymphoma." *N Engl J Med* **307**(20): 1231-1236.
- Zang, Z. J., I. Cutcutache, S. L. Poon, S. L. Zhang, J. R. McPherson, J. Tao, V. Rajasegaran, H. L. Heng, N. Deng and A. Gan (2012). "Exome sequencing of gastric adenocarcinoma identifies recurrent somatic mutations in cell adhesion and chromatin remodeling genes." *Nature genetics* **44**(5): 570-574.
- Zoellner, A., K. Herfarth, M. Herold, W. Klapper, N. Skoetz and W. Hiddemann (2021). "Clinical Practice Guideline: Follicular Lymphoma—Diagnosis, Treatment, and Follow-up." *Dtsch Arztebl Int* **118**(Forthcoming): 320-325.
- Zolg, D. P., M. Wilhelm, P. Yu, T. Knaute, J. Zerweck, H. Wenschuh, U. Reimer, K. Schnatbaum and B. Kuster (2017). "PROCAL: A Set of 40 Peptide Standards for Retention Time Indexing, Column Performance Monitoring, and Collision Energy Calibration." *Proteomics* **17**(21).

Acknowledgments

I left the acknowledgments as the last part of the thesis to be written, thinking that they were an “easy” task, but... I was wrong. The very complicated spelling of the word itself should have warned me.

While writing these words, I am overwhelmed by all the memories and events that happened during these nearly four years of my life that made it memorable. Mainly because of the wonderful people who were part of it and will keep being part of it.

When I first started my Ph.D. journey, I was told that it would not be easy and that it would be full of obstacles to overcome. Of course, it was true. Nevertheless, thanks to my discipline and commitment and the people who accompanied and guided me, the Ph.D. was an incredible time.

Let's start this acknowledgment round without dwelling.

First, I want to thank my Doktorvater, Oliver Weigert, for believing in me as a Ph.D. candidate and as a person. Thank you for your guidance and support during these years and for pushing me to work on my weakness and become a better scientist. Thanks, because your door was always open! You constantly inspired me with your passion for medical scientific research, enthusiasm and determination.

A big fat thank you to the AG Weigert, you are all unique! Verena, Will, and Johannes, you were with me from day #1 and welcomed me into the group. Verena, you are an important point of reference for me. As mentioned, from the beginning, you have (and still do) helped and encouraged me, Thanks. Thank you, Will and Johannes, you two are my buddies on this journey... we shared daily our successes, concerns, crazy ideas, plans, and wishes, deep and honest (maybe sometimes too honest) talks in the cell culture... and we got till here together! Thank you, Caro; work-wise, you opened everyone's eyes to the FACS wonderland and always had the big picture in mind. Out-of-Lab, you are my craziest sports partner, the best party organizer ever, and a cheerful person. Thank you, Louisa, for sharing your medical expertise and answering all my questions, which scaled up drastically during the thesis writing. Also, thanks for always drinking with me... the early morning coffees and... the after-work Spritz. Thanks, Pranav, for being caring and kind, for giving us the boulder- β , and for all your funny jokes, memes and videos. Thank you, Lukas; even if we shared a short time in the lab, I really enjoyed working with you. Thanks for always taking the time to have lunch together, even though I was actually the only one of us having lunch. Thanks, Quentin, for the time we shared during and outside work, the laughs, the Bachelor Bingo, your colorful/funny socks, and all the “drama” that made every day unique. Thank you, Micha, for teaching me many wet-lab techniques, your cooperation in the project, and the excellent coffee you constantly provided!

Thanks ELLFen, for the pleasant work environment, the fun Christmas parties, and the summer barbeques. I particularly thank Alessandra for always being ready to listen to me, and I thank Yana for teaching me to be more spontaneous and for the great time we had together.

Moreover, I want to thank Maria S. Thank you for being a great collaborator and a brilliant scientist, for sharing the uphill path of writing a paper and improving the quality of our work.

Out of work, I have to thank many people that have been with me during this journey and contributed to making it even more special. I want to thank my “besties” for a lifetime, Bea, Michi, and Madda; thanks for always shouldering me, even now that we are in four different countries. Thank you, Viola and Troy; since I moved here, you have become an essential part of my life, I am very

thankful for every activity that we shared, and we will share. Thank you, Gió, for being a constant presence and for your dreamer soul. Thank you, Joel, Jenny, Lisa, Daniel, and Chris. You have been among the first ones that I connected with during my time in Munich, thank you for making me feel welcomed and offering me your friendship.

Thank you, Ale. There is not much else to add to these few words, also because I know that you do not like romantic sentences and would find them awkward. Thanks for encouraging me to move to Munich, even though it meant being 500 km apart from each other for a few years. I am glad that now we are here together.

Finally, thanks to my family for their unconditional love and support. Desidero ringraziare i miei nonni perché quotidianamente mi fate sentire amata, importante e come se stessi facendo qualcosa di grande, anche nel mio piccolo. Grazie a Voi, la mia ineguagliabile famiglia, che mi amate e sostenete da sempre. Grazie perché fin dal primo momento che ho scelto di vivere lontana, mi avete incoraggiata e spronata, anche se per voi non è stato facile. Mi avete insegnato a combattere per le persone e le cose cui tengo, a non demordere ed essere fedele a me stessa. Siete sempre stati e sempre sarete la mia forza e farò.

Affidavit



Affidavit

Antoniolli, Martina

Surname, first name

Max-Lebsche-Platz 30

Street

81373, München, Deutschland

Zip code, town, country

I hereby declare, that the submitted thesis entitled:

Functional Characterization of ARID1A Mutations in Follicular Lymphoma

is my own work. I have only used the sources indicated and have not made unauthorised use of services of a third party. Where the work of others has been quoted or reproduced, the source is always given.

I further declare that the dissertation presented here has not been submitted in the same or similar form to any other institution for the purpose of obtaining an academic degree.

München, 04.10.2023

place, date

Martina Antoniolli

Signature doctoral candidate

Confirmation of congruency



**Confirmation of congruency between printed and electronic version of
the doctoral thesis**

Antoniolli, Martina

Surname, first name

Max-Lebsche-Platz 30

Street

81373, München, Deutschland

Zip code, town, country

I hereby declare, that the submitted thesis entitled:

Functional Characterization of ARID1A Mutations in Follicular Lymphoma

is congruent with the printed version both in content and format.

München, 04.10.2023
place, date

Martina Antonioli
Signature doctoral candidate

List of publications

Antoniolli M, Solovey M, Bararia D, Strobl CD, Keay WD, Hildebrand JA, Heide M, Passerini V, Wange L, Enard W, Thieme S, Blum H, Rudelius M, Bultmann S, Leonhardt H, Subklewe M, von Bergwelt M, Colomé-Tatché M, Weigert O; ARID1A Controls a Novel Transcriptional Network Regulating FAS in Follicular Lymphoma. *Blood* **2021**; 138 (Supplement 1): 3492. doi: [10.1182/blood-2021-148862](https://doi.org/10.1182/blood-2021-148862)

Mentz M, Keay WD, Strobl C, **Antoniolli M**, Adolph L, Heide M, Lechner A, Häbe S, Osterode E, Kridel R, Ziegenhain C, Wange L, Hildebrand J, Shree T, Silkenstedt E, Staiger A, Ott G, Horn H, Szczepanowski M, Richter J, Levy R, Rosenwald A, Enard W, Zimmer-Strobl U, von Bergwelt-Baildon M, Hiddemann W, Klapper W, Schmidt-Supprian M, Bararia D, Rudelius M, Passerini V, Weigert O;. PARP14 is a novel target in *STAT6* mutant follicular lymphoma. *Leukemia* **2022**. <https://doi.org/10.1038/s41375-022-01641-x>

Adolph LC, Fichaux Q, Strobl CD, **Antoniolli M**, Passerini V, Keay WD, Jurinovic V, Lechner A, Hodson DJ, von Bergwelt M, Subklewe M, Rudelius M, Weigert O; CHOP but Not Bendamustine Reverses EZH2 Y641 Mutation Induced MHC-I/II Loss in Human Lymphoma Models. *Blood* **2021**; 138 (Supplement 1): 621. Doi: [10.1182/blood-2021-144803](https://doi.org/10.1182/blood-2021-144803)

Erpf AC, Stenzel L, Memar N, **Antoniolli M**, Osepashvili M, Schnabel R, Conradt B, Mikeladze-Dvali T. PCMD-1 Organizes Centrosome Matrix Assembly in *C. elegans*. *Curr Biol.* **2019** Apr 22;29(8):1324-1336.e6. doi: [10.1016/j.cub.2019.03.029](https://doi.org/10.1016/j.cub.2019.03.029)